10-2013

Image-based EUVL Aberration Metrology

Germain Louis Fenger

R·I·T

IMAGE-BASED EUVL ABERRATION METROLOGY

by

Germain Louis Fenger

A dissertation submitted in partial fulfillment of the requirements
for the degree of Doctorate of Philosophy in Microsystems Engineering

Microsystems Engineering Program
Kate Gleason College of Engineering

Rochester Institute of Technology
Rochester, New York
October, 2013

IMAGE-BASED EUVL ABERRATION METROLOGY

by

Germain L. Fenger

Committee Approval:

We, the undersigned committee members, certify that we have advised and/or supervised the candidate on the work described in this dissertation. We further certify that we have reviewed the dissertation manuscript and approve it in partial fulfillment of the requirements of the degree of Doctor of Philosophy in Microsystems Engineering.

_____

Dr. Bruce W. Smith Date
Director and Professor, Microsystems Engineering

_____

Dr. Karl D. Hirschman Date
Associate Professor, Electrical and Microelectronic Engineering, Director, Semiconductor & Microsystems Fabrication Laboratory

_____

Dr. Zoran Ninkov Date
Professor, Chester F. Carlson Center for Imaging Science

_____

Dr. Obert R. Wood II Date
Principal Member, Technical Staff at GLOBALFOUNDRIES

Certified by:

_____

Dr. Bruce W. Smith Date
Director, Microsystems Engineering Program

_____

Dr. Harvey J. Palmer Date
Dean, Kate Gleason College of Engineering

ABSTRACT

Kate Gleason College of Engineering

Rochester Institute of Technology

Degree: Doctor of Philosophy **Program**: Microsystems Engineering

Authors Name: Germain L. Fenger

Advisors Name: Dr. Bruce W. Smith

Dissertation Title: Image-Based EUVL Aberration Metrology

A significant factor in the degradation of nanolithographic image fidelity is optical wavefront aberration. As resolution of nanolithography systems increases, effects of wavefront aberrations on aerial image become more influential. The tolerance of such aberrations is governed by the requirements of features that are being imaged, often requiring lenses that can be corrected with a high degree of accuracy and precision. Resolution of lithographic systems is driven by scaling wavelength down and numerical aperture (NA) up. However, aberrations are also affected from the changes in wavelength and NA. Reduction in wavelength or increase in NA result in greater impact of aberrations, where the latter shows a quadratic dependence. Current demands in semiconductor manufacturing are constantly pushing lithographic systems to operate at the diffraction limit; hence, prompting a need to reduce all degrading effects on image properties to achieve maximum performance. Therefore, the need for highly accurate in-situ aberration measurement and correction is paramount.

In this work, an approach has been developed in which several targets including phase wheel, phase disk, phase edges, and binary structures are used to generate optical images to detect and monitor aberrations in extreme ultraviolet (EUV) lithographic systems. The benefit of using printed patterns as opposed to other techniques is that the lithography system is tested under standard operating conditions. Mathematical models in conjunction with iterative lithographic simulations are used to determine pupil phase wavefront errors and describe them as combinations of Zernike polynomials.

ACKNOWLEDGMENTS

I would like first thank my advisor, Dr. Bruce W. Smith, specifically for guiding me when needed, but giving me the confidence and room to think independently and critically. I would also like to thank my committee members Dr. Karl D. Hirschman, Dr. Zoran Ninkov, and Dr. Obert R. Wood II for guiding me through the PhD process. I would like to especially acknowledge and thank Obert, without his support much of this work would not have been possible.

I would like to acknowledge and thanks KLA Tencor for the use of PROLITH^{TM}, GLOBALFOUNDRIES for the fabrication of a phase-shifting reticle and processing support, the IBM alliance and partners for use of the cleanroom facilities including scanner and SEM tool time, Dr. Lena Zavyalova for her many discussions, Luke Orsini, Dr. Lei Sun, and Dr. Sudhar Raghunathan for help with exposures. I would also like to thank and acknowledge my fellow graduate students for their encouragement and support, Burak Baylav, Dr. Monica Sears, Andrew Estroff, Chris Maloney, Dr. Neal Lafferty and Dr. Peng Xie. I would also like to the U.S. Department of Education Graduate Assistance in Areas of National Need (GAAN) program and the Semiconductor Research Corporation (SRC/GRC) for their support.

Table of Contents

LIST OF FIGURES

LIST OF TABLES

LIST OF ACRONYMS

ANOVA	analysis of variance
ART	aberration ring test
CAR	chemically amplified resist
CCD	charge-coupled device
CD	critical dimension, [nm]
CTF	contrast transfer function
DOE	design of experiments
DPP	discharge produced plasma
DUV	deep ultraviolet region of the radiation spectrum (100–300 nm wavelengths)
DRAM	dynamic random access memory
EUV	extreme ultraviolet region of the radiation spectrum (10–30 nm wavelengths)
EUVL	extreme ultraviolet lithography
FEM	focus-exposure matrix
FWHM	full width half max
GUI	graphical user interface
HP	horizontal pitch
IC	integrated circuit
IFT	inverse Fourier transform
ILIAS	integrated lens interferometer at scanner
ITRS	International Technology Roadmap for Semiconductors
LER	line edge roughness
LPP	laser produced plasma
LSI	lateral shearing interferometry
MTF	modulation transfer function
NA	numerical aperture

NAND	‘not and’ logic circuit
OPD	optical path difference
OTF	optical transfer function
PAG	photo acid generator
PMI	phase measuring interferometry
PSF	point spread function
PSM	phase shifting mask
PSPDI	phase shifting point diffraction interferometry
PTF	phase transfer function
RMS	root-mean-square
RMSE	root-mean-square error
SEB	secondary electron blur
SEM	scanning electron microscope
TAMIS	transmission image sensor at multiple illumination settings
TEM	transmission electron microscope
TCC	transmission cross-coefficient
TIS	total integrated scatter
UV	ultraviolet region of the radiation spectrum (150–400 nm wavelengths)
VP	vertical pitch

1. INTRODUCTION TO LITHOGRAPHY

Since the invention of the integrated circuit (IC) in 1958, device performance has increased substantially. The performance gains have enabled new software and device applications not foreseen in the inception of the IC, such as supercomputers and smart phones. The gains in performance of the IC and other devices have followed the trend famously known as "Moore's Law" [1]. Gordon E. Moore, co-founder of Intel Corporation, predicted that the number of transistors in an IC would double approximately every two years. This trend has held true for the last four decades. The vehicle used to enable this trend has been traditionally photolithography, with current microprocessors having over 2.9 billion transistors [2], compared to Intel's first microprocessor manufactured in 1971, having 2,300 transistors [3]. This scaling is realized by shrinking the transistor dimensions, including gate length. Reducing gate length in a transistor results in higher current, lower parasitic capacitance, faster switching speed and smaller circuit footprint. This enables fabrication of sophisticated ICs that operate at higher frequencies and with more complicated circuit designs.

1.1 **Microlithography Systems and System Requirements**

Lithographic processes in the IC industry typically employ projection printing techniques for pattern transfer. An IC design on a reticle is transferred to a film that is radiation sensitive (i.e. photoresist on a substrate). In an IC manufacturing process several lithographic steps are required to create modern devices. A current state-of-the-art single exposure lithographic system uses deep ultraviolet (DUV) wavelengths with a

line narrowed excimer laser source to image features with a period or pitch (P) as small as 64 nm.

Figure 1 shows a schematic of a simple lithography system in which uniform illumination across the reticle is ensured by Köhler type illumination set up. The set up consists of both condenser and projection type optic, where source is imaged at pupil plane and reticle is imaged at wafer plane. The diffracted orders of the object are collected and focused through the projection lens onto the image plane or substrate to form an image that can be recorded by a photosensitive film such as photoresist. Photoresist will be discussed in more detail in Section 1.2.4. During normal operation of a scanner, both wafer and reticle are scanned simultaneously at a certain speed ratio governed by the optical magnification of the system.

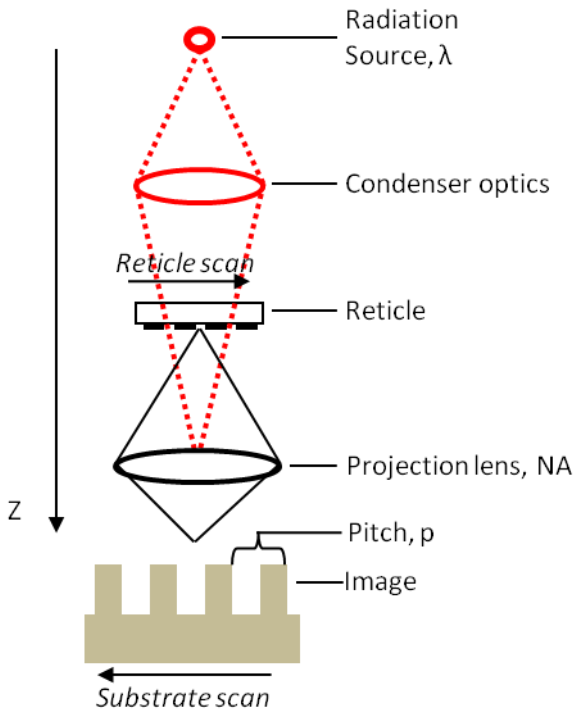

Figure 1: Depiction of a projection system used for pattern transfer in lithography.

The optical configuration of a projection lithographic system most closely resembles a microscope [4]. The demands of lithographic systems, however, are far greater than that of the modern microscopes. There are two criteria that are used to describe an optical system, namely resolution and depth-of-focus (DOF). The resolution criterion, first defined by Lord Rayleigh [5] and shown in Equation (1.1), has traditionally been driven by source wavelength scaling to meet the demands of shrinking transistor designs. The minimum resolvable pitch in diffraction limited optical system is defined as:

$$P_{min} = \frac{2\,k_1\lambda}{n\,sin(\theta)} = \frac{2\,k_1\lambda}{NA} \tag{1.1}$$

where P_{min} is the minimum resolvable line pitch, k_1 is a process capability factor and has a theoretical limit of 0.25 for incoherent illumination, λ is the source wavelength, n is the imaging medium, θ is the maximum half angle in the imaging plane and NA is the numerical aperture of the projection lens. The k_1 factor is dependent on several things including illumination source shape, photoresist resolution, and mask properties. The depth of focus of an optical system is given by Equation (1.2).

$$DOF = \pm\frac{k_2 n\lambda}{NA^2} \tag{1.2}$$

where k_2 is also a process related factor.

From the Rayleigh criterion, it is straightforward to reduce the minimum resolvable pitch by reducing the wavelength. In fact, over the past decades, advances in resolution have been made possible, traditionally by scaling wavelength (λ) from the early lithography tools that used a wavelength of 436 nm from the g-line of a mercury arc

lamp to current state of the art lithography tools that use a wavelength of 193 nm from an ArF excimer laser. Several years of research were spent investigating 157 nm lithography using a F_2 laser source, but the attempts eventually failed due to lack of timely production of photoresist and lens materials for that wavelength and the benefits of immersion lithography performed at already established 193 nm lithography platforms [6]. Scaling in NA has also gained significant momentum following the demise of 157 nm lithography [7]. Lens manufactures have developed the ability to precisely make large high quality lenses, enabling increase of NA in 193 nm tools. Using the 193 nm platform, high NA tool were created. Theoretically, NA has an upper limit of 1 for an air ambient; but this can be increased to 1.35 when water replaces the air gap between the final lens and the substrate. Further developments of high index liquids (HIL) for NA > 1.35 suffer from issues such as IC manufacturing process incompatibility and viscosity challenges for high speed scanning. Besides the demanding material requirements on the HIL, the projection optics would need to be drastically changed to support the high NA, as-well-as changes in the photoresist film stack materials [8].

The next logical technology node is extreme ultraviolet lithography (EUVL). EUVL systems do not utilize high NA; but, the resolution is increased again by scaling wavelength. EUVL uses a wavelength of 13.5 nm, which is fourteen times smaller than current state-of-the-art DUV systems (193 nm). Apart from having a much smaller wavelength than DUV lithography systems, EUVL systems are quite different in that at 13.5 nm wavelength, air (N_2, O_2, etc.) becomes very absorbing. Therefore EUVL systems must operate under vacuum to remove these impurities. Another problem is that there is very little difference in index of refraction between different materials at 13.5 nm, since

all indices are close to one. So, it is not possible to make a refractive lens with any focusing power as the refraction angle is almost the same as the incident angle. Figure 2 shows refraction of the same incident ray from air (n_o) into a medium (n_1) with a low index contrast (n_1/n_o) and a medium (n_2) with higher index contrast (n_2/n_o). The ray that enters medium 1, which has an index close to one, is virtually undeviated compared to the ray that enters medium 2.

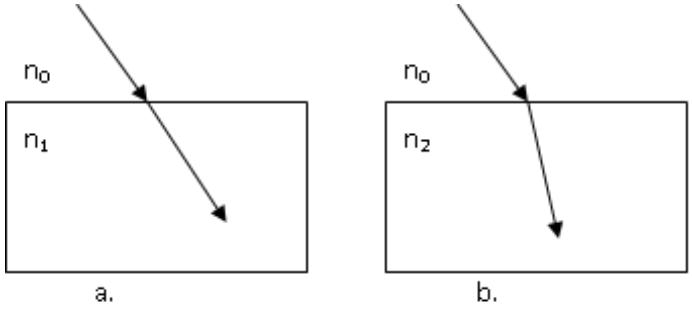

Figure 2: Depiction of refraction (a) with a low index contrast and (b) with a higher index contrast.

Furthermore, almost all materials are absorbing at 13.5 nm wavelength, which makes fabrication of a low loss thick lens, to obtain enough focusing power for a low index contrast material, very challenging. Due to these aforementioned problems, EUV projection optics are based on reflective components. In order to reflect EUV photons with high efficiency, mirrors composed of alternating layers of high and low refractive index materials such as silicon and molybdenum with indices at 13.5 nm of 0.999 and 0.924 respectively, which has an index contract of 0.925, are used. The lenses in current full field scanners have a numerical aperture of 0.33, which is much less than the NA of state of the art immersion lithography systems (1.35).

The final factor in Equation (1.1) is k_1, which is a process dependent parameter. There have been many technologies developed in lithography to make a lower k_1

possible, known as resolution enhancement techniques (RET). These RET include off-axis illumination [9], sub-resolution assist features [10], phase shift mask (PSM) [11], source mask optimization (SMO) [12], and custom polarization [13].

1.1.1 *Off-axis illumination*

For a simple grating mask, the illuminating beam is split into discrete diffraction orders, some of which are collected by the objective lens. The diffracted orders are then focused by the objective lens in the image plane and form an image of the mask. If the grating pitch is small enough, the objective lens may only collect the 0^{th} diffraction order as seen in Figure 3a, resulting in no image modulation. One diffraction order is not sufficient to produce any kind of modulation on the wafer plane. However, when the mask is illuminated at an angle, it is possible for the objective lens to capture two diffraction orders as depicted in Figure 3b showing the capture of the 0^{th} and $+1^{st}$ diffraction orders by shifting the 0^{th} order to one side of the entrance pupil allowing the $+1^{st}$ order to be captured by the other side of the entrance pupil. The interference of the 0^{th} and the 1^{st} diffraction order creates a sinusoidal electric field, an image of the mask grating.

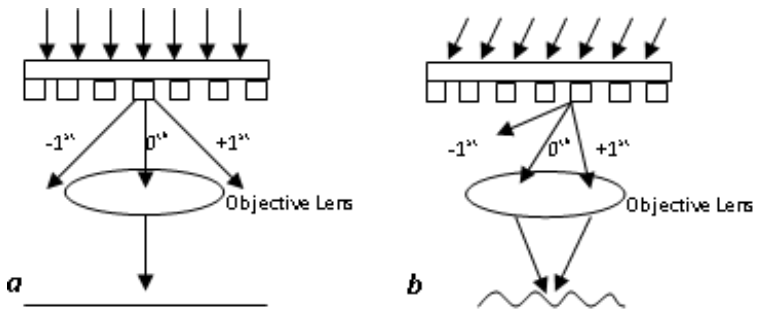

Figure 3: Diagram of (a) on-axis illumination showing the collection of the 0^{th} diffraction order only and (b) off-axis illumination showing the collection of the 0^{th} and $+1^{st}$ diffraction order

Off-axis illumination also has the benefit of enhancing depth-of-focus. For on-axis illumination, the depth-of-focus is defined as the defocus distance at which the wavefront phase difference between the 0^{th} order and an order on the edge of the pupil is $\pi/2$. This amount of defocus prevents the orders to interfere with each other, creating no modulation. For the off-axis illumination case, the defocus difference between the 0^{th} and 1^{st} order is always going to be less than the on-axis case, greatly improving the depth-of-focus. If the 0^{th} and 1^{st} orders are symmetric about the pupil, the depth of focus will be infinite. Therefore the optimum illumination angle (θ_i) can be described by Equation (1.3).

$$\theta_i = sin^{-1}\left(\frac{\lambda}{2P}\right) \tag{1.3}$$

where λ is the illumination wavelength and P is the grating pitch. As can be seen the optimum illumination angle is a function of grating pitch. A pitch will therefore have an optimum illumination angle. With increasing pitch, the benefit of the off-axis illumination will decrease, diffraction orders become asymmetrically distributed in the lens pupil, until higher orders are captured. This usually occurs near $P=\lambda/[(\sigma-1)\sin(\theta_i)]$.

For the simple grating case presented here, the imaging enhancement will only occur in one mask direction, the direction perpendicular to the projected incident beam. The features on the mask that are parallel to the projected incident beam will not receive any benefit from the off axis illumination. Therefore the illuminator angle will need to be optimized for a given layout. Several common examples of illuminations are shown in Figure 4. A monopole illumination, shown in Figure 4a is the simple example discussed previously and will only benefit features that are perpendicular to the projected

illumination angle. Dipole illumination, similarly to monopole illumination will only benefit structures that are perpendicular to the projected illumination angle. Dipole illumination, which is shown in Figure 4b, is used in place of monopole illumination to balance the diffraction orders of the 0^{th} and $+1^{st}$ from the right with the 0^{th} and -1^{st} from the left. Quadruple illumination, shown in Figure 4c, can boost resolution for both vertical and horizontal oriented pitches. Annular illumination, shown in Figure 4d, will work best for any arbitrary pitch orientation.

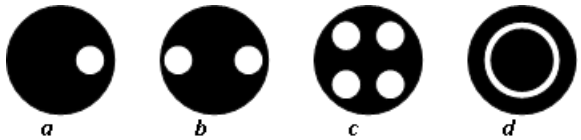

Figure 4: Common off-axis illuminations used in lithography: (a) monopole, (b) dipole, (c) quadruple, and (d) annular illumination

1.2 **Lithography Tool Considerations**

The next generation of lithographic systems is determined by the availability of materials that have the required transmission, absorption, sensitivity and resolution at a given wavelength as well as a radiation source with sufficient output power at the desired wavelength. The critical components that all need to be in place and meet the material and production demands include photoresist, objective lens and illumination optics, source and mask. In the next subsections each of these aspects will be discussed in more detail as well as the requirements from the IC industry laid out in the International Technology Roadmap for Semiconductors (ITRS) [14].

1.2.1 *International Technology Roadmap for Semiconductors*

The requirements to meet the demands of the systems presented in this chapter are detailed in the International Technology Roadmap for Semiconductors (ITRS), a roadmap for silicon-based semiconductor technology that describes the technology required for each device shrink for the next decade [14]. Each year a new device generation or node is introduced. This new node has smaller feature sizes than the previous node. The trends showed in the ITRS are tighter process control with shrinking device size. At each device generation or node, there are industry wide goals set by the IC manufactures and tool vendors stating the requirements for line critical dimension (CD) control (variation, minimum feature size, k_1) for each device type: DRAM, NAND flash, and logic. The ITRS also highlights the need for more work to be done on certain areas where the need is not being met. This facilitates open discussions with IC manufacturers and equipment and material vendors. This is depicted in Table 1, the white cells indicate issues that have solved and a manufacturable solution is available. The areas in yellow show a possible solution is in place, but this solution requires more work to implement in production at satisfactory levels. The areas in red have no solution available and research needs to be focused in these areas.

Table 1: ITRS device requirements for the next five years [14]

Year of Production	2011	2012	2013	2014	2015	2016	2017
DRAM ½ pitch (nm) (contacted)	36	32	28	25	23	20.0	17.9
DRAM							
DRAM ½ pitch (nm)	36	32	28	25	23	20	18
CD control (3 sigma) (nm) [B]	3.7	3.3	2.9	2.6	2.3	2.1	1.9
Contact in resist (nm) - Note Optical now, EUV later	55	55	55	55	29	26	23
Contact after etch (nm)	36	32	28	25	23	20	18
Overlay [A] (3 sigma) (nm)	7.1	6.4	5.7	5.1	4.5	4.0	3.6
k1 (13.5nm) EUVL	0.66	0.59	0.52	0.47	0.55	0.49	0.44
Flash							
Flash ½ pitch (nm) (un-contacted poly)	22	20	18	17	15	14.2	13.0
CD control (3 sigma) (nm) [B]	2.3	2.1	1.9	1.8	1.6	1.5	1.4
Bit line Contact Pitch (nm) [D]	131	120	110	101	93	113	104
Contact after etch (nm)	36	32	28	25	23	20	18
Overlay [A] (3 sigma) (nm)	7.2	6.6	6.1	5.6	5.1	4.7	4.3
k1 (13.5nm) EUVL	0.42	0.39	0.35	0.32	0.38	0.35	0.32
MPU / Logic							
MPU/ASIC Metal 1 (M1) ½ pitch (nm)	38	32	27	24	21	18.9	16.9
MPU gate in resist (nm)	35	31	28	25	22	20	18
MPU physical gate length (nm) *	24	22	20	18	17	15	14
Gate CD control (3 sigma) (nm) [B] **	2.5	2.3	2.1	1.9	1.7	1.6	1.5
Contact in resist (nm)	55	55	55	55	28	25	22
Contact after etch (nm)	43	36	30	27	24	21	19
Overlay [A] (3 sigma) (nm)	7.6	6.4	5.4	4.8	4.2	3.8	3.4
k1 (13.5nm) EUVL	0.70	0.59	0.50	0.44	0.52	0.46	0.41

The lithography requirements, current status, and development timeline are described for each device generation. This is shown in Figure 5a for NAND (logic 'not and') flash devices and Figure 5b for DRAM (dynamic random-access memory) devices with the potential lithography systems that may be adopted, the timing of development and implementation, and at what node. The figure also shows where innovation in needed due to available technology may not meet the demands for future nodes. It is important to note that insertion of a technology must be timed sufficiently in the future to meet the development requirements. For example, at the 11 nm node, the candidates for the lithography technology are EUV with multiple patterning, ArF with multiple patterning, EUV with 6X reticle reduction, nanoimprint, EUV with directed self assembly (DSA), together with innovative solutions not yet developed.

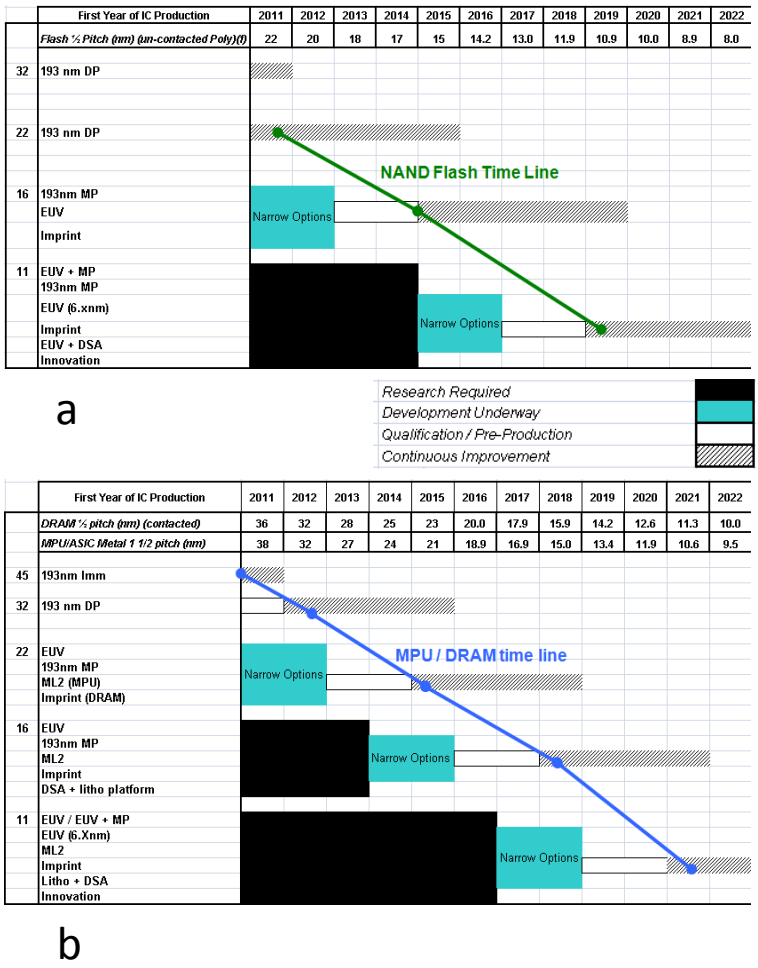

Figure 5: ITRS lithography roadmap for a) NAND Flash and b) DRAM devices [14]

1.2.2 *Lithography Source*

As the lithographic wavelength has scaled to meet the resolution requirements of the next generation of integrated circuits, so must change the source used to generate that wavelength. When choosing the wavelength of the next generation of lithography systems, factors such as source availability, available lens material, and available photoresist material are each considered. Early lithography systems used a glow-discharge Hg arc lamp as a radiation source with a noble gas ambient (Xe). The mercury arc lamp (Hg-Xe) has an intensity peak at 436 nm (g-line), 405 (h-line) and 365 nm (i-

line) that were used successfully in lithography systems. The use of Hg-Xe lamps for sub 365 nm wavelengths was abandoned due to lack of power at the desired wavelength [15] and failed attempts to raise the power due to heating from the other non-desirable emission wavelengths.

With the commercialization of the excimer laser in the late 70's [16,17], a new opportunity for lithography sources was opened and in 1982 IBM first demonstrated the use of an excimer laser in photolithography [18]. The gain medium of an excimer laser is a gas mixture of a noble gas and a halide. The excimer laser sources successfully used in lithography are krypton fluoride (KrF) with an emission wavelength of 248 nm and argon fluoride (ArF) with an emission wavelength of 193 nm. Excimer lasers are well suited for lithography due to their narrow bandwidth (when spectrally narrowed) and high power scalability [19].

The bandwidth of a source used in lithography needs to be small to reduce comatic aberration and image blur. An emission peak of a laser or arc lamp has some width, this traditionally is measured at the full width and half of the maximum intensity of the emission peak. Figure 6 shows an example of an emission peak and the measurement of full width half max (FWHM).

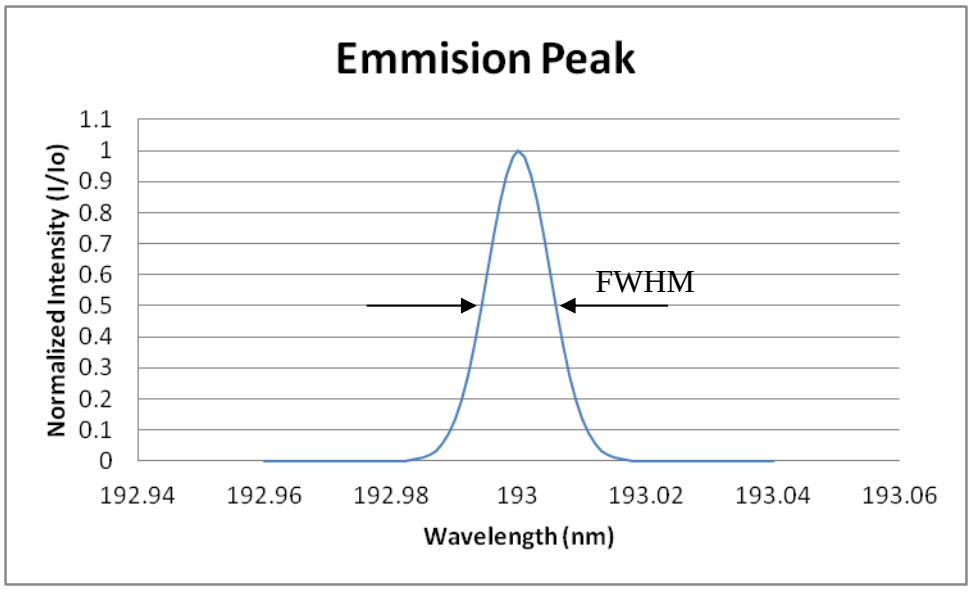

Figure 6: Gaussian emission peak showing measurement location of bandwidth for a spectrally line-narrowed ArF excimer laser (FWHM=12pm)

Comatic aberration is caused by focal length changes of a refractive lens due to material dispersion or a wavelength dependent change in index, each wavelength will have a different ideal focus position. This ultimately degrades contrast and adds image blur. Comatic aberrations have traditionally been corrected using a cemented doublet. A cemented doubled is two lenses that have been cemented together, each lens has a different index of refraction, enabling wavelength dependent correction. The doublet is typically designed for a specific wavelength range. In deep ultraviolet lithography (DUV) lithography however, there are few materials that have low absorption and lenses are made from ultra violet (UV) grade fused silica, making correction of comatic aberration by the use of a cemented doublet not possible because two materials of different index are needed. Therefore, to correct for chromatic aberration, other methods are employed including use of a spectrally pure source (one with a bandwidth in the picometer range), or the use of entirely reflective optics, which do not suffer from

chromatic aberration or mostly reflective optics. With respect to narrow bandwidth solution to chromatic aberration, this is prohibitive for free-running excimer lasers where the high efficiency for populating metastable states creates a larger temporal coherence than most lasers, having a bandwidth of one nanometer. Spectral line narrowing, on the order of a picometer bandwidth is therefore not the solution for high volume manufacturing and chromatic aberration then preferably corrected in another manner, namely in the lens design, which will be discussed in section 1.2.3.

Current EUV lithography tools under development use a 13.5 nm source either a discharge produced plasma (DPP), or a laser produced plasma (LPP) [20,21]. Figure 9 shows a schematic of DPP and LPP source technology used to generate 13.5 nm wavelengths. In both LPP and DPP source technologies, generated hot plasma fuel emits EUV photons. Fuel materials that have been demonstrated include tin (Sn) and xenon (Xe). DPP sources use low energy plasma created by an applied voltage, the plasma is then magnetically pinched creating high energy plasma. In the high energy plasma electrons in the fuel material are excited and EUV photons are emitted when the electrons relax to the ground state. Figure 7 shows the time averaged measured emission spectrum of Sn that has been magnetically pinched to create high energy plasma. Figure 8 shows the calculated emission spectrum for Xe from high energy plasma. The emission spectra show a bandwidth of a few nanometers; but since the projection optics are purely reflective, the requirements on the bandwidth can be relaxed compared to DUV lithography for the case of chromatic aberration.

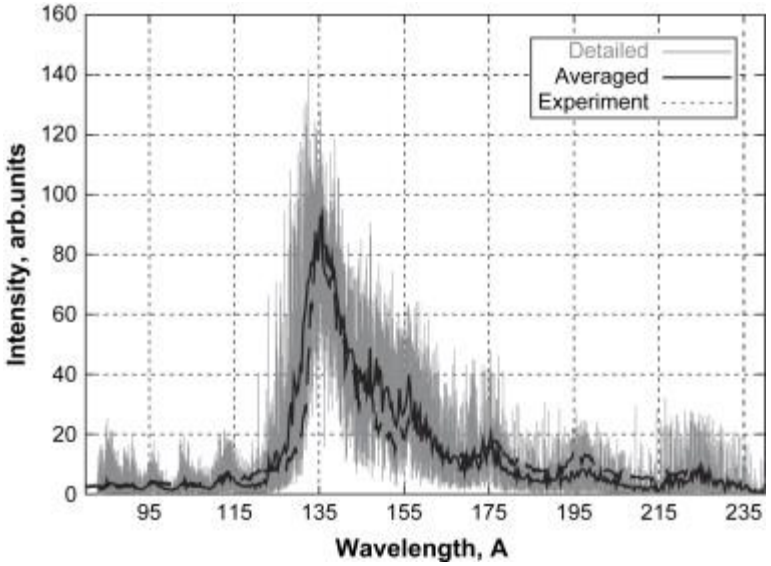

Figure 7: Time integrated emission spectrum of a high density plasma of Sn that has been magnetically pinched [22]

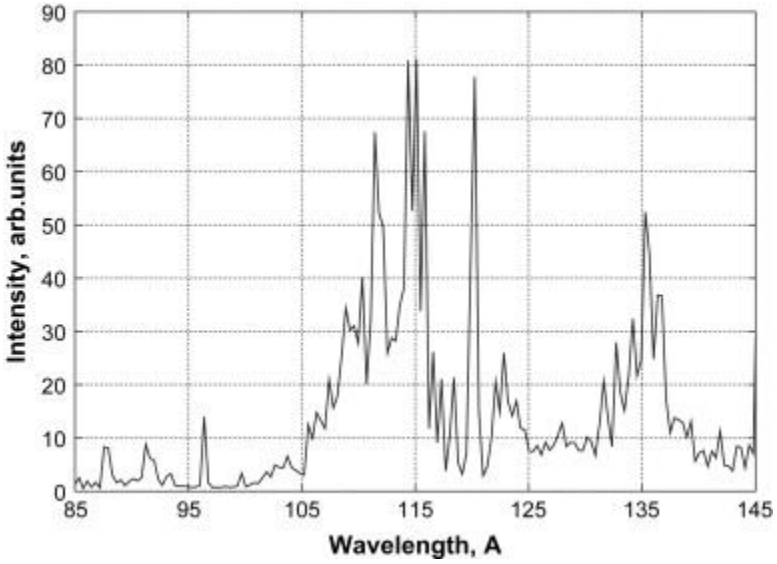

Figure 8: Calculated emission spectrum of a high energy plasma of Xe [22]

The emitted photons are then directed into a beam by the collector mirrors made of silicon, molybdenum multilayer, more will be discussed on the multilayer in section 1.4. Similarly, LPP sources use high energy plasma created by a CO_2 laser to excite the

electrons in fuel material where EUV photons are emitted when the electrons relax to a ground state. The photons are then directed in a beam by the collector mirror. Currently LPP source with Sn fuel is the most promising candidate for high volume manufacturing (HVM), showing stable high energy plasmas experimentally[20,21,23].

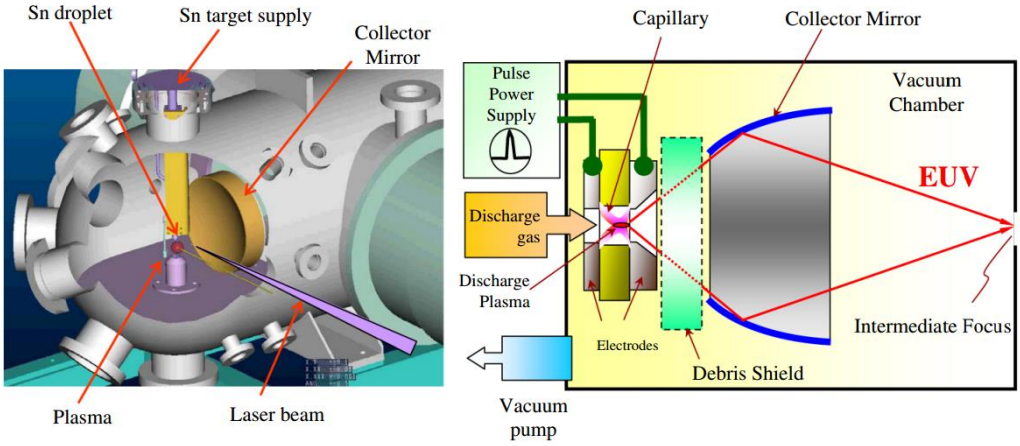

Figure 9: Diagram of the two EUVL source candidates LPP (left) and DPP (right) [20]

1.2.3 *Lithography Projection Optics*

In modern scanners, projection optics have become much more complicated than the simple case depicted in Figure 1. Modern optical lithographic systems have over 30 elements in the projection lens with both refractive lenses and reflective mirrors being used. These catadioptric lenses, an example shown in Figure 10, became necessary in order to reduce lens size and cost while maintaining field flatness[24]. Comparing to these complex systems, the current EUVL systems have a rather simple projection lens design. For example, ASML 3100 pre-production tool has an NA of 0.25 and a six mirror design with a fixed partial coherence of 0.8 [25]. Figure 11 shows a schematic of an EUV system with a projection lens made up of 6 mirrors and an LPP source.

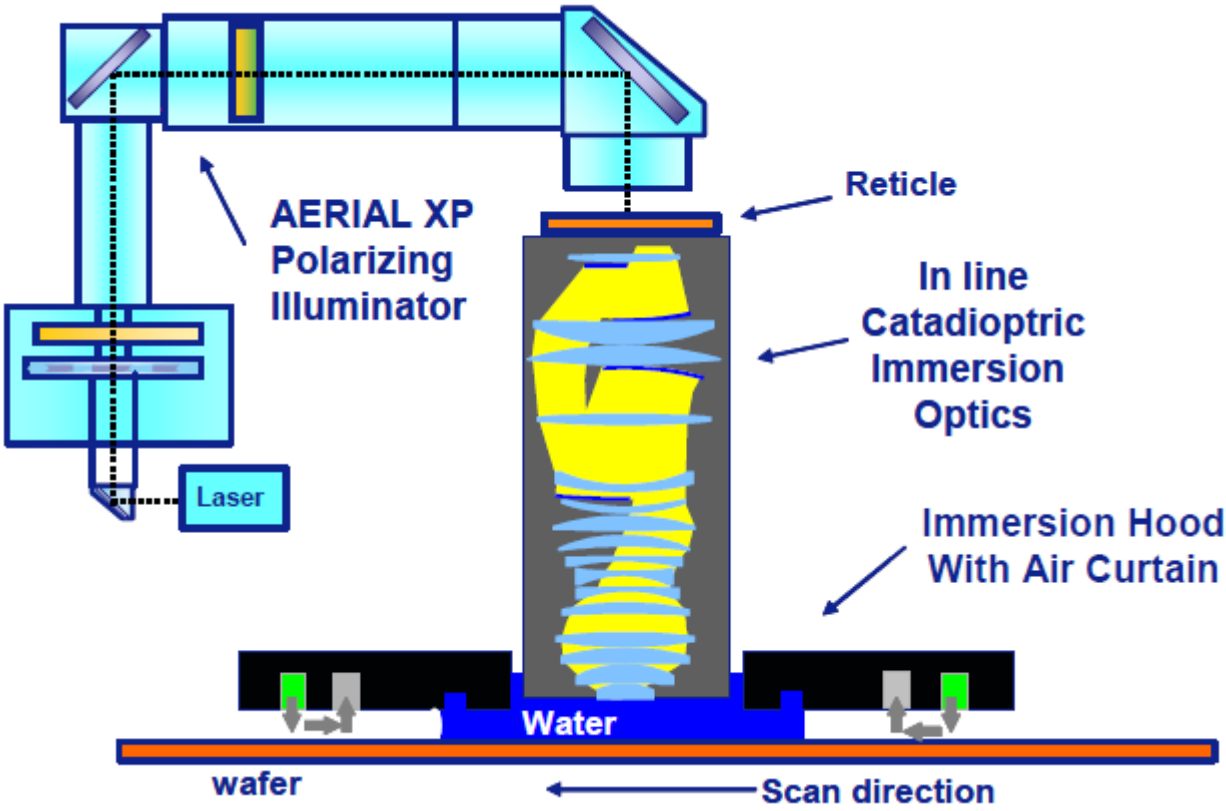

Figure 10: Schematic of a catadioptric lens using both refractive and reflective elements [24]

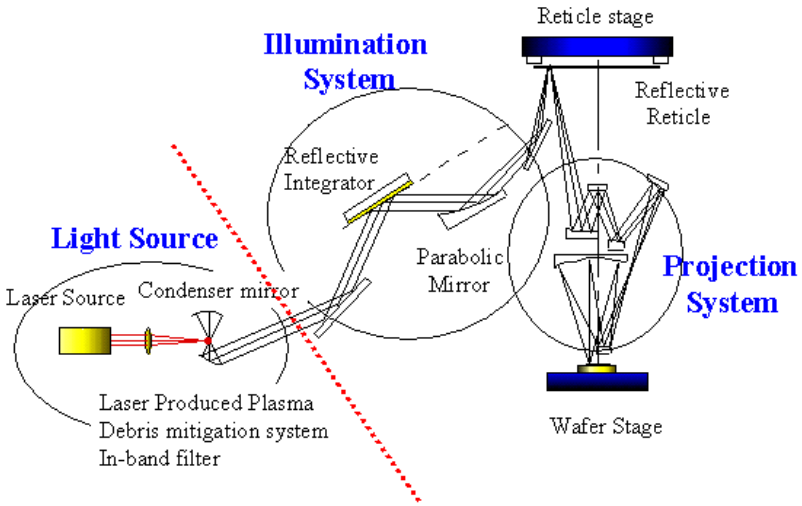

Figure 11: Schematic of the optics used in an EUVL system showing an LPP source, illumination system, reflective reticle and projection optics [26]

Current state of the art projection optics have the requirement of sub nanometer flatness. Scattering from a rough surface will create stray light in the lithography scanner. The stray light can directly degrade contrast by adding a constant intensity to all features; this nonideal effect is called flare. Because scattering scales with wavelength, EUVL will have more scattering than DUV lithography off the same roughness and therefore EUVL has a higher requirement than DUV lithography on optic roughness. More detail on flare will be discussed in section 1.3.

1.2.4 *Photoresist*

Photoresists are photopolymeric etch resistant material, which are used in lithography for the process of pattern transfer from a design on a reticle to an IC chip. A photoresist's function is to record radiation intensity or design data from the reticle and transfer that data from the film to the underling layer. In modern chemically amplified positive photoresists, when the film of photoresist is exposed to a specific wavelength of light, a photosensitizing photoacid generator (PAG) produces an acid, de-protecting the base resin (such as a polyacrylate for 193 nm), making it more soluble in basic solution. The de-protection process is amplified by baking the photoresist, allowing the generated acid to be regenerated and diffuse with a sufficient mean free path [27]. For EUV lithography there is an added complexity that each photon will generate secondary electrons through ionization. These secondary electrons can diffuse up to 7 nm from the initial ionization region before they activate a PAG [28,29]. This secondary electron blur (SEB), combined with stochastic effects manifests itself as line edge roughness (LER) [30] and may limit the use of chemically amplified resist (CAR) in EUVL.

1.3 **Imaging in EUVL**

EUVL optics cannot achieve perfect reflectivity, only having ~70% reflectivity per mirror [31–35]. Figure 12 shows the reflectivity of Mo/Si multilayer versus angle of incidence, as well as the required angles for a 0.43 NA 6 lens system. The dashed line is the reflectivity of a standard multilayer, by tuning the layer period the angular response can be shifted and tuned to be flat over a given angle range, shown in the solid line. This creates unique challenges for EUVL, as not only lens manufacturing and mask fabrication are different from other lithography technologies, but also the beam line can no longer be orthogonal if an unobscured full field catoptric system is used.

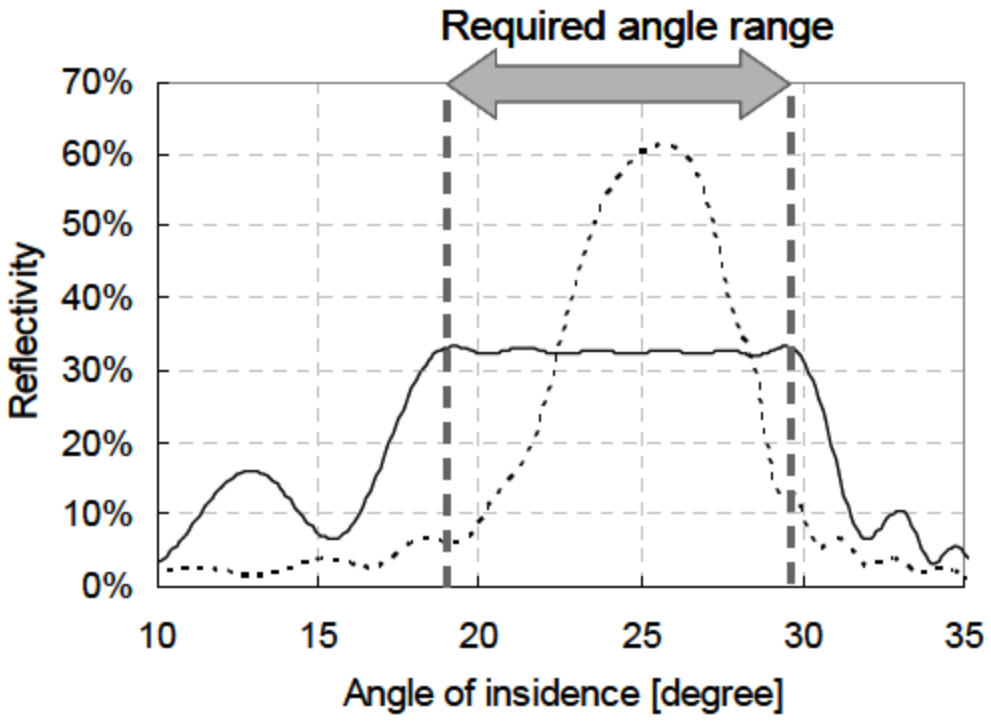

Figure 12: Reflectivity versus angle of incidence for (dashed line) standard multilayer stack and (solid line) broad angle multilayer stack [36]

Several non-ideal affects also scale with source wavelength, such as aberrations, flare, and scattering, further increasing requirements of EUV mirrors. Figure 11 shows a schematic of an EUVL system using a catoptric design, and Figure 13 shows a diagram of the optics as implemented in a EUVL system.

Some issues specific to EUVL that were well controlled or not applicable in previous generations of lithography tools are: horizontal vertical bias caused by non orthogonal paraxial beam, flare caused by mirror roughness on the order of the exposure wavelength, shot noise, phase defects caused by multilayer defectivity, and challenges in fabricating phase shifting reticles [31,37–50].

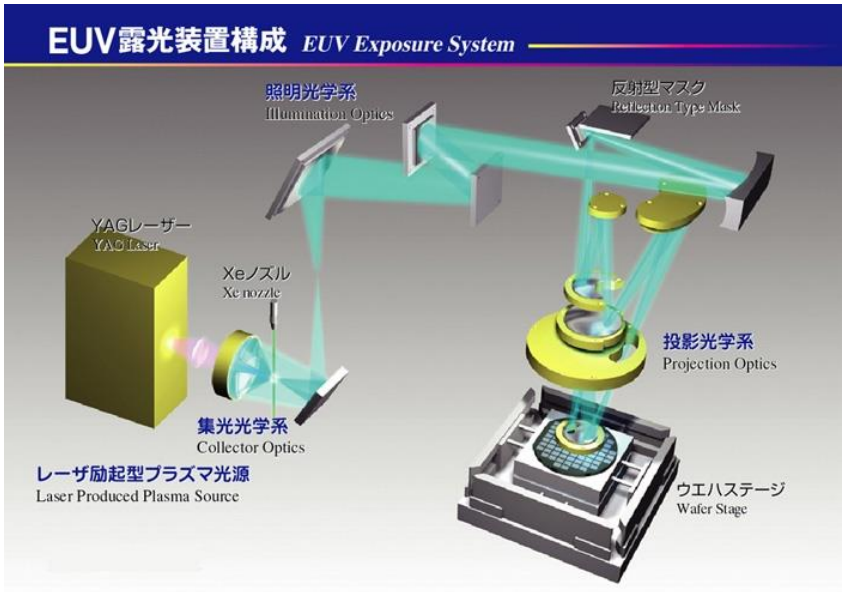

Figure 13: A diagram of the optical system used in an EUVA EUV lithography tool [26]

1.3.1 *Flare*

Stray light, also known as flare, is the light scattered in a lens system that reaches the imaging plane. The scattering of light will reduce the intensity in the bright areas and increase the intensity in the dark areas. Flare is still broadly defined by the dose that

makes a 2-μm pad disappear, but its estimate is carried out mainly visually, using optical and e-beam metrology indiscriminately. Flare effects are critical in EUV lithography because the amount is proportional to the inverse square of the wavelength. Therefore, mirror roughness in EUVL causes more scattering than in DUV due to the 14X reduction in wavelength. This is shown in Figure 15, which is a plot of total integrated scatter (TIS) versus lens roughness for EUV (13.5 nm) and DUV (193 nm) wavelengths. TIS can be derived from the roughness of the lens and wavelength being used for imaging as shown in Equation (1.4).

$$TIS = R\left[1 - e^{-\left(\frac{4\pi\sigma_r \cos(\theta_i)}{\lambda}\right)^2}\right] \tag{1.4}$$

where R is the reflectivity of the lens, σ_r is the surface roughness [units (nm)], and θ_i is the angle of incidence on the surface. The point-spread function (PSF) is used in determining flare and is calculated from the power-spectral density (PSD) of the objective lens as shown in Equation (1.5).

$$PSF(\rho) = \left(\frac{4\pi}{\lambda^2 z}\right)^2 PSD\left(\frac{\rho}{\lambda z}\right) \tag{1.5}$$

where λ is the wavelength of light, and PSD is the power spectral density of the objective lens in the pupil, as a function of radius, ρ. The impact on the image intensity from flare is shown in Equation (1.6), which is the original image convolved with the function shown in Figure 14. I_o is the original image, which will be described in more detail in section 2.1, and $I_F(x,y)$ is the blurred image due to flare.

$$I_F(x,y) = (1 - TIS)I_o(x,y) + PSF \otimes I_o(x,y) \tag{1.6}$$

where I_o is the original image.

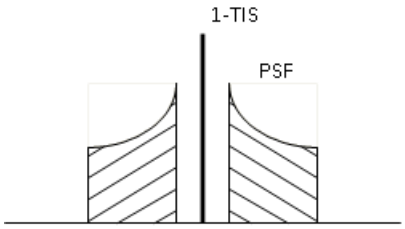

Figure 14: Function that describes the impact of flare on imaging

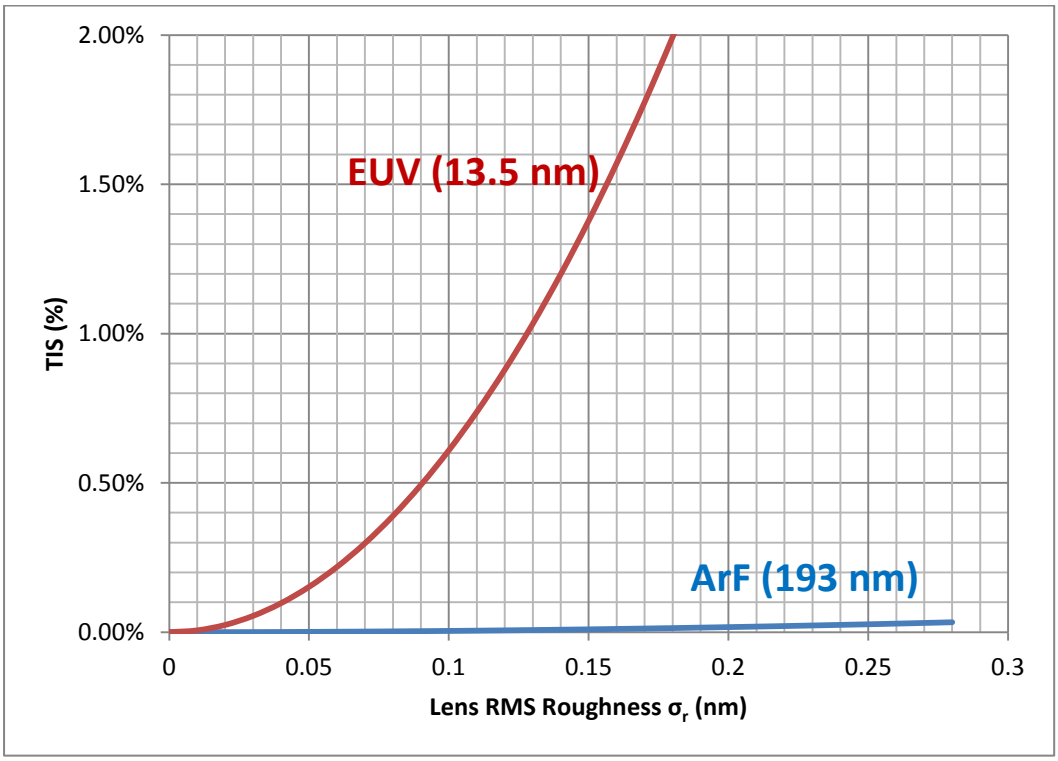

Figure 15: Comparison of TIS for EUV and ArF wavelengths

The range of influence of flare in EUV can be extremely broad (millimeters or more), so that an effective full-chip compensation strategy is gennerally needed to be able to satisfy the requirements for the 32-nm node and beyond [42,51]. At the core of any strategy for flare correction is the ability to accurately and effectively calculate the local

flare levels across the chip design, producing what is commonly known as a flare map. The calculation of flare maps in a reasonable time is not an obvious task, requiring the convolution of an extended PSF with the image or design density map at a reasonable resolution. To confirm the correctness of flare calculation, comparison to measured values is critical.

1.3.2 *Shadowing*

Another issue that is specific to EUVL is an effect known as 'shadowing'. Because of the catoptric (reflective) design of EUVL optics, the paraxial beam of current full field scanners is not orthogonal to the mask. An orthogonal optical axis is not possible without obscuration, especially when scaling lenses to larger designs. This non-orthogonality causes a 'shadowing' effect of lines that are perpendicular to the projected paraxial beam, as seen in Figure 16. Part of the reflected beam is blocked, effectively making lines in one orientation print larger than design in a positive photoresist. This effect must be accounted and corrected for in mask design and is done so by adding an orientation dependent bias or by using a model based correction approach, especially sub 20 nm features and at large optical angles [52]. The horizontal and vertical bias can be reduced by making the absorber height smaller, but it cannot be eliminated because the effective reflection layer is inside of the multilayer, so this effect would be present even when the absorber has a height of zero.

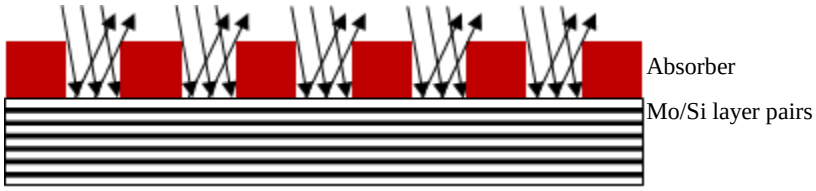

Figure 16: Illustration of non-orthogonal incident reflections on a mask with topography showing partial blocking and 'shadowing' of a line

1.3.3 *Shot Noise*

Shot noise is discrete photon uncertainty, resulting from individual photon effects during the exposure process. Consider, for instance, a light source that emits photons randomly at a rate of R photons per unit time into an area A where each photon is independent. Over a short period of time dT where RdT is < 1, a photon is either emitted or not emitted. With these assumptions the problem can be simplified to a Bernoulli trial [53], resulting in a binomial probability distribution of the number of photons n emitted over a period of time T. If a time division dT is chosen such that is allowed to approach zero, the number of intervals N in the given time T then approaches infinity. With N infinite and dT zero and if $NRdT=TR$ and is finite and nonzero, the binomial converges to a Poisson distribution as shown in Equation (1.7) [54] .

$$B(n) = \frac{(TR)^n}{n!} e^{-TR} \tag{1.7}$$

The Poisson distribution is easier to use for large N and can be easily applied to photon emissions. The expected number of photons is RT, and the variance is also RT for a Poisson distribution. Making this more meaningful to a lithographer, the expected intensity I is used, which is the expected number of photons n multiplied by the energy of a photon $E=hc/\lambda$ divided by the area where you are measuring the intensity A times time interval T as seen in Equation (1.8).

$$I = \frac{n}{TA} E = \frac{R}{A} E \tag{1.8}$$

Since the variance of the Poisson distribution is equal to the expected value, then the standard deviation of the expected value of the intensity is shown in Equation (1.9).

$$\sigma_I = \frac{\sqrt{n}}{TA}E = \frac{I}{\sqrt{n}} \tag{1.9}$$

As can be seen, the standard deviation of the intensity of radiation from this system is proportional to one over the square root of the number of photons. This relationship is call shot noise. For a given intensity, having high energy photons will have a larger noise than having low energy photons because more photons will be collected in the low energy case. Calculating the energy of a photon for 13.5 and 193 nm light gives a result of 1.47×10^{-17} J and 1.03×10^{-18} J respectively. This energy difference in photons manifests itself as added noise as can be seen in Figure 17, a plot of shot noise for a 1x1 nm square for EUV and ArF lithography assuming all photons are absorbed in the photoresist.

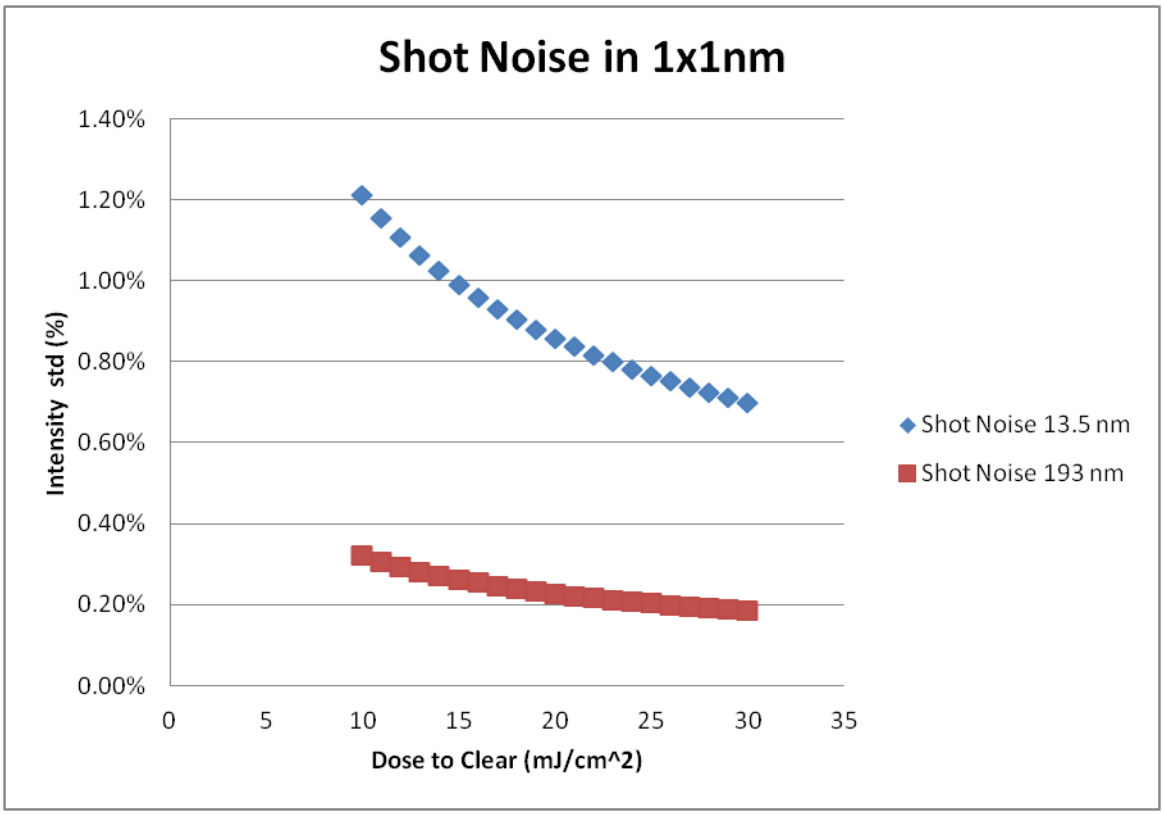

Figure 17: Plot of percent standard deviation of 193 nm and EUV (13.5 nm) intensity due to shot noise integrated in an area of 1x1 (nm^2)

1.3.4 *Aberrations*

In any imaging system, aberrations lead directly to image degradation. Every surface the imaging beam interacts with contributes to the overall system aberration level and these aberration levels can vary with imaging field position, lens temperature, source coherence, and other environmental conditions. Traditionally, a diffraction limited imaging system is one that produces no more than $\lambda/4$ wavefront optical path difference (OPD). This Raleigh criterion is sufficient for imaging in most imaging applications, but does not meet the aggressive requirements of lithographic systems. In lithography, the need for tight control of aberrations is driven by the whole system and application requirements, including photoresist and process needs as well as specifications for line

width roughness (LWR), line CD uniformity (CDU), and field to field uniformity [55–57]. These specifications are determined by the resulting electrical performances of devices that are being fabricated and are shown in the ITRS. Modern lithography tools therefore require that aberrations be well understood and characterized so that they may be accounted for and corrected, if possible [58–73]. Unlike other state-of-the-art lithography systems, which for example have aberration requirements on the order of $\lambda/200$ (0.97 nm OPD) for a k_1 of 0.3 for 193 nm wavelengths to meet resolution requirements of the 45 nm hp node, EUVL has an equivalent requirement of just $\lambda/20$ (0.675 nm OPD) to $\lambda/30$ (0.45 nm OPD) to meet the requirements of state-of-the-art manufacturing [74,75] for the comparable specifications on OPD. Given the lower scaled wavefront aberration specifications for EUVL, characterization methods not suitable for other lithography systems are suitable for EUVL. Such methods will be discussed as well as image formation and pupil phase characterization in Section 3.6.

1.4 **Photomasks**

In photolithography, photomasks (masks) or reticle technology is an important aspect that must be understood and controlled for critical IC manufacturing specifications. There are a number of types of technologies and materials that are used in fabricating masks. These materials have been carefully selected based on their performance and cost. Figure 18 shows a typical mask schematic for both optical and EUVL and also the representative image intensities and electric field assuming a diffraction limited system. Optical lithography masks generally have an opaque metal

such as chromium oxynitride, patterned on a transparent substrate, typically quartz for 193 nm wavelengths and a schematic of such a reticle is shown in Figure 18a.

No single layer materials, or material composites, exist that can reflect normally incident EUV light or have a significantly different index of refraction from vacuum to construct a transparent lens with any focusing power. Therefore EUVL reticles and optics use constructive interference from repeated film layers, typically made from alternating molybdenum and silicon, to create normal incidence mirrors for 13.5 nm wavelengths [49]. At each interface of molybdenum and silicon, part of the radiation is transmitted and part is reflected. By engineering the materials and the thickness of the alternating films, the reflected electromagnetic wave can be made to constructively interfere with other reflected waves from other layer pairs. Atop of the multilayer stack in EUVL reticles there is a patterned absorber layer, which blocks transmission to and reflection from the multilayer stack. Absorber films typically contain tantalum [44], shown by the opaque rectangles in Figure 18b. Tantalum based materials have many advantages over other technologies (chromium based materials for example) and are the best candidates for the absorber layer due to their high mass density, stability, conductivity, oxidation prevention capabilities and selective etching can be performed using chlorine chemistries [76,77]. There are two main candidates for the absorber stack, one of which is made up of a TaON antireflective sublayer, TaN bulk absorber layer, and ruthenium capping layer [78]. Another prominent candidate for an absorber stack is made up of a TaBO antireflective sublayer, a TaBN bulk absorber layer, and a CrN buffer layer with a silicon capping layer [77].

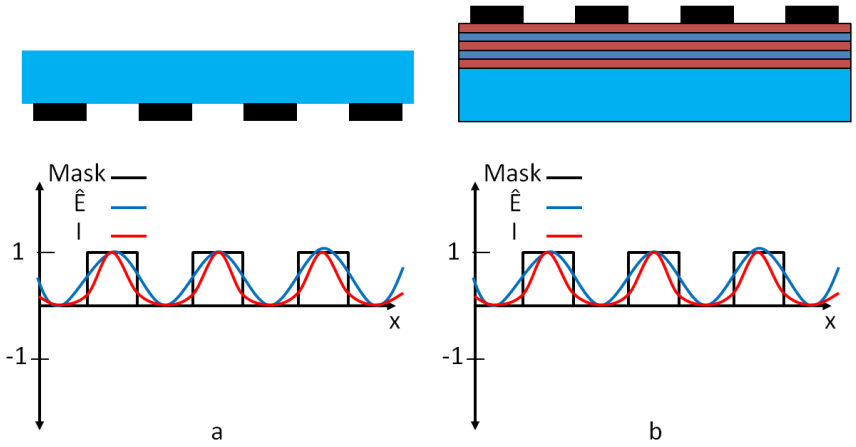

Figure 18: Typical ideal mask schematics, mask function, image electric field and image intensity of a) optical lithography and b) EUV lithography reticles

Some of the general performance metrics that are used in reticle fabrication are line CD variation, line width or edge roughness, proximity effects, minimum feature size, and defectivity [37,51,79–81].

1.4.1 *Phase Edges*

Certain phase objects can be very sensitive to aberrations, provided the illumination angle distribution is small and the phase difference is large. One such object is a phase edge with a phase shift of ideally of λ/2 [82,83]. The resulting image contrast can be twice that of a binary edge [84]. The ideal amount of the phase shift is given by Equation (1.10)

$$\Delta\varphi = \frac{2\pi}{\lambda}\left(n_\varphi - 1\right)t_\varphi \tag{1.10}$$

where n_φ is the index of refraction of the phase shifted medium and t_φ is the thickness of the phase shifted medium. Often a correction is needed when feature sizes become

smaller due to diffraction effects, these effects are modeled and can be incorporated into a phase edge design [85]. Figure 19 shows the imaging of a phase edge in an ideal optical lithography system with a constant threshold resist and t_{φ}.

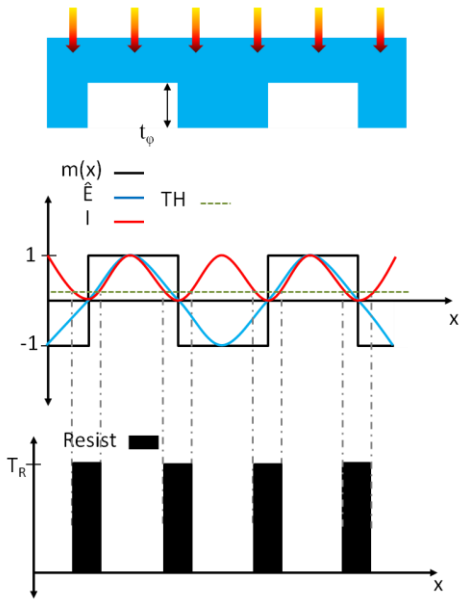

Figure 19: Imaging of phase edges using an ideal threshold resist

With the addition of aberration to the wavefront, OPD is induced in the different diffracted orders depending where they are in the pupil. The added OPD to the diffraction orders will cause image distortion, including CD errors and image shift. Aberrations can be described by a series of orthogonal polynomials know as Zernike polynomials. The primary Zernike odd polynomials are tilt and coma, and the even are power, astigmatism and spherical. More detail of the Zernike polynomials can be found in Section 2.2.

Figure 20 shows a simulation of resist lines printed with four phase edges with and without comatic aberration. The dimensions are 90 nm pitch with a 1:1 duty ratio,

imaged with coherent illumination, 0.25 NA and 13.5 nm wavelength. The signature behavior of coma aberration is CD difference between the left and right feature, which is present in the figure.

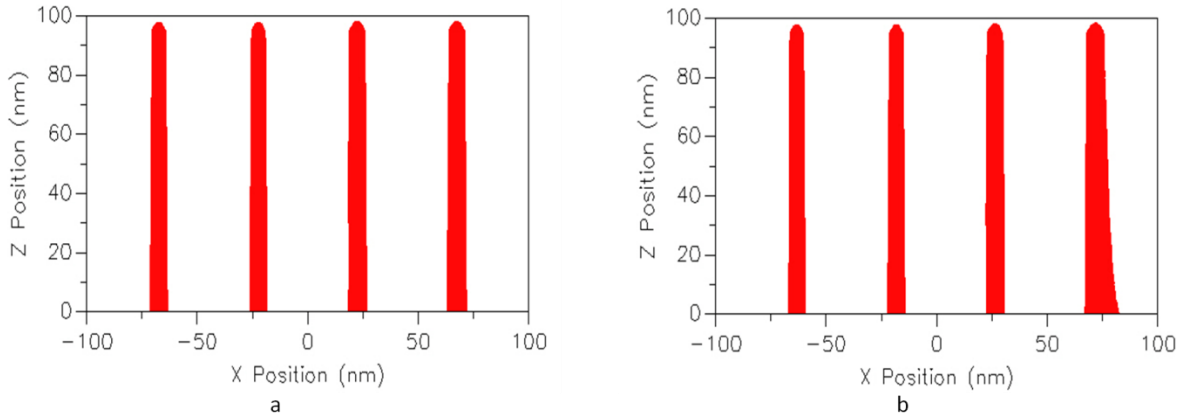

Figure 20: Simulation of four phase edges with a) no aberrations and with b) comatic aberration

1.4.2 *Phase Shifting Masks*

A phase-shifting reticle is a reticle that allows for areas on the reticle to transmit or reflect radiation that has longer interaction with the reticle causing an OPD or spatial phase change. Phase shifting reticles are considered a resolution enhancement technology (RET) because they increase the resolution of a lithography system by increasing contrast or doubling intensity frequency by modulating the electric field to negative values. In optical lithography, alternating phase-shifting masks (PSM) are fabricated by adding or removing material from the reticle by means of thin film deposition or plasma etch [4]. Figure 21 shows a schematic for a chromeless phase shifting reticle for both optical lithography and EUVL.

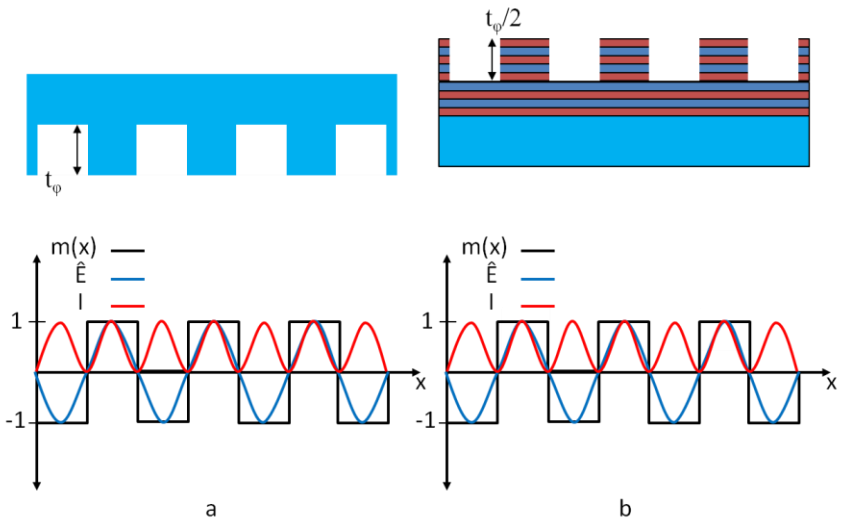

Figure 21: Chromeless phase shifting reticles for a) optical and b) EUV lithography

Sometimes it is advantageous to have a phase-shifted electric field in a dark field reticle. This can be achieved by allowing a small (3-10%) amount of light through the dark areas of the reticle with a 180º (π) phase shift from the clear areas. This is achievable by adding material to the reticle that is absorbing at the wavelength of interest known as an attenuated PSM [86], shown in Figure 22. The material must have the correct index of refraction and thickness to give the desired OPD and intensity [4,87–89]. In EUVL this is often not possible with one material so a composite of materials is used [44,87,90]. Figure 23 is a schematic of an alternating phase shifting mask for both optical and EUV lithography.

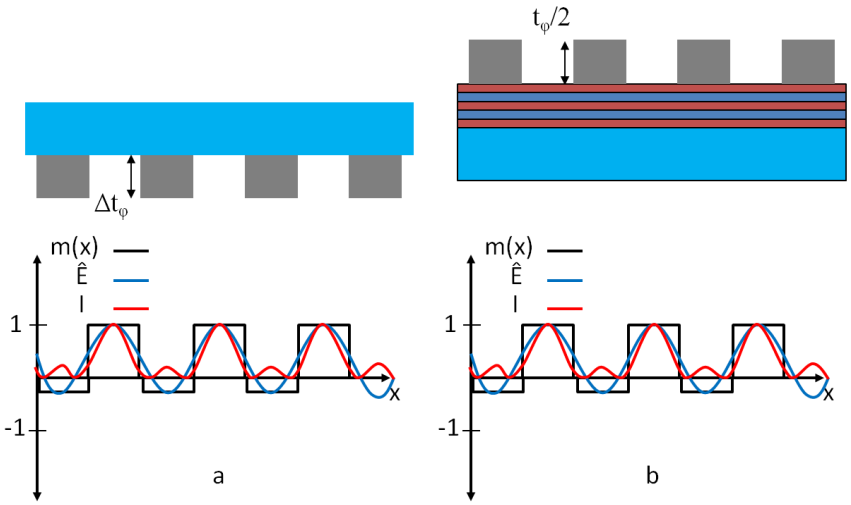

Figure 22: Schematic of an attenuated phase shift mask for both a) optical and b) EUV lithography

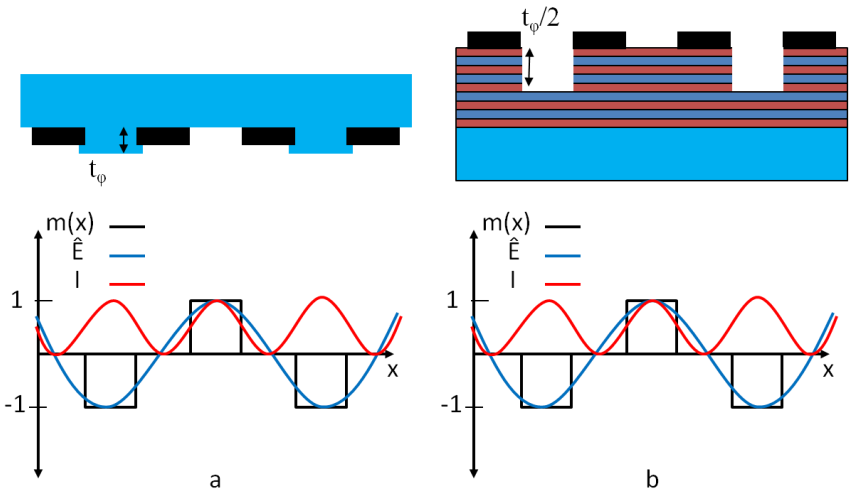

Figure 23: Schematic for alternating phase shifting mask for both a) optical and b) EUV lithography

1.5 Quality of an Optic

The quality of a lens or curved mirror can be described as its ability to converge a diverging spherical wavefront from a point object to a point image [91]. The term aberration describes the non-ideal propagating spherical wavefront resulting in image

blurring, focus shift, placement error, and distortion. Aberrations caused by optical elements are induced by imperfections or misalignment of that element, creating OPD of points on the propagating wavefront. OPD is defined as the distance a ray travels from expected multiplied by the index of refraction of the propagating medium.

In a lithographic tool, aberrations can significantly degrade imaging performance. CD variation tolerances determine the allowable levels of aberrations in a lithographic system. It is therefore crucial to determine aberration levels accurately and precisely during lens manufacturing and system use. During system use, several environmental conditions such as temperature, pressure, vibrations, misalignment, and other disturbances can affect the aberration levels by altering the optical and/or properties of the elements in the optical path. Any changes in the optical elements in the lithography system on the order of the wavelength being used will cause the imaging properties of the system to change. Also any temperature fluctuations or air density changes will cause the refraction index to fluctuate causing image performance degradation. Therefore it is critical to monitor aberration levels during system use as the environment of the lens can change during exposure and from day to day use. Once aberration levels are known, modern lithographic systems may have several deformable or movable lens to correct and control wavefront phase error.

2. IMAGING BACKGROUND

Mathematical methods are used to describe image formation from diffraction of an object. Aberrations in an imaging system can also be represented by a mathematical function. Several state-of-the-art methods to determine a systems aberration signature have been developed, including phase measuring interferometry, common path interferometry, shearing interferometry, phase shifting point diffraction interferometry, aerial image based tests, Hartman screen tests, and wavefront testing using lithographic images.

2.1 **Image Formation**

The performance of a lithographic system is ultimately determined by the minimum resolution of that system, which can be reduced drastically by the presence of aberrations. In lithography object transmittance is defined by the mask *m(x,y)*, which has magnitude and phase information. When illuminated by a coherent point source, its image at a distance *z* is given by the Fraunhofer diffraction integral and is shown in Equation (2.1). The expression in Equation (2.1) is simply the Fourier transform of the object [91] defined in the *(x",y")* plane with special frequencies *(u,υ)*.

$$E(x'',y'') = \iint_{-\infty}^{\infty} m(x,y)\, e^{-2\pi i(u\,x+v\,y)}\, dx\, dy \tag{2.1}$$

where $u=x''/(z\lambda)$ and $v=y''/(z\lambda)$. Therefore, the electric field impingent upon the objective lens is the Fourier transform of the mask pattern $M(u,v)$ as shown in Equation (2.2).

$$M(u,v) = \mathcal{F}\{m(x,y)\} \tag{2.2}$$

where $\mathcal{F}$ is the Fourier transform operator.

The NA of a lithography system determines the maximum diffraction angle the system can capture. Ideally, the pupil transmission is unity inside the NA limit and zero outside. The pupil function in terms of spatial frequencies can be given as Equation (2.3).

$$H(u,v) = \begin{cases} 1, & \sqrt{u^2+v^2} < NA/\lambda \\ 0, & \sqrt{u^2+v^2} > NA/\lambda \end{cases} \tag{2.3}$$

The final image in the (x'',y'') plane is the convolution of the mask function $m(x,y)$ and the pupil function $H(x',y')$ or the inverse Fourier transform of the product of the far field mask pattern $M(u,v)$ and the pupil function $H(u,v)$ shown in Equation (2.4).

$$E(x'',y'') = M_g\,\mathcal{F}^{-1}\{M(u,v)H(u,v)\} \tag{2.4}$$

where M_g is the magnification of the system, and $\mathcal{F}^{-1}$ is the inverse Fourier transform.

The mask function of a 1:1 line grating with no modulation in the y direction can be simplified to $m(x)$. The imaging of $m(x)$ in a diffraction limited lithography system is shown in Figure 24.

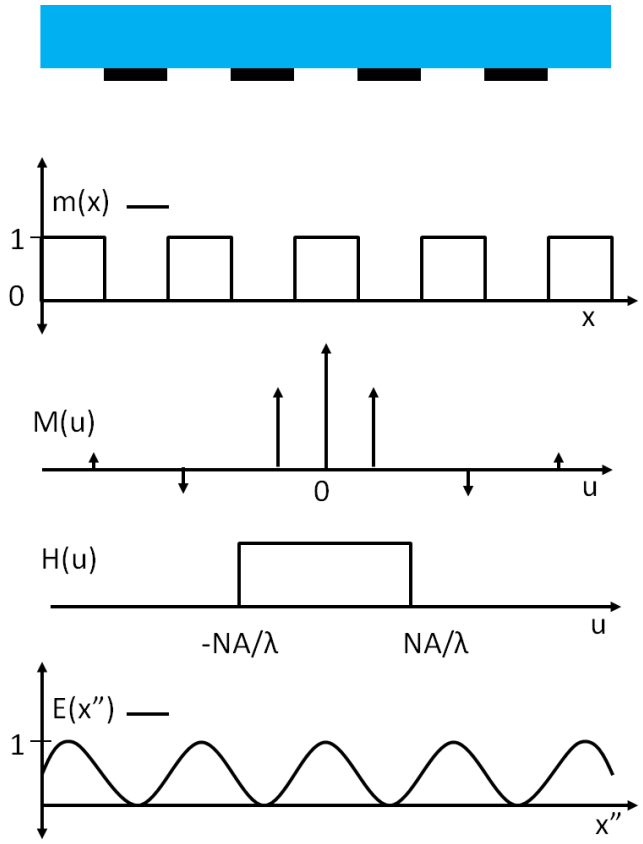

Figure 24: Imaging of an infinite grating with 1:1 duty ratio in a diffraction limited lithography system

2.2 **Aberrations in Imaging**

It is useful to describe the OPD of a wavefront in terms of phase error, often represented in terms of wavelength or in nanometers. The OPD of a wavefront in the pupil plane can be described by the aberration function *W(u,v)*. The generalized pupil function is given by Equation (2.5),

$$H'(u,v) = H(u,v)\, e^{jk\,W(u,v)} \tag{2.5}$$

where *H* is the un-aberrated pupil function shown in Equation (2.3) for an ideal case, *k* is the wavevector $2\pi/\lambda$, and *kW(u,v)* describe the phase error of the wavefront in the pupil.

It is useful to describe aberrations in terms of the shape of the wavefront. A wavefront is a constant phase surface that is normal to geometrical rays, aberrations describe the deviation of this surface from an ideal spherical surface. A point object will image to a point with no distortion if after the wavefront propagates through the optical system and it still has a perfect spherical wavefront. The converging rays from such a system will have no phase difference between them and will converge to a single point. In real optical systems, however, there are differences in phase of converging rays and the wavefront is deviated from a perfect spherical shape.

Consider an optical system where a point object is being imaged as seen in Figure 25. The example is comprised of a point object P_O, an optical system, and a point image. Consider a spherical wavefront propagating from P_O through the optical system. In an ideal case, the spherical wavefront would remain spherical throughout the system and emerge as the spherical wavefront S_f. The wavefront would then converge to a perfect image P_{II}. In a real system, however, the wavefront will not remain spherical and deviations from an ideal wavefront will occur when the wavefront propagates through the optical system. The real wavefront R_{f1} still has an ideal spherical shape, but once the wavefront enters the lens in the optical system, deviations from the ideal case are seen in R_{f2}. The real wavefront R_f will emerge from the optical system in the exit pupil with a non-ideal wavefront and will converge to an imperfect image P_{RI}. The imperfect image has both a shift in planar position, but also a shift in focus, as well as image distortion.

In geometrical ray tracing, the important planes are known as pupils. All object rays that will contribute to imaging enter the system in the entrance pupil and exit the

system in the exit pupil. Pupils are images of the front and rear physical limiting apertures of the optical system.

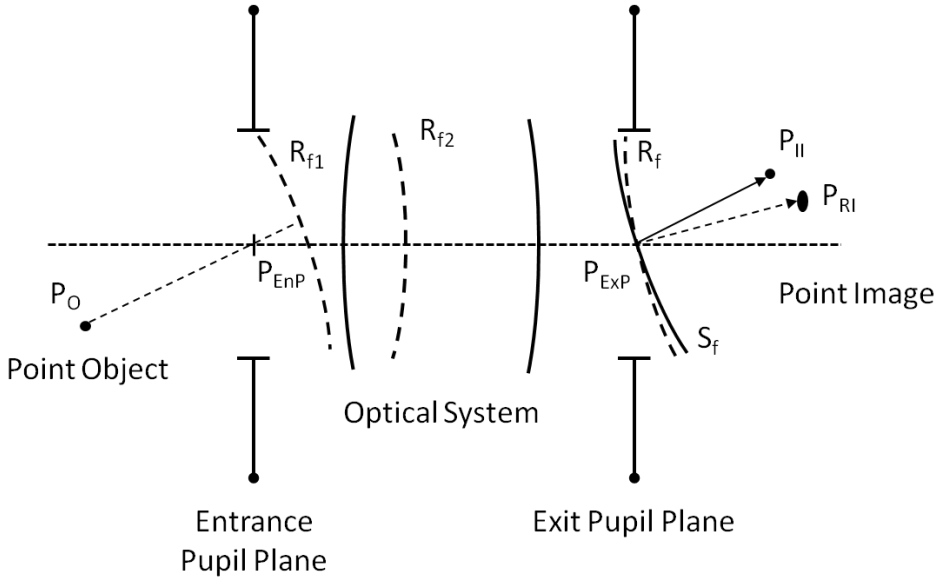

Figure 25: Illustration of geometrical optical imaging, showing ideal and real imaging

It is often customary to describe a wavefront as the deviation from an ideal wavefront S_f, called a reference spherical wavefront centered at a reference point knows as the Gaussian focus. Aberrations can be defined by the geometry shown in Figure 26, showing the wavefront propagating along the chief ray with and without aberrations. With P_{II} known as the Gaussian image point or ideal image. The ratio of the maximum intensity of the actual image point P_{RI} by the Gaussian image point P_{II} is known as the Strehl ratio [92,93], and is often used as a figure of merit for an imaging system. The reference wavefront shown as S_f, is defined as the spherical wavefront in the exit pupil with its vertex on the point P_{ExP} and center of curvature on the image point P_{II}. The wave aberration is then defined as the deviation of the wavefront R_f from the spherical reference wavefront S_f in the exit pupil, more specifically the optical path difference or

product of the distance and the image medium refractive index between the reference wavefront and actual wavefront. In Figure 26, the difference between the point p_I on the spherical wavefront and the point p_R on the actual wavefront multiplied by the index is defined as optical path difference (OPD) for that location in the pupil.

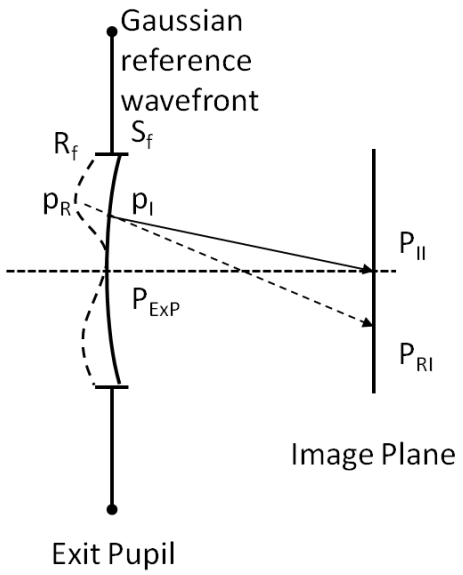

Figure 26: Diagram of wave aberration in a general system, showing an aberrated wavefront in the exit pupil

Consequently, a series of points on the reference and actual wavefronts can be subtracted from each other and a map of the OPD in the exit pupil can be produced. The reference map is what is typically reported as the aberration wavefront error function of an optical system.

2.2.1 *Zernike Polynomials*

The wavefront error function *W* is often described by a Zernike polynomial series $\{Z_n^m(\rho,\theta)\}$ that are a special case of the Jacobi Polynomial [83], allowing for an

aberrated wavefront to be separated into different aberration types each with their own effect on imaging. Zernike polynomials are an infinite series of orthogonal polynomials for a unit circle [94,95] and satisfy the orthogonality condition for a unit circle, shown in Equation (2.6). The polynomials are invariant about rotation in the origin and include polynomials for each permitted pair of *n* and *m*. The polynomial series arise from the expansion of a wavefront function of optical systems with circular pupils, where any arbitrary function in the pupil can be represented by a linear combination of Zernike polynomials.

$$\iint_{x^2+y^2\leq 1} G_\alpha(x,y)G_\beta^*(x,y)dxdy = A_{\alpha\beta}\delta_{\alpha\beta} \tag{2.6}$$

where $\{G\}$ is a set of polynomials in the real variables (x,y), G_α and G_β are typical polynomials from that set, * denotes the complex conjugate, $A_{\alpha\beta}$ is a constant of normalization, and $\delta_{\alpha\beta}$ denotes the Kronecker delta, which has a value of zero if $\alpha \neq \beta$. The Zernike polynomials are defined as the product of radial and trigonomic functions for integer values of n and l and taking $x = \rho\cos(\theta)$ and $y = \rho\, sin(\theta)$, as shown in Equation (2.7).

$$G_n^l(\rho,\theta) = R_n^l(\rho)e^{il\theta} \tag{2.7}$$

where $n \geq 0$, $n \geq |l|$, (ρ,θ) are the polar coordinates in the pupil plane, θ being the azimuthal angle, R is the radial function in ρ and is given by Equation (2.9). The polynomials that make up $\{G\}$ also include complex functions, but the Zernike polynomials that will be used are real functions. Therefore, taking the real functions

m=|l| and invoking Euler's formula ($e^{i\varphi} = \cos\varphi + i\sin\varphi$), Equation (2.7) can be written as Equation (2.8)

$$\begin{matrix} Z_n^{-m}(\rho,\theta) \\ Z_n^{m}(\rho,\theta) \end{matrix} = \begin{matrix} \frac{1}{2}[G_n^m + G_n^{-m}] \\ \frac{1}{2}[G_n^m - G_n^{-m}] \end{matrix} = R_n^m(\rho) \begin{matrix} sin \\ cos \end{matrix}(m\theta) \tag{2.8}$$

$$R_n^m(\rho) = \sum_{l=0}^{(n-m)/2} \frac{(-1)^l (n-l)!}{l!\left[\frac{1}{2}(n+m)-l\right]!\left[\frac{1}{2}(n-m)-l\right]!} \rho^{n-2l} \tag{2.9}$$

where n and m are integers with $n \geq m \geq 0$ and n-m is even otherwise $R = 0$. $R_n^m(\rho)$ is an even or odd polynomial depending on n being even or odd. The radial function is normalized such that when $\rho = R(1) = 1$ for all values of n and m, and $R_n^n(\rho) = \rho^n$.

For convenience, Zernike polynomials may be ordered with a single index j, instead of using coefficients n and m. The Zernike polynomials in Table 2 are listed using the "Fringe" index ordering [95,96], or Arizona convention, which uses the single positive value of $(n+m)/2$ for sorting. The Zernike polynomials are listed from increasing $(n+m)/2$ and decreasing m for a given $(n+m)/2$. An aberrated wavefront can then be described as a series of Zernike polynomials each with a weighting coefficient a_j, shown in Equation (2.10).

$$W(\rho,\theta) = \sum_{j=1}^{\infty} a_j Z_j(\rho,\theta) \tag{2.10}$$

Table 2: The first thirty six Zernike polynomial functions up to Z_{36}

$\frac{n+m}{2}$	m	j	$Z_j(\rho,\theta)$	Aberration name
0	0	1	1	Piston
1	1	2	$2\rho\sin\theta$	Tilt x
		3	$2\rho\cos\theta$	Tilt y
	0	4	$2\rho^2-1$	Power
2	2	5	$\rho^2\cos 2\theta$	Astigmatism
		6	$\rho^2\sin 2\theta$	Astigmatism 45º
	1	7	$(3\rho^3-2\rho)\cos\theta$	Coma x
		8	$(3\rho^3-2\rho)\sin\theta$	Coma y
	0	9	$6\rho^4-6\rho^2+1$	Primary Spherical
3	3	10	$\rho^3\cos 3\theta$	Trefoil x
		11	$\rho^3\sin 3\theta$	Trefoil y
	2	12	$(4\rho^4-3\rho^2)\cos 2\theta$	Secondary Astigmatism
		13	$(4\rho^4-3\rho^2)\sin 2\theta$	Secondary Astigmatism 45º
	1	14	$(10\rho^5-12\rho^3+3\rho)\cos\theta$	Secondary Coma x
		15	$(10\rho^5-12\rho^3+3\rho)\sin\theta$	Secondary Coma y
	0	16	$20\rho^6-30\rho^4+12\rho^2-1$	Secondary Spherical
4	4	17	$\rho^4\cos 4\theta$	Tetrafoil x
		18	$\rho^4\sin 4\theta$	Tetrafoil y
	3	19	$(5\rho^5-4\rho^3)\sin 3\theta$	Secondary Trefoil x
		20	$(5\rho^5-4\rho^3)\cos 3\theta$	Secondary Trefoil y
	2	21	$(15\rho^6-20\rho^4+6\rho^2)\cos 2\theta$	Tertiary Astigmatism
		22	$(15\rho^6-20\rho^4+6\rho^2)\sin 2\theta$	Tertiary Astigmatism 45º
	1	23	$(35\rho^7-60\rho^5+30\rho^3-4\rho)\cos\theta$	Tertiary Coma x
		24	$(35\rho^7-60\rho^5+30\rho^3-4\rho)\sin\theta$	Tertiary Coma y
	0	25	$70\rho^8-140\rho^6-90\rho^4-20\rho^2+1$	Tertiary Spherical
5	5	26	$\rho^5\cos 5\theta$	Pentafoil x
		27	$\rho^5\sin 5\theta$	Pentafoil y
	4	28	$(6\rho^6-5\rho^4)\sin 4\theta$	Secondary Tetrafoil x
		29	$(6\rho^6-4\rho^4)\cos 4\theta$	Secondary Tetrafoil y
	3	30	$(21\rho^7-30\rho^5+10\rho^3)\cos 3\theta$	Tertiary Trefoil x
		31	$(21\rho^7-30\rho^5+10\rho^3)\sin 3\theta$	Tertiary Trefoil y
	2	32	$(56\rho^8-105\rho^6+60\rho^4-10\rho^2)\cos 2\theta$	Quaternary Astigmatism
		33	$(56\rho^8-105\rho^6+60\rho^4-10\rho^2)\sin 2\theta$	Quaternary Astigmatism 45º
	1	34	$(126\rho^9-280\rho^7+210\rho^5-60\rho^3+5\rho)\cos\theta$	Quaternary Coma x
		35	$(126\rho^9-280\rho^7+210\rho^5-60\rho^3+5\rho)\sin\theta$	Quaternary Coma y
	0	36	$252\rho^{10}-630\rho^8+560\rho^6-210\rho^4+30\rho^2-1$	Quaternary Spherical

The first term in Table 2 is piston, which is a constant OPD across the pupil. Piston is does not degrade the wavefront, but adds a uniform delay in the whole wavefront, this is generally an artifact of the methodology employed. The second and third terms are

wavefront tilt around the x and y axis respectively. Tilt will cause wavefront shift to occur, creating also image shift placement, but no true degradation. The fourth term is power, which represents paraxial defocus. When considering the general case of defocus, the function is hyperbolic. The power and tilt (Z_2-Z_4) terms represent the Gaussian or paraxial wavefront properties.

Wavefront displacement or error is measured from the spherical reference wavefront. The center of curvature of that wavefront is close to the Gaussian image. Deviations from the spherical wavefront in transverse (x,y) directions will be seen as wavefront tilt, deviations in the longitudinal (z) direction will be seen as defocus. These errors can be eliminated through the appropriate leveling and focus of the reticle and wafer planes.

The first 36 polynomials are presented in Figure 27, the columns group the angular frequency (m) and the rows are grouped by ½(n+m). The angular frequency of each Zernike polynomial determines if the function will be symmetric around a unit circle.

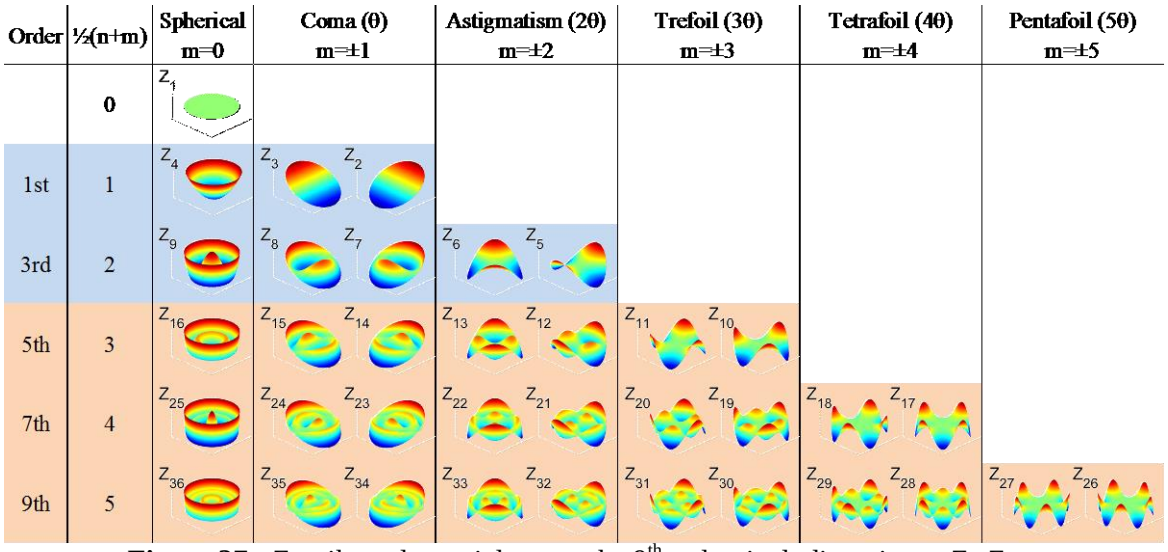

Figure 27: Zernike polynomials up to the 9th order, including piston, Z_1-Z_{36}

For even frequencies (m=2,4,6,...) there is symmetry along some axis, these functions are known as even Zernike polynomials. Odd Zernike polynomials have odd angular frequencies (m=1,3,5,…) and therefore no symmetry in a unit circle. Zernike polynomials with no angular dependence (m=0) have an infinite number symmetries and are therefore even functions. The total wavefront error can then be represented by a combination of even and odd Zernike polynomials: $W(\rho,\theta)=W_{even}(\rho,\theta)+W_{odd}(\rho,\theta)$.

The order of a Zernike polynomial aberration is identified by the value n+m-1. The term primary aberration is used frequently to describe a group of aberrations and includes the first and third order functions as seen as the blue shaded region in Figure 27. Polynomials often referred to as high order aberrations include the 5th, 7th, and 9th orders and are shown as the red shaded region in Figure 27.

2.2.2 *Aberrations in Annular Pupils*

Consider an optical system with an annular pupil, such that ε is the inner radius and the outer radius in one. It can be shown that annular Zernike polynomials can be derived that are orthogonal over an annular pupil [97–99]. Like the Zernike polynomials for circular pupils, the Zernike polynomials for annular pupils are polynomials in two variables, ρ and θ and are orthogonal over an annulus, invariant in form with respect to rotation about the origin, and include polynomials for each permitted n and m. By considering Equation (2.6) and changing the limits of integration as well as making the polynomial set G a function of ε, it can be rewritten to include a central pupil obscuration as shown in Equation (2.11).

$$\iint_{\varepsilon \le x^2+y^2 \le 1} G_\alpha(x,y;\varepsilon) G_\beta^*(x,y;\varepsilon) dxdy = A_{\alpha\beta}\delta_{\alpha\beta} \tag{2.11}$$

where $\{G\}$ is a set of polynomials in the real variables (x,y), G_α and G_β are typical polynomials from that set, * denotes the complex conjugate, $A_{\alpha\beta}$ is a constant of normalization, and $\delta_{\alpha\beta}$ denotes the Kronecker delta, which has a value of zero if $\alpha \neq \beta$. The Zernike polynomials are defined as the product of radial and trigonomic functions for integer values of n and l and taking $x = \rho\cos(\theta)$ and $y = \rho\, sin(\theta)$, as shown in Equation (2.12).

$$G_n^l(\rho,\theta;\varepsilon) = R_n^l(\rho;\varepsilon)e^{il\theta} \tag{2.12}$$

where $n \ge 0$, $n \ge |l|$, (ρ,θ) are the polar coordinates in the pupil plane where $0 \le \theta \le 2\pi$ and $\varepsilon \le \rho \le 1$, θ being the azimuthal angle, R is the radial function in ρ and is given by Equation (2.14). The polynomials that make up $\{G\}$ also include complex functions,

but again the annular Zernike polynomials that will be used are real functions. Therefore, taking the real functions $m=|l|$ and invoking Euler's formula ($e^{i\varphi} = \cos\varphi + i\sin\varphi$), Equation (2.12) can be written as Equation (2.13).

$$\begin{matrix} Z_n^{-m}(\rho,\theta;\varepsilon) \\ Z_n^{m}(\rho,\theta;\varepsilon) \end{matrix} = \begin{matrix} \frac{1}{2}[G_n^m + G_n^{-m}] \\ \frac{1}{2}[G_n^m - G_n^{-m}] \end{matrix} = R_n^m(\rho;\varepsilon) \begin{matrix} sin \\ cos \end{matrix}(m\theta) \tag{2.13}$$

$$R_n^m(\rho,\varepsilon) = N_n^m \left[R_m^n(\rho) - \sum\nolimits_{i\leq 1}^{(n-m)/2} (n-2i+1)\langle R_n^m(\rho) R_{n-2i}^m(\rho,\varepsilon)\rangle R_{n-2i}^m \right] \tag{2.14}$$

where n and m are integers, N is a normalization constant such that the radial polynomials satisfy the orthogonal relationship shown in Equation (2.15), $n \geq m \geq 0$ and $n - m \geq 0$ and is even otherwise $R = 0$. $R_n^m(\rho;\varepsilon)$ is an even or odd polynomial depending on n being even or odd. The expected value of $\langle R_n^m(\rho) R_{n-2i}^m(\rho;\varepsilon)\rangle$ is given by (2.16). The radial function is normalized such that when $\rho = R(1,\varepsilon) = 1$ for all values of n and m, and $R_n^n(\rho;\varepsilon) = \rho^n \sqrt{(1-\varepsilon^2)/(1-\varepsilon^{2(n+1)})}$.

$$\int_\varepsilon^1 R_n^m(\rho;\varepsilon) R_{n'}^m(\rho,\varepsilon)\rho\, d\rho = \frac{1-\varepsilon^2}{2(n+1)}\delta_{nn'} \tag{2.15}$$

$$\langle R_n^m(\rho) R_{n-2i}^m(\rho;\varepsilon)\rangle = \frac{2}{1-\varepsilon^2}\int_\varepsilon^1 R_n^m(\rho) R_{n'}^m(\rho;\varepsilon)\, \rho\, d\rho \tag{2.16}$$

3. ABERRATION MEASUREMENT METHODS

Optical systems used in photolithography have fixed conjugates; e.g. a point-like object has a point-like image in conjugate planes. The most common lens testing method (interferometry) uses these conjugate planes by having a diverging spherical wavefront generated from a point object letting it pass through the system and measuring the converging spherical wavefront at the image plane. Any deviation from a perfect spherical wavefront is the optical system's contribution to aberrations. In state-of-the-art, diffraction-limited lens manufacturing, interferometry refers to a class of wavefront measurement techniques that make use of coherent light to produce measurable intensity fluctuations or fringes. When coherent light passes through a test optic, the wave packet can be made to interfere with its delayed or shifted version, creating an interferogram. This interferogram can be used to measure the non-ideality of the test optic in terms of test wavelength. Using this method for EUVL, sub-nanometer accuracy (0.04 – 0.1 nm) and precision levels of 0.005 nm [45] can be achieved. Historically, there has been some debate over the usefulness of actinic (at-wavelength) optic testing as this is prohibitive due to source and detector costs, and visible wavelength tests offer comparable accuracies at lower costs due to the high cost of the optics, source, and vacuum equipment needed for EUV. However, in EUV systems, it was found that the defects under reflective multilayer stacks lead to image defects that will actually print in photoresist. The defects under the multilayer stack cause phase error in the reflected beam directly above the defect by shifting the effective reflection plane, which is in the multilayer, to a higher position than the surrounding area. This localized phase error is

what causes the defect to print. These defects are not always detected by visible wavelength interferometry because the surface of the multilayer over buried defects may remain flat and visible light interferometry may only probe surface roughness. Therefore, actinic reticle inspection is deemed necessary for EUV lithography to assist in reticle repair and the fabrication of optics [44].

Several interferometer methods using a common optical path interferometer have been used for in-situ measurements, such as point-diffraction interferometry (PDI) [100,101], phase-shifting point-diffraction interferometry (PSPDI) [70,102,103], and shearing interferometry [104]. Other non-interferometric methods used in aberration characterization include knife-edge test [105], screen tests [106,107], Ronchi tests [84,108], point spread function (PSF) methods [84], aerial image based methods [59,63], Hartmann screen tests [45,61,106,107], and wavefront estimation from lithographic images [58,69,71,109]. While all these tests provide highly accurate measurements, some are difficult to carry out during use of a photolithography system, as they require integration of a sensor efficient at the actinic wavelength or the integration of secondary optics for off-wavelength integration suitable for high resolution measurements, and access to conjugate planes. However, use of lithographic images does not rely on an actinic image sensor, which is currently a concern for EUVL [110], but merely relies on measurements on well characterized photoresist patterns.

With the progress in powerful computing, simulation software that can solve fast Fourier transforms (FFT) of complex masks and accurately predict resist images through stochastic modeling has become very sophisticated. For example, the use of the rigorous coupled wave analysis (RCWA) algorithm [111] to solve Maxwell's equations [112], the

Hopkins model of imaging [113–115]. The added simulation capabilities allow for new methods of determining lithographic aberrations. Some of the significant milestones achieved with lithographic images include phase shift focus monitor test [109], phase or blazed gratings at various angles [116,117] and phase edge printing with a $\lambda/2$ phase shift [58,71]. These methods infer what aberrations are present by measuring printed patterns, most often in photoresist, and simulate the effect of aberrations on that pattern. This has been proven useful for aberration control and characterization during full system use because it can be completed in a production exposure environment. Photoresist methods rely on specific targets that are sensitive to a certain aberrations. These methods have been investigated in the past for DUV lithography [69,72,73,109] and a similar approach can be extended to EUV lithography. Features that have been used in DUV investigations include phase edges [58,71], alternating PSM [69], three or five bar structures [69,72,73], DRAM isolation pattern [59,69,72,73], and line critical dimension (CD) in various orientations [59,69]. Phase structures have a higher sensitivity to pupil wavefront error than binary structures [58,71,89] and can therefore extract more aberrations with unique solutions. These structures are often coupled with variations in illumination shape, NA, exposure dose, focus, and feature size to give more accurate results [58,62,69,71–73,84,109].

3.1 **Phase Measuring Interferometry**

Some of the greatest achievements in optics fabrication have historically been driven by the demands from lithographic systems in the semiconductor industry, as their tolerances are far higher than most applications. These demanding requirements have

been met with equally demanding metrology accuracies. Phase measuring interferometry (PMI) is the most accurate method of measuring an optic's quality during fabrication and is used exclusively in the manufacturing of lithography systems today. The technique, also known as phase shifting (stepping) interferometry (PSI) [118], makes use of a time-varying phase shift between the reference beam and the test beam. Interferograms are collected over the field of the imaging system with time-varying phase shifts in an interferometer. The accuracy of PMI is far greater than static tests and can be attributed to the ability to eliminate systematic variations in the measurements seen in static tests [118].

The following analysis will derive the intensity fringes seen in the PMI method. Given an optic's surface height errors *h(x,y)*, Equation (3.1) shows the wavefront error for normal incidence measurements.

$$\phi(x,y) = 4\pi h(x,y)/\lambda \tag{3.1}$$

where x and y are spatial coordinates and λ is the wavelength. The general expressions for the test and reference wavefronts are:

$$W(x,y)_r = a_r(x,y)e^{i[\phi_r(x,y)-\delta(t)]} \tag{3.2}$$

$$W(x,y)_t = a_t(x,y)e^{i\phi_t(x,y)}, \tag{3.3}$$

where $a_r(x,y)$ and $a_t(x,y)$ are the reference and test wavefront amplitudes, $\varphi_r(x,y)$ and $\varphi_t(z,y)$ are the reference and test wavefront phases, and $\delta(t)$ is the time-varying phase shift introduced between the reference and test beams. $\delta(t)$ can also result in unintentional changes in either the reference or test beams [118].

The resulting intensity from the interference of the test and reference beam is given by Equation (3.4) and is furthered simplified by Equation (3.5)

$$I(x,y,t) = |w_r(x,y,t) + w_t(x,y,t)|^2 \tag{3.4}$$

$$I(x,y,t) = A + B\cos\big(\phi_t(x,y) - \phi_r(x,y) + \delta(t)\big), \tag{3.5}$$

where $A=a_r^2 + a_t^2$ is the average intensity and $B= 2a_r a_t$ is the fringe modulation. Taking $\varphi(x,y)=\varphi_t(x,y)-\varphi_r(x,y)$ as the phase difference between the test and reference beams, Equation (3.5) becomes Equation (3.6)

$$I(x,y,t) = A + B\cos\big(\phi(x,y) + \delta(t)\big), \tag{3.6}$$

which is the fundamental PMI equation.

The intensity of each point in the interferogram is modulated by a sinusoidal function with an introduced temporal phase shift $\delta(t)$ and an offset $\varphi(x,y)$ which is the unknown wavefront phase error. In an experimental test, the values for the three unknowns in Equation (3.6) can be extracted easily from the resulting interferogram. A is the average intensity, B is the amplitude of the modulation, and φ is related to the shift in the peak intensity from zero offset.

Precise interferometry requires stringent control of environmental variables such as vibrations; this will cause noise in measurements and uncertainty in results. A more significant limitation of PMI is that a separate path interferometer such as a Twyman-Green, Fizeau, or Mach-Zehnder is needed. The need for a perfect and separate optical path makes in-situ measurements difficult due to environmental differences in the two paths. These different environments are often caused by vibrations in the reference and

test paths, creating unpredictable shifts in the measured phase difference. Due to strict requirements and the need for coherent light, conventional interferometry methods are not suitable for photolithography after tool assembly, and a common path interferometer is preferable for in-situ measurements.

3.2 **Shearing Interferometry**

Shearing interferometry is a wavefront measurement technique that makes use of interference between sheared copies of the incident beam. The beam is split before the test optic and this split beam is then subjected to a shift, rotation, or radial shear, hence the name of the technique. The shear interferogram yields an interference pattern that represents the phase difference between test and sheared beams over the shifted distance. When the shear distance is small, the resulting intensity pattern is proportional to the phase gradient in the shear direction. Therefore a set of interference pattern with orthogonal shear directions is needed to be able to reconstruct a wavefront.

Shearing interferometry has been adapted to lithography systems. One such adaptation is called integrated lens interferometer at scanner (ILIAS) and is based on a lateral shearing [119]. The ILIAS method uses a point source made by an opaque reticle with a clear point. In the wafer or imaging plane the point is split or sheared by several diffraction gratings in different orientations. The sheared beams are then interfered in the far field. The resulting interferograms can be used to reconstruct the exit pupil plane wavefront. This method is capable of accuracies and precisions of 2.5 mλ and between 0.5 mλ and 2.5 mλ at 193 nm wavelength [119].

3.3 **Phase Shifting Point Diffraction Interferometry**

Phase shifting point diffraction interferometry (PSPDI) is another method used to characterize lithography tool aberrations [70,103,120]. The PSPD interferometer is another common path interferometer, similar to the ILIAS method having a point object, but uses a diffraction grating sending two beams through the optic under consideration. One beam being the zero order, and the other a higher diffraction order sent through the edge of the optic. This second beam is then filtered using another point object, creating an aberration free spherical wavefront for a reference beam. Interferograms are collected for various gratings allowing for full pupil mapping. The process uses similar algorithms used in the PMI technique to reconstruct the pupil wavefront. This method is capable of accuracies of 0.06 nm and precisions of 6 nm for small NA lens at 13.5 nm wavelength [103,104,121]. For EUVL application, this method has only been demonstrated using a synchrotron and has not been shown effective in other sources, such as DPP and LPP, which will be the sources of choice for EUVL due to their lower cost and availability. These sources will have lower coherence than that of a synchrotron beam and may not be effective for PSPDI. Another consideration is that as EUVL systems are fabricated with higher NAs and become more complicated, it may be difficult to access the desired location of the interferogram, requiring additional optics.

3.4 **Aerial Image Based Tests**

There have been several investigations of aberration testing by measuring the aerial image of different objects with an image sensor [122]. The method relies on

effects of different aberrations on different objects such as best focus and image shifts. The objects that are used in these tests are chosen for their sensitivity to a family of aberrations. In lithography, this method has been employed to track best focus shifts, and lateral and vertical shifts during system use. These shifts are then correlated to aberration changes. Transmission image sensor at multiple illumination settings (TAMIS) [59] uses a grating on the reticle stage and a detector just under the grating. There is a second detector on the wafer stage measuring the intensity of the image of the grating. When the system is aligned and at best focus, the intensity is maximum, and when the system is out of focus or misaligned the intensity is less. By measuring best focus shifts, spherical aberrations (Z_9 & Z_{16}) can be determined.

Aberration induced effects can be measured by imaging different objects that are sensitive to an aberration or varying NA and partial coherence (σ). In the TAMIS method eight different illumination settings are chosen to determine select higher order aberrations. Using this array of different NA and σ combinations coma (Z_7, Z_8, Z_{14}, Z_{15}), spherical (Z_9, Z_{16}), orthogonal secondary and tertiary astigmatism (Z_{12}, Z_{21}) can be determined. Higher order and other aberrations such as trefoil cannot be determined by this method because trefoil is not sensitive to line gratings. Tilt (Z_2, Z_3) and primary astigmatism (Z_4, Z_5) cannot be accurately determined by this method due to a need for a well matched reticle and wafer stage image sensor.

After data is collected over the array of optical settings, linear models are created and Zernike values are fit by simulation. The models are created by simulating the effect of an aberration with a certain Zernike coefficient value on a metric such as image shift

and best focus shift. This method has produced results with accuracies of 1 nm for 193 nm wavelengths and the three sigma (3σ) repeatability of 3 nm [123].

The TAMIS method allows for quick measurements of aberration levels, with a device that is integrated into a lithography system. Having this capability integrated into the tool, allows for in-situ measurements and corrections. Though powerful, it has been challenging to implement in EUVL due to image sensor variability [110].

3.5 **Hartmann Screen Tests**

The Hartmann sensor named after its inventor was developed in 1900 [106]. The Hartmann wavefront sensor (HWS) uses a noninterfermetric technique with a much lower coherence requirement and higher overall efficiency. It consists of an array of apertures on the order of the wavelength, whose diffraction pattern is projected onto a screen or in modern techniques a CCD array. Figure 28 shows a schematic of the operation of a Hartmann sensor with a charge couple device (CCD) image sensor as a backplane. The wavefront travels to the sensor and each of the apertures or pinhole acts as an optical lever, displacing the diffracted spot proportional to the average phase tilt over the aperture. The relative phase tilt can then be calculated by measuring the displacement of the diffracted spot from a reference spot.

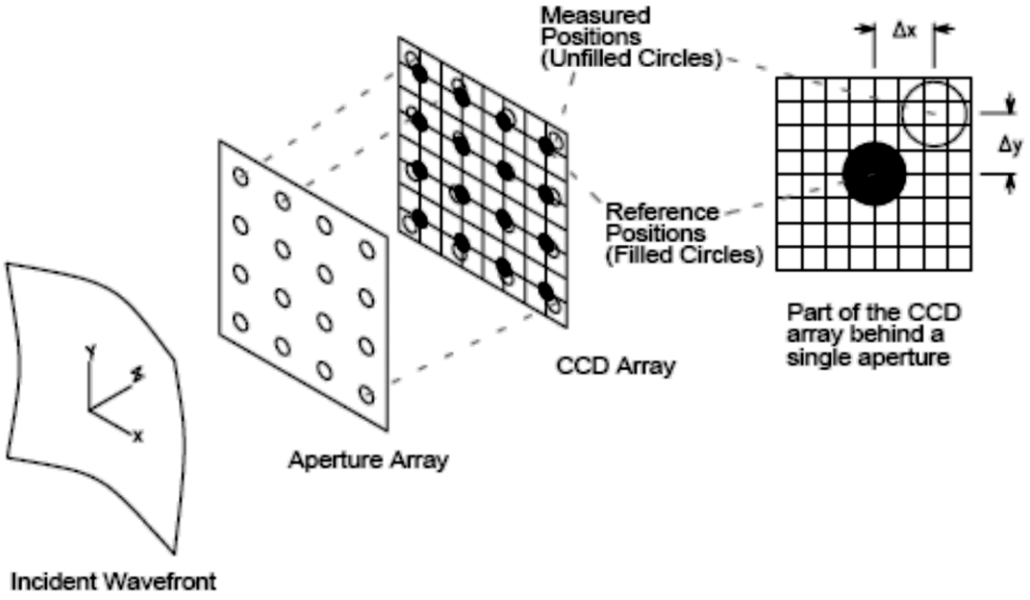

Figure 28: Drawing of a Hartmann wavefront sensor operation. The wavefront propagating along the z-direction is diffracted by the aperture array and the first order diffraction spots illuminate a CCD array. The black spots being reference non aberrated wavefront diffraction locations [124]

In the Hartmann sensor, once the curvature or slope of the incident wavefront is known, the wavefront can then be modeled and corrected using adaptive optics techniques.

The method used to determine the curvature of the wavefront in a Hartmann sensor is relatively straight forward. A displacement is measured in both *x* and *y* directions and based on Equations (3.7) – (3.10), which is derived from simple geometry as can be seen in Figure 29, the slope of the wavefront is determined.

$$\Delta x = z\,\frac{slope_x}{\sqrt{1+slope_x^2}} \tag{3.7}$$

$$slope_x = \sqrt{\frac{\Delta x^2}{z^2 - \Delta x^2}} \tag{3.8}$$

$$\Delta x \cong z\, slope_x \tag{3.9}$$

$$slope_x \cong \frac{\Delta x}{z} \tag{3.10}$$

where z is the distance from the pinhole to the screen, Δx is the displacement in the x direction from a un-aberrated reference point and $slope_x$ is the average curvature of the wavefront over the pinhole. Since the displacement of the spot is much less than the distance to the screen, z^2-Δx^2 can be approximated to z^2.

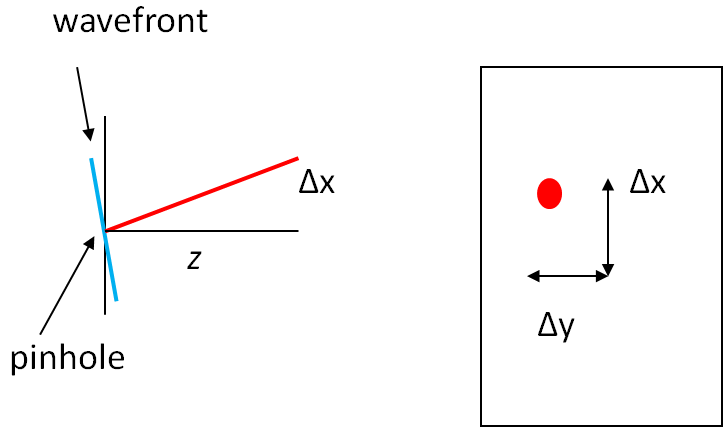

Figure 29: Drawing of the method used to determine the curvature of a wavefront in a Hartmann sensor

Once the slopes are determined for each pinhole the wavefront can be reconstructed by either zonal or modal reconstruction. Zonal reconstruction uses an integration tool to sum the parts of the wavefront starting at one point and indexing over the whole array. Modal reconstruction uses polynomials to fit coefficients to match the wavefront [106,107,124].

The first type of zonal reconstruction, linear integration is the simplest method to reconstructing a wavefront. Linear integration starts at one end of the incident wave and sums the heights (*H*) in steps of the pinhole spacing (*D*) as seen in Equation (3.11).

$$H_{n,m}^{x} = H_{n-1,m}^{x} + slope_{n-1,m}^{x}\, D \tag{3.11}$$

While the dynamic range of a Hartmann sensor is much greater than that of a traditional interferometer, its sensitivity does have limitations. To make Hartmann sensor more sensitive the image distance can be increased, increasing the displacement of the spot as per Equation (3.10). But as the image distance get larger; the dynamic range of the system is reduced. This is due to cross talk of adjacent pinholes. If the aberration is too large the rays will cross in mid air and arrive at the CCD on the incorrect cell. Also for lithographic systems, the Hartmann test is difficult to implement on large NA systems due to the size constraints on the detector [45].

A variation of the Hartmann screen test for lithography systems has been developed by Litel [125,125]. This method uses three box or a pinhole array on the reticle plane and projects this array through the lithography system on the wafer plane. This method shows promising results for optical lithography having 0.008 wave repeatability [61]. However, this technology is difficult to implement in EUVL because the feature spacing on the reticle would have to be on the order of the wavelength. The spacing on the reticle determines the sampling of the pupil, making it difficult to map a full field pupil with great detail using this method.

3.6 **Lithographic Images Used for Wavefront Testing**

Like the TAMIS test, lithographic images can be used in-situ to extract wavefront aberrations. There has been significant interest in using printed images as an alternative to an aerial image based test. Like aerial image based test, the effects of different illumination conditions and test patterns on the image are leveraged to determine the wavefront aberration levels.

The basic concept of using lithographic images to determine wavefront aberration is to make use of different objects that are highly correlated to changes in specific areas of the pupil plane. This will create the greatest sensitivity for a given object and a given aberration. An example of this is the left-right CD difference of a five bar structure and coma, shown in the top second from the left of Figure 30. The images of such objects can be simulated with various levels of aberrations and compared to printed images. The accuracy of this method can be furthered increased by including variations of the object and the illumination. Focus and dose variations can be leveraged to increase accuracy. Figure 30 shows some examples of targets that have been used to extract wavefront error in a lithographic system and the corresponding aberration it is sensitive to.

Binary Mask Structure	{CD ver} – {CD hor} 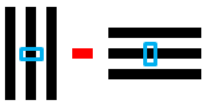	{CD left} – {CD right} 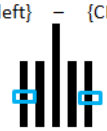	{CD left} – {CD right} 	CD Through Pitch 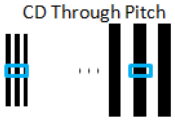
Aberration Sensitivity	Astigmatism	Coma/Trefoil	Trefoil/Coma	Spherical
Phase Mask Structure	Phase edge shape/ CD 	Phase edge shape/ CD 	FEM Tilt/ Delta CD 	Defect Printing 
Aberration Sensitivity	All	All	Coma/ Spherical	All

Figure 30: Targets that have been used in the past to extract aberrations from a lithographic system and the aberrations the target was used for [60,62,69,72,73,119]

Using print based methods in a partial coherent system causes some unavoidable pupil averaging, reducing the effects of aberrations on printed images as shown in Figure 31 as the red areas, and while this may be beneficial to manufacturing integrated circuits, for the purposes of extracting aberrations it is not ideal. A more ideal case would be a coherent illumination, shown by the blue arrows and lines in Figure 31.

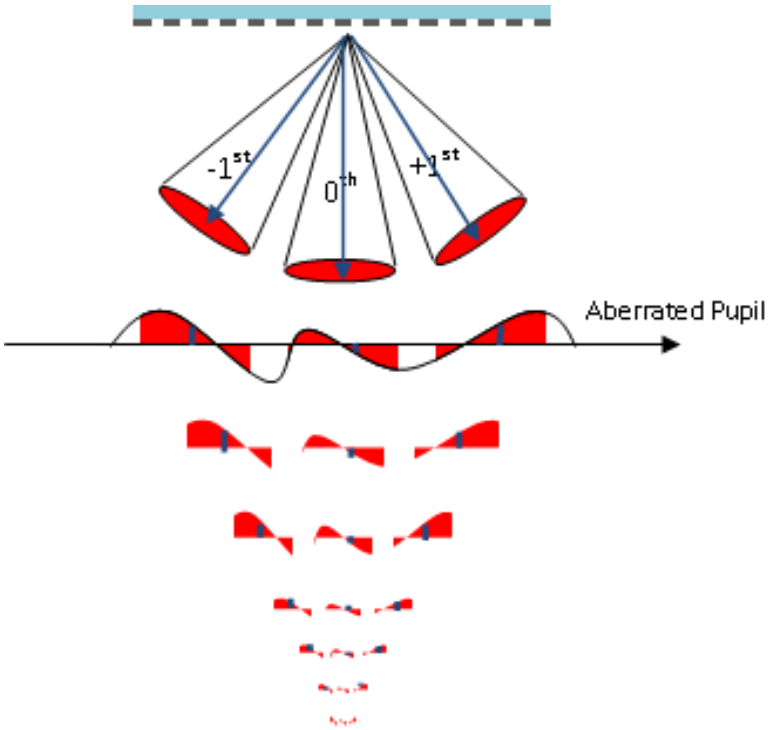

Figure 31: Figure depicting pupil averaging from a coherent and partial coherent optical system

Resist based tests are ideally carried out with a highly coherent source (low σ) to decrease diffraction order spread and increase sensitivity. For example, Figure 32 shows the image placement error caused by 40 mλ of coma of an isolated space. As partial coherence is increased there is more averaging in the pupil wavefront and less image shift is seen.

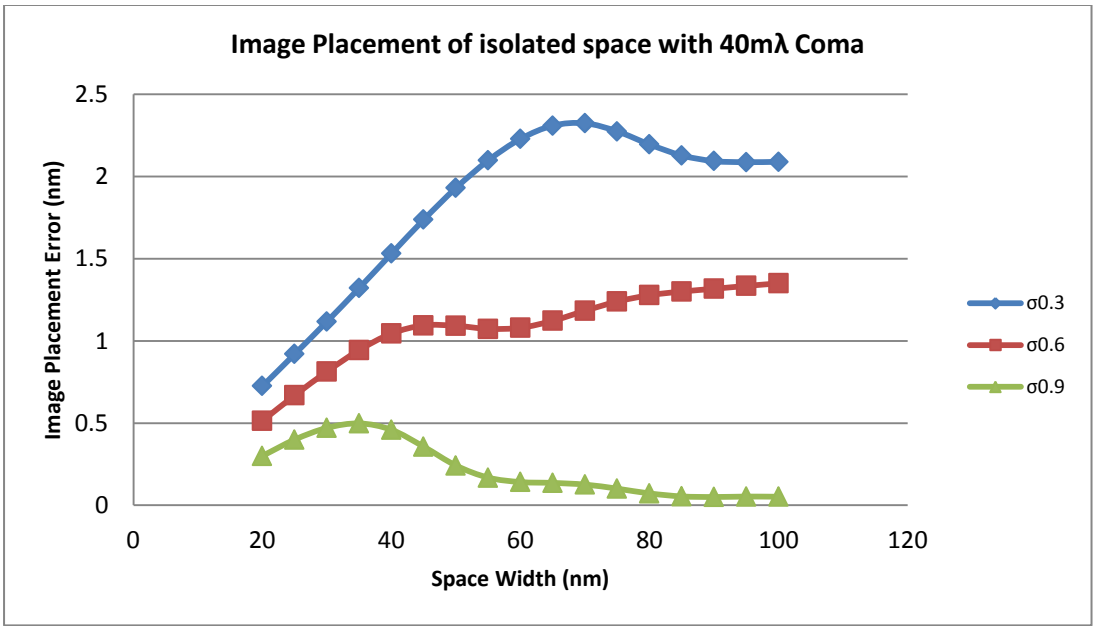

Figure 32: Image placement error of an isolated space imaged with the presence of 40 mλ coma (NA 0.25, λ 13.5 nm)

3.6.1 *Binary Structures*

Binary structures are used with some success to determine wavefront aberration [126]. The top left corner of Figure 30 shows the CD difference of horizontal and vertical lines and this structure is useful in extracting astigmatism. Astigmatism causes a best focus change between horizontal and vertical lines. The through focus behavior of CD follows a quadratic function that is centered on best focus. With no astigmatism the two orientations of lines will print with no CD difference, assuming no other effects such as EUV 'shadowing'. With some astigmatism the best focus for each orientation of lines will be shifted in opposite directions, causing a CD difference that changes for each focal point. This change can be approximated by a linear line for restricted focus values. This line can then be correlated to an astigmatism value through the use of lithographic simulation. When the 'shadowing' effect in EUVL is considered there is a constant CD

difference that is added through focus. This can be accounted for in the lithography simulation, or the slope of the line can be fit, ignoring the offset.

One example of such a method uses binary gratings in various orientations and two pitches. The gratings are imaged with ±0°, ±30°, ±60°, and ±90° orientations under fully coherent illumination through focus. This method is simplified to 3 beam interference under ideal conditions: monochromatic and coherent source, and perfect alignment. This method is capable of extracting individual Zernike terms with precisions and accuracies of λ/50 [127].

The feature to the right of the binary lines in Figure 30 is a five bar structure. This structure has a diffraction pattern that interacts with the part of the pupil that coma effects, causing a CD difference between the 1^{st} and 5^{th} bar. Lithography simulation can again be used to predict this with a given amount of coma and a coma value can be extracted [73]. Because coma is an odd aberration, this effect is not depend on focus like even aberrations such as astigmatism because the function is not symmetric about the pupil and can therefore be fit separately.

Trefoil has rotational symmetry in the pupil of 120° and can be extracted with a brick like test structure such as the one shown in top second from the right of Figure 30. This is a common structure used in DRAM isolation and has symmetry in the 120° orientation. In the presence of trefoil, the left and right CD of the bar will print differently, causing an offset, trefoil can then be extracted using lithographic simulations [72].

3.6.2 *Phase Gratings*

Using the benefits of the phase edge that is discussed in Section 1.4.1, phase shifted gratings shown in the bottom second from the right of Figure 30 can be used to monitor focus and aberration in a lithography system. One approach uses phase gratings in one orientation to monitor focus [116,128]. This method also provided a lumped estimate of low-order aberrations. There is however, no discrimination between aberration types, therefore comprehensive pupil mapping is not possible. By adding various orientations of phase gratings, a more complete mapping of the pupil is accomplished [108]. The methodology uses the diffraction orders from the grating to sample isolated portions of the lens. The gratings are then imaged with different focus steps and printed in photoresist. The lens can then be mapped by using several different orientations of gratings, 0 to 337.5 degrees in 22.5 degree steps and comparing the results to simulated print image. Using this method, low and high order aberrations have been determined within 12% of RMS OPD of the measured wavefront by other means [109]. This method has further been improved by lowering partial coherence, thereby measuring a smaller portion of the lens at once, and using multiple grating pitches, allowing for more complete mapping of the pupil.

3.6.3 *Phase Disk*

One technique used to reconstruct an aberrated wavefront takes advantage of a $\lambda/2$ phase edge object [58]. This method can be used in-situ and be able to correlate image intensity to pupil phase, or determining the modulation of phase in the pupil or aberration level by the intensity profile in the image plane. A test that uses this principle of a phase

edge is the aberration ring test (ART) [58]. The method uses an object with a phase shift of λ/2 from the surrounding transparent background and has a diameter of ~λ/NA. The structure appears as a ring in the image plane due to the transition of the electric field from 0 to λ/2 phase. The phase ring is imaged through focus with variations in illumination conditions. The images are analyzed and metrics such as ring width are used to create models. These models are then used to determine aberration levels. This method has been shown to extract up to 25 Zernike coefficients with a precision of 0.006 to 0.020λ depending on aberration type [59].

3.6.4 *Aberration Specific Resist Tests*

Another resist based method makes use of targets that respond to a specific aberration [129]. In the center of the target is a sub-resolution probe surrounded by a chrome ring and a unique phase pattern. The pattern is made up of concentric rings with phases of 0 or λ/2. This pattern is designed in such a way to direct energy into the probe center, if the aberration in question is present. Each probe is designed to respond with a high sensitivity to the desired aberration and for even and odd aberrations fabricated with phases of λ/4 and 0 respectively. To achieve high sensitivity of the designed targets, the partial coherence must be low. The maximum sensitivity of these targets can be achieved only with a coherent source. The concept is experimentally validated by achieving 0.01λ error RMS when predicting individual aberrations [129].

3.6.5 *Phase Wheel*

The extension and combination of phase gratings and phase disks is the phase wheel [71]. The technique uses λ/2 phase disks with a primary disc in the center surrounded radially with eight secondary discs. To obtain more detailed information and full mapping of a pupil, a simple phase grating in one direction is inadequate. Phase gratings in multiple orientations would be needed to fully map a pupil. A phase wheel takes the idea of multiple gratings in four orientations and combines them into one structure, as seen in Figure 33. The printed result is a set of nine rings that each respond differently to the same aberration because they each sample unique portions of the pupil. The phase wheel is imaged through focus with variations in illumination, NA, and target dimensions. The images are then processed, extracting contours and CD of the target. Compact models are made with simulations, which describes the behavior of the rings under the different imaging conditions and targets. The compact model is then used to produce a best fit of aberration coefficients using a global search method.

A phase wheel is a π-phase structure that is able to sample larger and unique areas of the pupil [60,71,130–134], without increasing data collection and computation time, through interaction of phase components. The disk features are sized between 0.5 and 1.5 λ/NA, with the total structure being between 2.5 and 5 λ/NA, and the features are at 0°, 45°, 90°, 135°, 180°, 225°, 270° and 315° in azimuth. The number of features, size, phase, shape, density, and transmission can be varied to produce unique detection of aberrations. For example, as discussed previously even aberrations will respond to focus variations, while odd aberrations do not. This can be leveraged along with different source shapes to probe the pupil in a meaningful way. Figure 34, 35, and 36 show the

effects of third order aberrations (astigmatism, spherical, coma and trefoil respectively) on the printing of a phase wheel target.

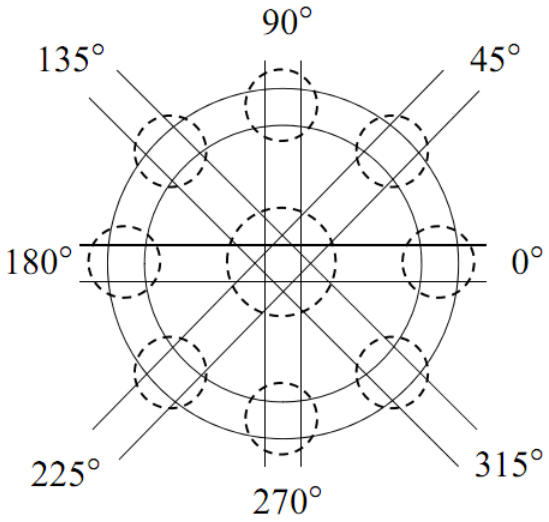

Figure 33: Design of a phase wheel target [68]

Figure 34, 35, and 36 show simulated resist images of a phase wheel target with dimensions of L1=100 nm, L2=150 nm, and L3=200 nm imaged at a wavelength of 157 nm and a NA of 0.85. The phase wheel structure is shifted 180° from the surrounding area. The entire target has 100 percent transmission; the printed features are the result of destructive interference of the phase edge as explained in Section 1.4.1.

Even aberrations (n,m is even), such as astigmatism and spherical have symmetry in the xy plane. The effect of even aberrations on imaging is best observed with defocus. Figure 34 (a) shows the result of negative third order astigmatism x (Z_5) through a defocus of ~1.5 waves or ±0.12 microns. The result is the resist image of the disks in the x and y orientations is deformed with a non zero defocus value. With positive defocus the rings in the +y and –y are open toward the center of the structure. With negative

defocus, the rings in the +x and –x directions are open toward the central ring. Figure 34 (b) shows the imaging result of positive third order astigmatism x with ± 0.12 microns defocus. Compared to the negative astigmatism case, defocus causes the exact opposite response from the phase wheel target. With positive defocus, the +x and –x rings are open toward the center, and with negative defocus the +y and –y rings are open toward the center of the structure. In the case of third order astigmatism y (rotated 45° from astigmatism x) the main deformation is on the 45° orientated rings. Figure 34 (c) shows the case of positive astigmatism y with positive defocus the rings on the 45° (clockwise is +) axis are open toward the center and for negative the rings on the -45° axis are open toward the center. Figure 34 (d) shows the case of negative astigmatism y, with a positive defocus, the rings on the -45° (clockwise is +) axis are open toward the center and for the case with negative defocus, the rings that are on the +45° axis are open toward the center.

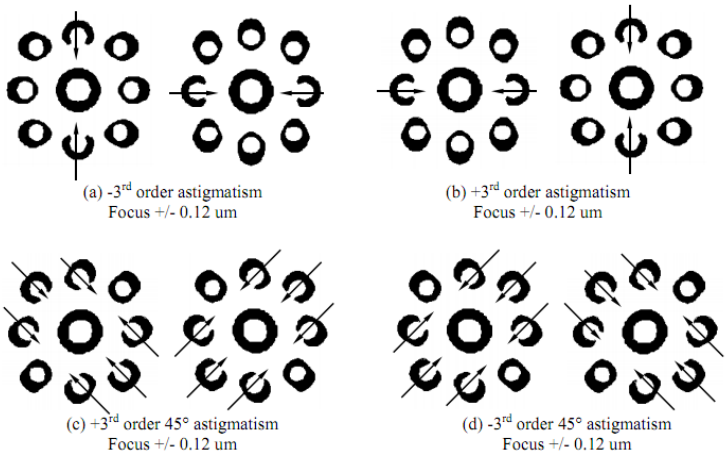

Figure 34: Images of phase wheels in defocus with the presence of a) negative and b) positive 3rd order astigmatism, c) positive and d) negative 3rd order 45° astigmatism. Target dimensions of L1=100 nm, L2=150 nm, and L3=200 nm imaged at 157 nm wavelength, 0.85NA, 0.30σ in resist [68].

When considering spherical aberration the phase wheel prints in a distinct pattern through focus as seen in Figure 35, with -0.16, -0.12, +0.12, and +0.16 microns defocus. Imaging of the phase wheels in the presence of spherical aberration causes the rings to expand and contract through focus, eventually merging with extreme defocus. Like with the astigmatism case, the effects are symmetric through focus, showing the symmetric nature of the even aberration.

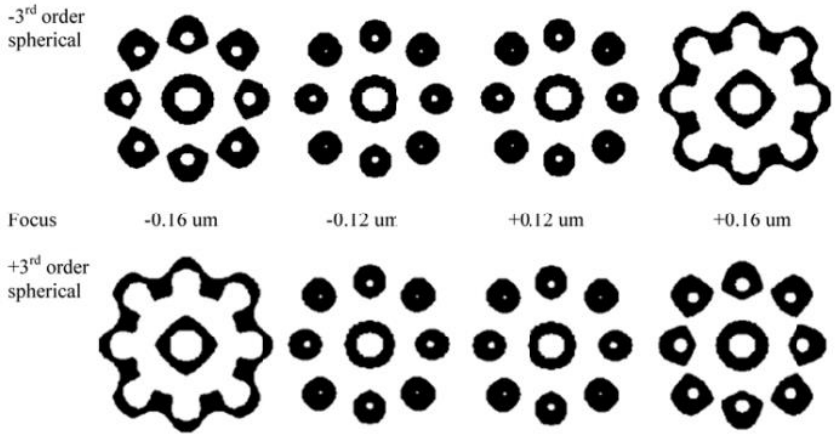

Figure 35: Images of phase wheels through defocus with the presence of negative (top) and positive (bottom) 3rd order spherical. Target dimensions of L1=100 nm, L2=150 nm, and L3=200 nm imaged at 157 nm wavelength, 0.85NA, 0.30σ in resist [68].

Odd aberrations (n,m is odd) such as coma and trefoil are asymmetric in the pupil in the xy plane. Figure 36 (a) shows the unique effect of imaging the phase wheel in the presence of positive and negative third order coma x and y (Z_7 & Z_8). The vector lines shown can be used to visualize the effect of an aberration and can be uniquely recognized for a particular aberration under test. Coma being an odd aberration, it has no focus dependence, but will cause the phase wheel to print with open rings on all but three of the external rings as seen in Figure 36 (a), with the opposite rings remaining closed. Trefoil,

like coma is an odd aberration and no focus dependence. The effect of trefoil on the phase wheel target is seen in Figure 36 (b). Unlike the effects of coma, trefoil deforms all rings with the vectors pointing to a single point, showing the 120° symmetry of the aberration.

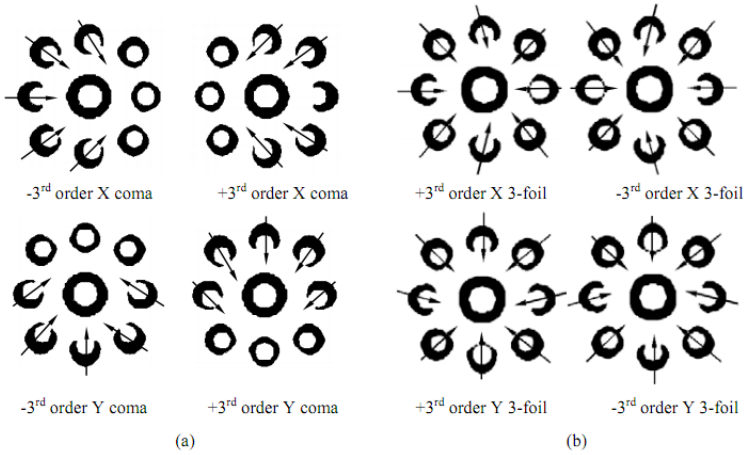

Figure 36: Images of phase wheels with the presence of a) negative and positive 3rd order X (top) and Y (bottom) coma, b) positive and negative 3rd order X (top) and Y (bottom) 3-foil (trefoil). Target dimensions of L1=100 nm, L2=150 nm, and L3=200 nm imaged at 157 nm wavelength, 0.85NA, 0.30σ in resist **[68]**.

4. BINARY TARGET METHODOLOGY & RESULTS

The goal of this project is to develop a method to determine the aberration signature of an EUV lithography tool and monitor this signature. The study limits the parameters of the experiment to currently available EUVL tools. The primary tool used in this investigation is a developmental EUVL system at the Center for Nanoscale Science and Engineering (CNSE) at the University of Albany, NY. The system, the ASML alpha demo tool (ADT) has a numerical aperture (NA) of 0.25 and partial coherence (σ) of 0.5 [135]. A diagram of the ADT is shown in Figure 37. Limiting and fixing the NA and σ, as well as the available targets makes extracting aberrations with a unique solution more challenging because these factors offer more degrees of freedom to the experiment. The relatively large value of partial coherence of the ADT limited fitting to lower aberration orders. With a large σ, there is more pupil averaging, which makes extracting higher frequency aberrations difficult as shown in Section 3.6.

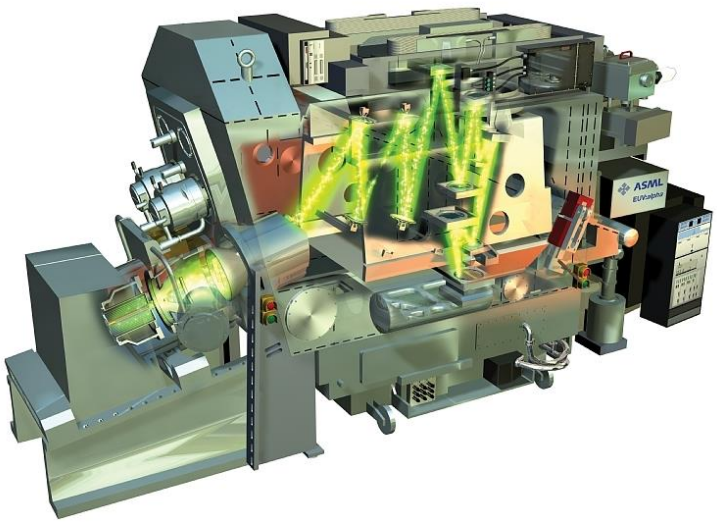

Figure 37: CAD schematic of the ASML ADT showing the EUV beam path [136]

The binary structures that were used include 1:1 lines through pitch of various orientations, five bar, and DRAM isolation structures. Several exposures of features found on existing reticles were completed through dose and focus. Resist CD measurements were then taken with a Hitachi CD4000 scanning electron microscope (SEM). This CD data was then added as input into custom fitting routines, optimized with a software program that interfaces with a commercial lithography simulator (PROLITH^{TM} v14.0.3.1) using a full vector model and threshold resist model. The fitting routines, which are described below, uses predictive models fitted to simulated scenarios of a wide range of aberrated wavefronts. Using these models and the resist CD data, a wavefront can be fit and a particular set of Zernike coefficients used to describe the wavefront. Because the system under test has a rather large fixed partial coherence of

0.5, the targets were only able to probe for and fit low order aberrations as discussed in Section 3.6, with higher order aberrations averaged into the extracted aberration value. The aberrations that were extracted include third order astigmatism (Z_5 & Z_6), coma (Z_7 & Z_8), spherical (Z_9), and fifth order trefoil (Z_{10} & Z_{11}). The simulator was interfaced using MATLAB^{TM} and automated, running approximately ~20,000 simulations for a typical fitting set. This method offers the advantage that it is easily altered and can be adapted to a variety of conditions, parameters, and test targets by altering the setup. This makes the ability to change exposure conditions, resist models, accounting for mask 3D effects, or other non idealities in the model fitting, creating a more accurate extraction of Zernike coefficients.

The extraction algorithm is flexible allowing for the inclusion of different illumination conditions (such as coherent, annular, dipole, etc), the inclusion of mask 3D effects, the use of custom resist models (resist models that have been characterized independently of this exercise), and other parameters by modifying the vector simulator setup as necessary.

4.1 **Binary Target Selection**

Target structures for the ADT, which is a full field EUV lithographic system with a NA of 0.25 and σ of 0.5, were chosen based on the diffraction interaction in the pupil. The diffraction spectrum of a structure must interact with the area of the pupil that the desired aberration effects as shown by the arrows in Figure 38, which shows 3rd order astigmatism and 5th order trefoil x and arrows pointing to areas with the highest lobes or

the highest phase differences. Initially several targets were considered but were narrowed by examining the diffraction spectrum for each test target and verified by lithographic simulation and the structures that showed the highest sensitivity to a given aberration were selected. A full factorial design of experiments (DOE) was then performed on the selected structures with inputs of $Z_4 - Z_{11}$, focus and dose to see if any cross effects were present. An analysis of variance (ANOVA) was then preformed on the results of the DOE and an F-test was performed to determine parameter significance. The parameters of the DOE are shown in Table 3 for horizontal and vertical lines, five bar, and brick wall targets.

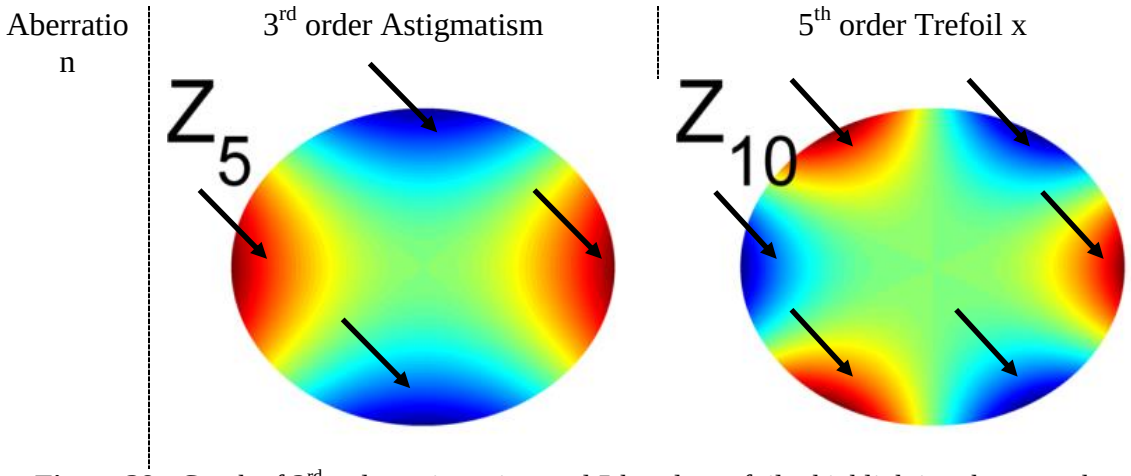

Figure 38: Graph of 3rd order astigmatism and 5th order trefoil x highlighting the areas that diffraction energy must interact with

Table 3: Full factorial DOE design space used to determine significance of Zernike coefficients

Structure	Z_4-Z_{11} Range	Z_4-Z_{11} Step	Focus Range	Focus Step	Measured Response
Horizontal-Vertical Line	±80 mλ	80 mλ	±80 nm	20 nm	HCD-VCD
Five Bar	±80 mλ	80 mλ	±80 nm	20 nm	1st BarCD-5th BarCD
Brick Wall	±50 mλ	50 mλ	±80 nm	20 nm	Bar End CD Difference

4.1.1 *Horizontal and Vertical Lines*

The target investigated for astigmatism was dense lines with a duty cycle of 1:1 at various pitches. The diffraction patterns for dense lines in vertical and horizontal orientations, imaged with an NA of 0.25 and wavelength of 13.5 nm, overlaid with the phase error from astigmatism x is shown in Figure 39. Figure 39 (a) and (b) show the diffraction pattern for pitch 70 nm in vertical and horizontal orientations respectively. Figure 39 (c) and (d) show the diffraction pattern for pitch 90 nm in vertical and horizontal orientations respectively. Figure 39 (e) and (f) show the diffraction pattern for pitch 110 nm in vertical and horizontal orientations respectively. Pitch 90 nm was chosen to avoid non-linear shadowing effects from the reticle, which become an issue for smaller pitches [52] and pitch 90 nm also has sufficient sensitivity to astigmatism, with an expected CD response of 4 nm as can be seen in Figure 41, which is a surface response plot of the delta CD between pitch 90 nm horizontal and vertical lines through focus and astigmatism x (Z_5). Even aberrations such as coma and trefoil are not sensitive to changes in focus. Therefore a through focus method for extracting astigmatism offers greater sensitivity in the presence of odd aberrations than a method not leveraging focus.

Because astigmatism and 45º are identical but rotated in the pupil, the results from astigmatism x-y were applied to astigmatism 45º (Z_6) with structures rotated accordingly.

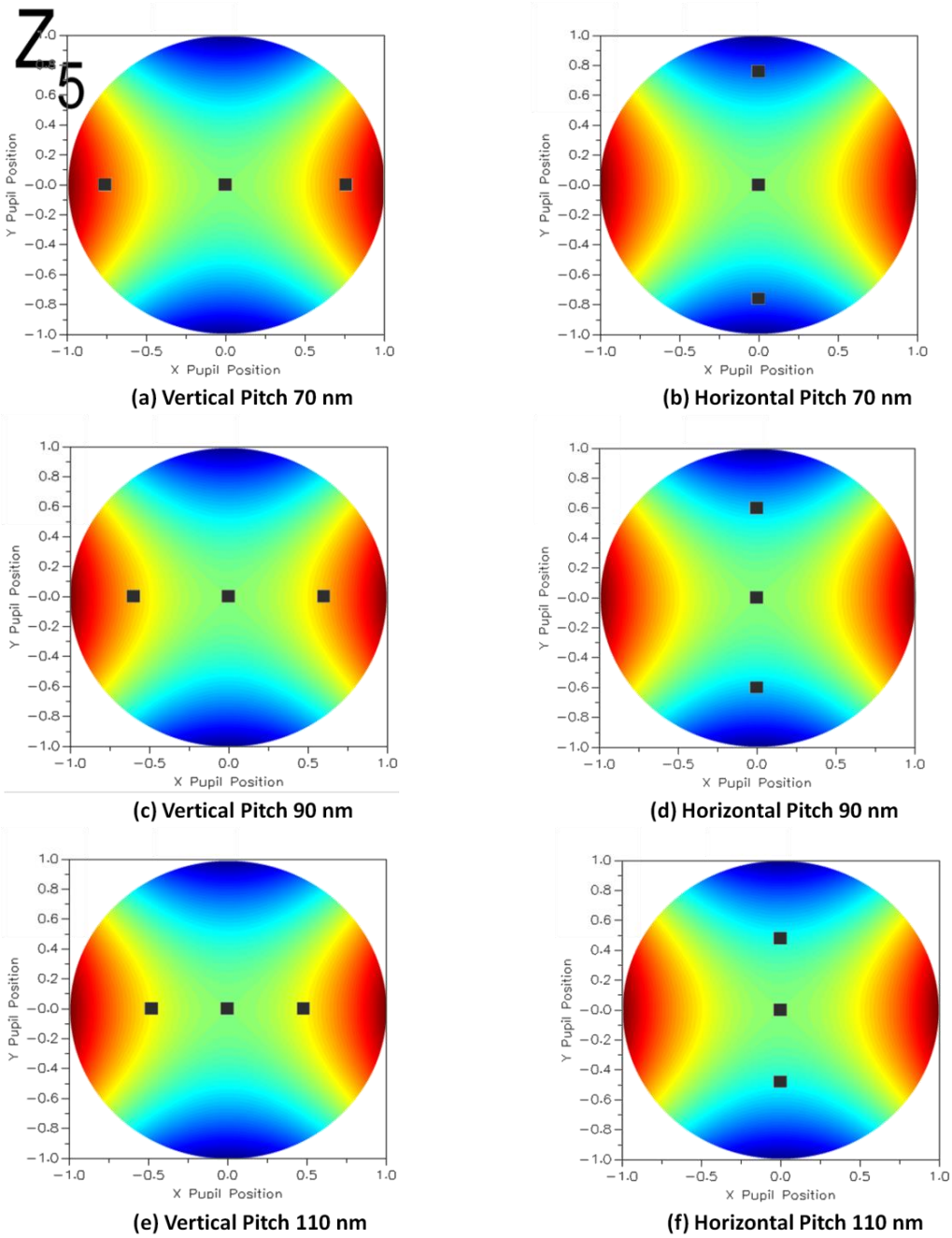

Figure 39: Diffraction spectrum of horizontal and vertical dense line with a duty ratio of 1:1 and a pitch of (a) (b) 70 nm, (c) (d) 90 nm, (e) (f) 110 nm overlaid with x-y astigmatism (Z_5)

The results of the model fit are shown along with the ANOVA results, in Table 4. The model prediction delta CD for horizontal and vertical lines through focus versus actual delta CD with ±80 mλ of Z_4-Z_{11} and ±80 nm of focus is shown in Figure 40. The results of the F-test in the ANOVA show that several terms are significant, including focus*astigmatism x (Z_5), coma y (Z_8), coma x (Z_7), trefoil y (Z_{11})*trefoil y (Z_{11}), trefoil x (Z_{10})* trefoil x (Z_{10}), trefoil x (Z_{10}), trefoil y (Z_{11}). Astigmatism x (Z_5), however is the only term that is significant with focus, because the other terms are odd aberrations. It is also important to note that the effect of the odd aberrations on delta CD of horizontal and vertical lines is small, shown by the small sum of squares, which is the sum of the square of the difference between the data points and the mean of the data points. A large sum of squares means a higher response that can be attributed to a certain model term (in our case focus*astigmatism x). All the odd aberrations have a sum of squares less than 50, while the term focus*astigmatism x has a sum of squares of over 100,000.

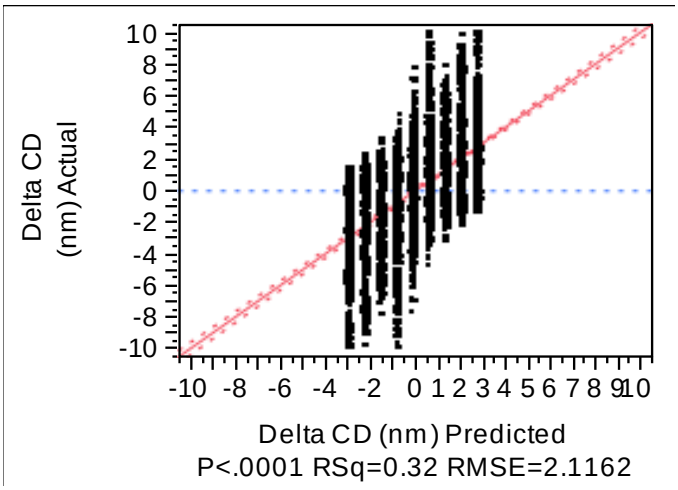

Figure 40: Plot of actual delta CD versus predicted with ±80 mλ of Z_4-Z_{11} and ±80 nm of focus

Table 4: Results of pitch 90 nm, horizontal and vertical lines DOE showing an ANOVA test of significant for Z_4-Z_{11}

Summary of Fit

RSquare	0.315232
RSquare Adj	0.314895
Root Mean Square Error	2.116201
Mean of Response	-0.00159
Observations (or Sum Wgts)	52891

Analysis of Variance

Source	DF	Sum of Squares	Mean Square	F Ratio
Model	26	108983.39	4191.67	935.9944
Error	52864	236741.13	4.48	**Prob > F**
C. Total	52890	345724.52		<.0001*

Effect Tests

Source	Sum of Squares	F Ratio	Prob > F
Focus*Zernike: Astigmatism x (Z_5)	108696.41	24271.77	<.0001*
Zernike: Coma y (Z_8)	46.96	10.4854	0.0012*
Zernike: Coma x (Z_7)	45.68	10.2005	0.0014*
Zernike: Trefoil y (Z_{11})*Zernike: Trefoil y (Z_{11})	39.68	8.8598	0.0029*
Zernike: Trefoil x (Z_{10})*Zernike: Trefoil x (Z_{10})	33.01	7.3704	0.0066*
Zernike: Trefoil x (Z_{10})	24.07	5.3754	0.0204*
Zernike: Trefoil y (Z_{11})	23.64	5.2783	0.0216*
Zernike: Coma x (Z_7)*Zernike: Coma x (Z_7)	1.38	0.3072	0.5794
Zernike: Coma y (Z_8)*Zernike: Coma y (Z_8)	0.58	0.1295	0.7190
Focus*Zernike: Primary Spherical (Z_9)	0.24	0.0526	0.8185
Focus*Zernike: Power (Z_4)	0.13	0.0284	0.8662
Zernike: Power (Z_4)*Zernike: Power (Z_4)	0.10	0.0225	0.8808
Zernike: Astigmatism x (Z_5)*Zernike: Astigmatism x (Z_5)	0.08157668	0.0182	0.8926
Zernike: Primary Spherical (Z_9)*Zernike: Primary Spherical (Z_9)	0.05792164	0.0129	0.9095
Focus*Focus	0.01776503	0.0040	0.9498
Zernike: Astigmatism y (Z_6)*Zernike: Astigmatism y (Z_6)	0.00474164	0.0011	0.9740
Focus*Zernike: Astigmatism y (Z_6)	0.00065601	0.0001	0.9903
Focus*Zernike: Trefoil y (Z_{11})	2.16583e-7	0.0000	0.9998
Focus*Zernike: Coma x (Z_7)	1.39043e-7	0.0000	0.9999
Focus*Zernike: Trefoil x (Z_{10})	3.68809e-9	0.0000	1.0000
Focus*Zernike: Coma y (Z_8)	1.85988e-9	0.0000	1.0000
Zernike: Astigmatism x (Z_5)	1.77983e-9	0.0000	1.0000
Focus	7.6425e-10	0.0000	1.0000
Zernike: Astigmatism y (Z_6)	1.8474e-10	0.0000	1.0000
Zernike: Primary Spherical (Z_9)	1.8708e-11	0.0000	1.0000
Zernike: Power (Z_4)	1.1896e-11	0.0000	1.0000

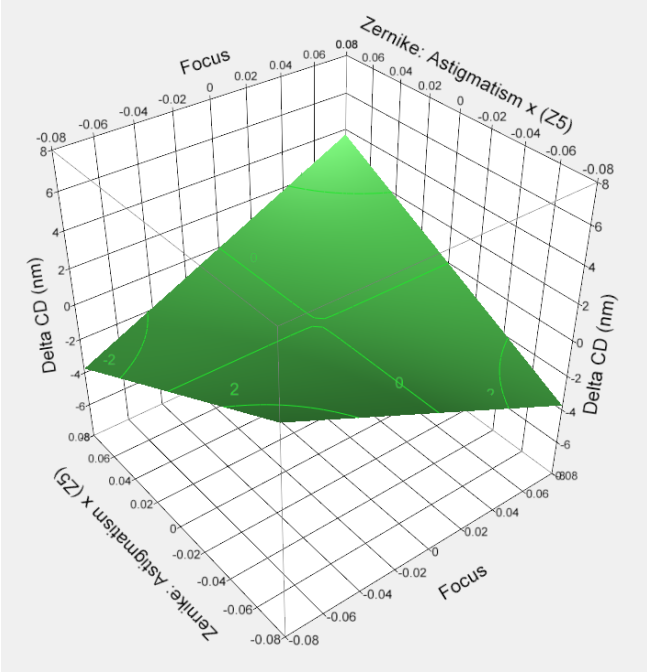

Figure 41: Surface response plot of the delta CD of pitch 90 nm lines through focus and astigmatism (Z_5)

The interactions of astigmatism (Z_5) and higher order astigmatism (Z_{12} and Z_{21}) crossed with power (Z_4), spherical (Z_9) and focus were also investigated. The results of a designed experiment (DOE) and an ANOVA test are presented in Table 5. The interaction between astigmatism (Z_5) and primary spherical (Z_9) was found to be significant, along with higher order astigmatism (Z_{12}, and Z_{21}) crossed with focus, power (Z_4) and spherical (Z_9). The cross terms with power (Z_4) behave similarly as the focus cross terms, which is expected because power is Gaussian focus. Figure 42 shows a plot of the model created with Z_4, Z_5, Z_9, Z_{12}, and Z_{21} versus actual delta CD data of horizontal and vertical 90 nm pitch lines. Astigmatism (Z_5, Z_{12}, and Z_{21}) along with power (Z_4) and spherical (Z_9) were varied ±80 mλ through ±80 nm defocus. The surface response of astigmatism (Z5) through spherical (Z9) is shown in Figure 43. The response of delta CD of horizontal and vertical lines through spherical is much less than that seen

by through focus shown in Figure 41. Because spherical aberration is being solved in an independent manner it is assumed that this interaction will be accounted for.

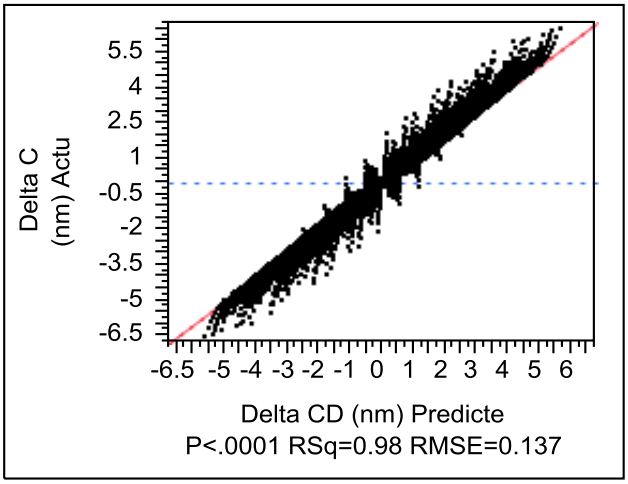

Figure 42: Plot of actual delta CD versus predicted for primary astigmatism and ±80 mλ of higher orders (Z_5,Z_{12},Z_{21}) crossed with power (Z_4), primary spherical (Z_9), and ±80 nm of focus

Table 5: Results of horizontal and vertical line DOE showing an ANOVA test of significant for Z_4, Z_5,Z_9,Z_{12}, and Z_{21}

Summary of Fit

RSquare	0.983828
RSquare Adj	0.983827
Root Mean Square Error	0.137519
Mean of Response	8.744e-8
Observations (or Sum Wgts)	203559

Analysis of Variance

Source	DF	Sum of Squares	Mean Square	F Ratio
Model	15	234170.71	15611.4	825492.6
Error	203543	3849.32	0.018912	**Prob > F**
C. Total	203558	238020.03		<.0001*

Effect Tests

Source	Sum of Squares	F Ratio	Prob > F
Zernike: Astigmatism x (Z_5)*Focus	114244.19	6040961	<.0001*
Zernike: Astigmatism x (Z_5)*Zernike: Power (Z_4)	38468.43	2034119	<.0001*
Zernike: Astigmatism x (Z_5)*Zernike: Primary Spherical (Z_9)	1652.11	87359.78	<.0001*
Zernike: Secondary Astigmatism x (Z_{12})*Focus	22554.03	1192603	<.0001*
Zernike: Secondary Astigmatism x (Z_{12})*Zernike: Power (Z_4)	6097.80	322437.4	<.0001*
Zernike: Secondary Astigmatism x (Z_{12})*Zernike: Primary Spherical (Z_9)	113.87	6021.114	<.0001*
Zernike: Tertiary Astigmatism x (Z_{21})*Focus	37687.56	1992828	<.0001*
Zernike: Tertiary Astigmatism x (Z_{21})*Zernike: Power (Z_4)	11828.67	625471.7	<.0001*
Zernike: Tertiary Astigmatism x (Z_{21})*Zernike: Primary Spherical (Z_9)	1920.30	101541.1	<.0001*
Focus	3.8017e-10	0.0000	0.9999
Zernike: Secondary Astigmatism x (Z_{12})	3.6087e-10	0.0000	0.9999
Zernike: Astigmatism x (Z_5)	2.5749e-10	0.0000	0.9999
Zernike: Tertiary Astigmatism x (Z_{21})	7.0875e-11	0.0000	1.0000

Source	Sum of Squares	F Ratio	Prob > F
Zernike: Power (Z_4)	1.698e-11	0.0000	1.0000
Zernike: Primary Spherical (Z_9)	1.1259e-12	0.0000	1.0000

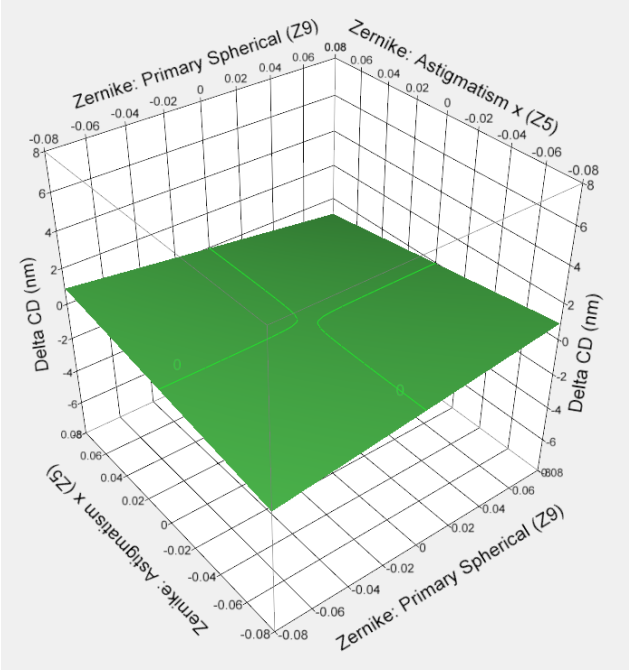

Figure 43: Surface response plot of the delta CD of pitch 90 nm lines through spherical (Z_9) and astigmatism (Z_5)

Higher order astigmatism (Z_{12} and Z_{21}) crossed with power (Z_4), focus or spherical (Z_9) was also found to be a significant factor as seen in Table 5. It is also important to note that the response from higher order astigmatism is less than that of primary astigmatism as seen in Figure 44 and 45, which are the surface response of Z_{12} through focus and Z_{21} through focus respectively. It is assumed because the NA of the system under test is relatively small; the contribution from higher order astigmatism may be small. Any higher order astigmatism in the system will therefore be attributed to primary astigmatism, and an effective astigmatism reported. For a system that has a

smaller partial coherence (0.1 – 0.3) this interaction will be greater and higher orders of astigmatism can be extracted using several different targets or illumination conditions.

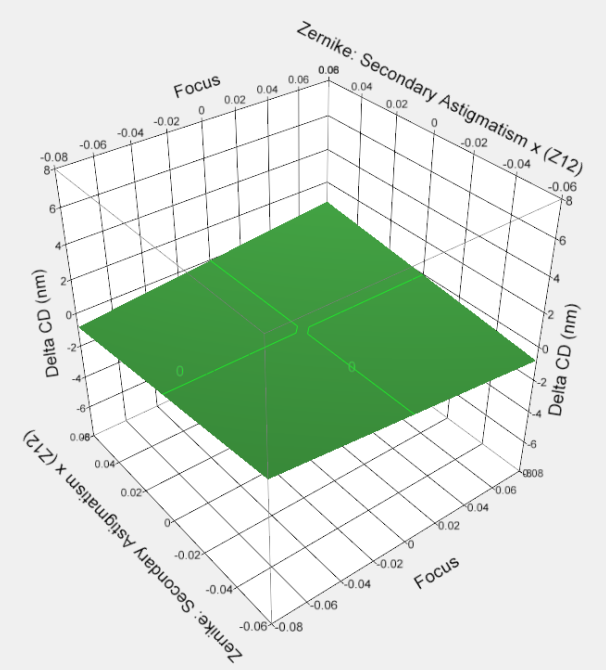

Figure 44: Surface response plot of the delta CD of pitch 90 nm lines through focus and secondary astigmatism (Z_{12})

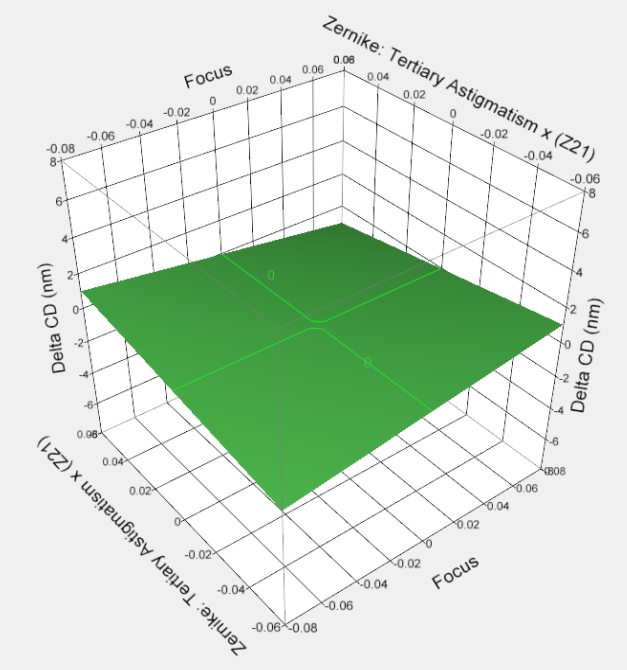

Figure 45: Surface response plot of the delta CD of pitch 90 nm lines through focus and tertiary astigmatism (Z_{21})

4.1.2 *Five Bar Structure*

Odd aberrations like coma and trefoil break rotational symmetry (m=odd#). For coma (Z_5), this makes the aberrated aerial image asymmetric along the x axis. Consequently, structures that have symmetries along the x-axis imaged in the presence of coma will have left-right asymmetries. Figure 46 shows a top-down aerial image simulation of a pitch 64 nm five bar structure, Figure 46 (a) is the simulation with no aberrations, Figure 46 (b) is a simulation of the same structure with 200 mλ of coma (Z_7). Comparing the two aerial images, a clear left-right asymmetry is seen in the aberrated image. The CD difference between the 1st and 5th bar is linear through coma, and relatively constant through focus.

The targets that were investigated for coma include three and five bar structures at various pitches. A five bar structure at pitch 64 nm with 1:1 duty cycle was chosen because it offers the highest sensitivity compared to larger pitches and seven bar targets. The test features are also in the same direction, unlike the target for extracting astigmatism, making effects from shadowing uniform for both the 1st and 5th bars. Three bar structures offered similar sensitivities to five bar structures, but it was believed that a five bar target would be simpler to create a metrology recipe on a CD SEM. The results of the DOE and ANOVA test of significance are shown in Table 6 and the predictive model versus the delta CD data is shown in Figure 47, in the presence of ±80 mλ of aberrations Z_4-Z_{11} and ±80 nm focus. The terms that were found to be significant include coma (Z_5) and trefoil (Z_{10}). The response of trefoil was found to have a sum of squares an order of magnitude lower than the response of coma, which were approximately

80,000 and 800,000 respectively. This indicates a stronger response from coma compared to trefoil, as seen in the surface profiles shown in Figure 48, which is the response of delta CD of the 1st and 5th bar of a five bar target with a duty ratio of 1:1 and a pitch of 64 nm. The same results were applied to coma y with structures rotated 90°.

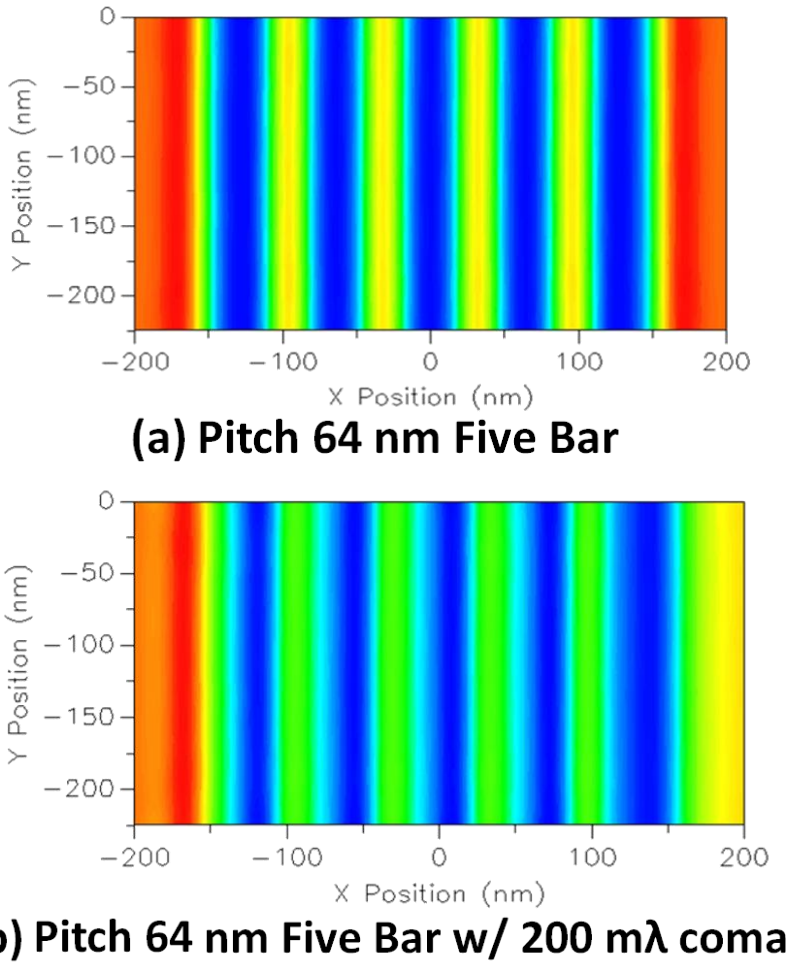

Figure 46: Aerial image of a 64 nm pitch five bar target with a duty ratio of 1:1 and (a) no aberrations, and (b) 200 mλ of coma (Z_7)

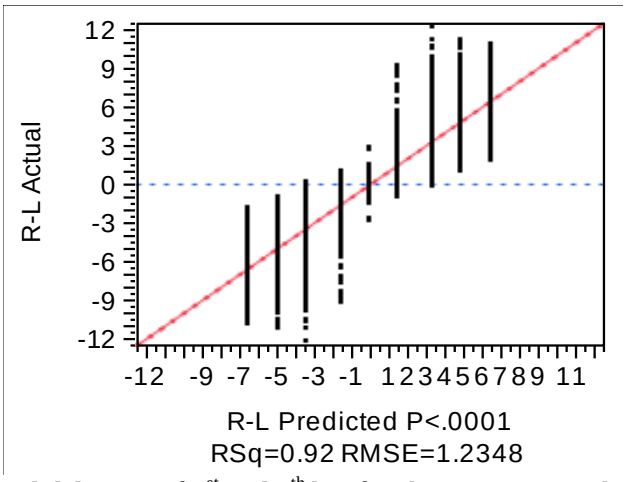

Figure 47: Plot of actual delta CD of 1st and 5th bar five bar structure with ±80 mλ of aberrations Z_4-Z_{11} and ±80 nm focus

Table 6: Results of five bar DOE showing an ANOVA test of significant for Z_4-Z_{11}

Summary of Fit

RSquare	0.920215
RSquare Adj	0.920177
Root Mean Square Error	1.234759
Mean of Response	-7.82e-6
Observations (or Sum Wgts)	53713

Analysis of Variance

Source	DF	Sum of Squares	Mean Square	F Ratio
Model	26	944052.2	36309.7	23815.41
Error	53686	81851.3	1.5	**Prob > F**
C. Total	53712	1025903.5		<.0001*

Effect Tests

Source	Sum of Squares	F Ratio	Prob > F
Zernike: Coma x (Z_7)	859790.84	563933.9	<.0001*
Zernike: Trefoil x (Z_{10})	85833.60	56297.97	<.0001*
Focus (um)*Zernike: Astigmatism y (Z_6)	0.47	0.3095	0.5780
Zernike: Coma x (Z_7)*Zernike: Coma x (Z_7)	2.68614e-7	0.0000	0.9997
Focus (um)*Zernike: Power (Z_4)	1.34792e-7	0.0000	0.9998
Zernike: Power (Z4)*Zernike: Power (Z_4)	4.25408e-8	0.0000	0.9999
Focus (um)*Zernike: Primary Spherical (Z_9)	2.073e-8	0.0000	0.9999
Zernike: Trefoil y (Z_{11})	1.0027e-8	0.0000	0.9999
Focus (um)*Focus (um)	7.57223e-9	0.0000	0.9999
Focus (um)*Zernike: Trefoil x (Z_{10})	5.80633e-9	0.0000	1.0000
Zernike: Astigmatism y (Z_6)*Zernike: Astigmatism y (Z_6)	5.43284e-9	0.0000	1.0000
Zernike: Coma y (Z_8)	3.14683e-9	0.0000	1.0000
Focus (um)*Zernike: Coma x (Z_7)	2.70829e-9	0.0000	1.0000
Zernike: Power (Z_4)	2.6512e-9	0.0000	1.0000
Zernike: Coma y (Z_8)*Zernike: Coma y (Z_8)	2.56701e-9	0.0000	1.0000
Zernike: Primary Spherical (Z_9)	2.2894e-9	0.0000	1.0000
Focus (um)*Zernike: Coma y (Z_8)	1.61754e-9	0.0000	1.0000
Zernike: Astigmatism x (Z_5)	1.41422e-9	0.0000	1.0000
Zernike: Trefoil y (Z_{11})*Zernike: Trefoil y (Z_{11})	1.11027e-9	0.0000	1.0000
Focus (um)*Zernike: Trefoil y (Z_{11})	6.1797e-10	0.0000	1.0000

Source	Sum of Squares	F Ratio	Prob > F
Focus (um)*Zernike: Astigmatism x (Z_5)	4.4915e-10	0.0000	1.0000
Zernike: Trefoil x (Z_{10})*Zernike: Trefoil x (Z_{10})	3.3931e-10	0.0000	1.0000
Zernike: Primary Spherical (Z_9)*Zernike: Primary Spherical (Z_9)	2.768e-10	0.0000	1.0000
Focus (um)	1.9329e-10	0.0000	1.0000
Zernike: Astigmatism y (Z_6)	1.7455e-10	0.0000	1.0000
Zernike: Astigmatism x (Z_5)*Zernike: Astigmatism x (Z_5)	1.4498e-11	0.0000	1.0000

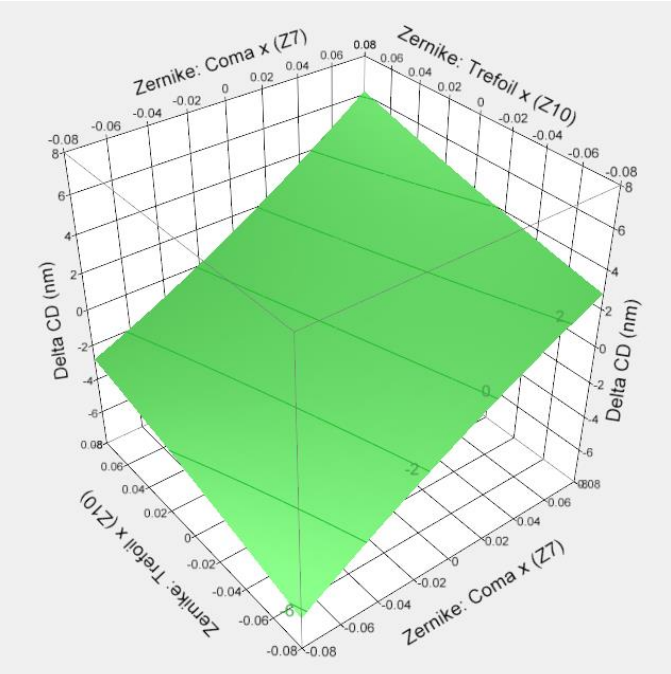

Figure 48: Surface response plot of left right CD difference in a pitch 64 nm five bar structure through coma (Z_7) and trefoil (Z_{10})

The effect of higher order coma was also investigated. Table 7 shows the results of a DOE and ANOVA test for significance for the delta CD between the 1st and 5th bar of a 64 nm pitch five bar structure with inputs of coma (Z_7), secondary coma (Z_{14}), tertiary coma (Z_{23}), trefoil (Z_{10}), and focus. Higher order coma was also found to be significant. The plot of the model predicted delta CD between the 1st and 5th bar of a 64 nm pitch five bar structure versus the actual delta CD is shown in Figure 49, with ±80 mλ of Z_7, Z_{10}, Z_{14}, and Z_{23}, as well as ±80 nm defocus. It is important to note that the

sum of squares from coma was about 11,000 while the sum of squares for secondary and tertiary coma was about 3,000 and 400 respectively, indicating a smaller response than that of primary coma. This can be seen by comparing the surface response of higher order coma, seen in Figure 50, with that of primary coma seen in Figure 48. It is assumed, as stated previously, that because the system under test has a relatively low NA, the aberration signature will be mostly primary aberrations. Any higher order aberrations present will contribute to the effective primary coma aberration that is extracted from five bar targets. Similarly as astigmatism, a system with a lower partial coherence (0.1 – 0.3) will have a greater sensitivity to higher order coma and by coupling the extraction with various targets and/ or illuminators a unique solution for higher order coma can be determined.

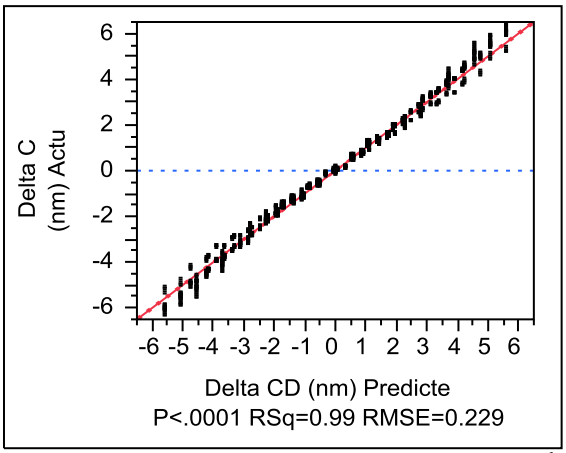

Figure 49: Plot of predicted versus actual CD delta of the 1st and 5th bar with primary and ±80 mλ of higher order coma (Z_{14}, Z_{23}), trefoil (Z_{10}), and ±80 nm focus

Table 7: Results of five bar DOE showing an ANOVA test of significant for coma (Z_7), higher order coma (Z_{14} and Z_{23}), along with trefoil (Z_{10}) and focus

Summary of Fit

RSquare	0.992868
RSquare Adj	0.992812
Root Mean Square Error	0.229243
Mean of Response	9.694e-6

Summary of Fit

Observations (or Sum Wgts)	2187

Analysis of Variance

Source	DF	Sum of Squares	Mean Square	F Ratio
Model	17	15867.975	933.410	17761.51
Error	2169	113.986	0.053	**Prob > F**
C. Total	2186	15981.961		<.0001*

Effect Tests

Source	Sum of Squares	F Ratio	Prob > F
Zernike: Coma x (Z_7)	11450.107	217879.8	<.0001*
Zernike: Secondary Coma x (Z_{14})	2985.334	56806.79	<.0001*
Zernike: Tertiary Coma x (Z_{23})	384.045	7307.840	<.0001*
Zernike: Trefoil x (Z_{10})	1048.412	19949.84	<.0001*
Zernike: Secondary Trefoil x (Z_{19})	0.078	1.4820	0.2236
Zernike: Trefoil x (Z_{10})*Zernike: Trefoil x (Z_{10})	6.91587e-9	0.0000	0.9997
Focus (um)*Zernike: Coma x (Z_7)	1.48148e-9	0.0000	0.9999
Zernike: Coma x (Z_7)*Zernike: Coma x (Z_7)	1.20942e-9	0.0000	0.9999
Zernike: Secondary Coma x (Z_{14})*Zernike: Secondary Coma x (Z_{14})	8.2533e-10	0.0000	0.9999
Focus (um)	4.3896e-10	0.0000	0.9999
Focus (um)*Zernike: Trefoil x (Z_{10})	2.572e-10	0.0000	0.9999
Zernike: Secondary Trefoil x (Z_{19})*Zernike: Secondary Trefoil x (Z_{19})	2.2862e-10	0.0000	0.9999
Zernike: Tertiary Coma x (Z_{23})*Zernike: Tertiary Coma x (Z_{23})	2.2862e-10	0.0000	0.9999
Focus (um)*Zernike: Secondary Trefoil x (Z_{19})	9.2593e-11	0.0000	1.0000
Focus (um)*Zernike: Tertiary Coma x (Z_{23})	4.1152e-11	0.0000	1.0000
Focus (um)*Zernike: Secondary Coma x (Z_{14})	4.1152e-11	0.0000	1.0000
Focus (um)*Focus (um)	3.658e-11	0.0000	1.0000

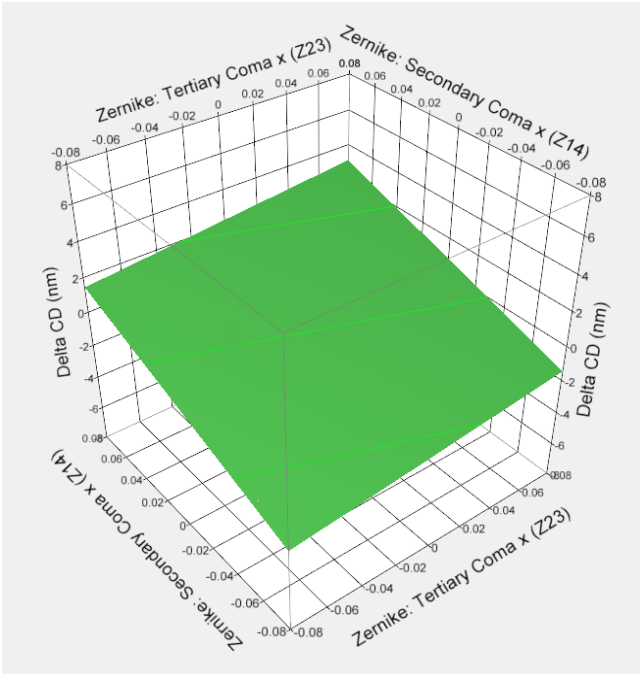

Figure 50: Surface plot of left right CD difference in pitch 64 nm five bar structure through secondary and tertiary coma (Z_{14} & Z_{23})

4.1.3 *Through Pitch Best-Focus Shift*

The test response investigated to determine primary spherical aberration was the change in best focus through pitch. The highest sensitivity was found between pitches 50 nm and 130 nm and more isolated pitches having little change in best focus as can be seen in Figure 51, which shows the change in best focus (delta) response for various spherical aberration levels, ±80 mλ, for pitches between 64 to 256 nm and a line CD of 32 nm. Also shown in Figure 51 is the pitch location where a certain diffraction order is entering the pupil, as indicated by the images of Z_9 overlaid with the diffraction order that is entering the pupil with σ=0.5. The phase error caused by the various diffraction orders entering the pupil through pitch, gives the unique shape of the best focus versus pitch curves in the presence of spherical aberration (Z_9). Figure 52 is a plot of the best focus change normalized by primary spherical aberration (Z_9), showing that the shape of the change in best focus versus pitch curve is independent of primary spherical, Z_9 only changing the scale of the best focus change. Using this method, a robust determination of primary spherical aberration can be determined, and, as stated previously, the value of the extracted Z_9 will also be influenced by higher order spherical terms (Z_{16}, Z_{25}, Z_{36}). The contribution of higher order spherical aberrations, however, is presumed small due to the relatively small NA of the ADT.

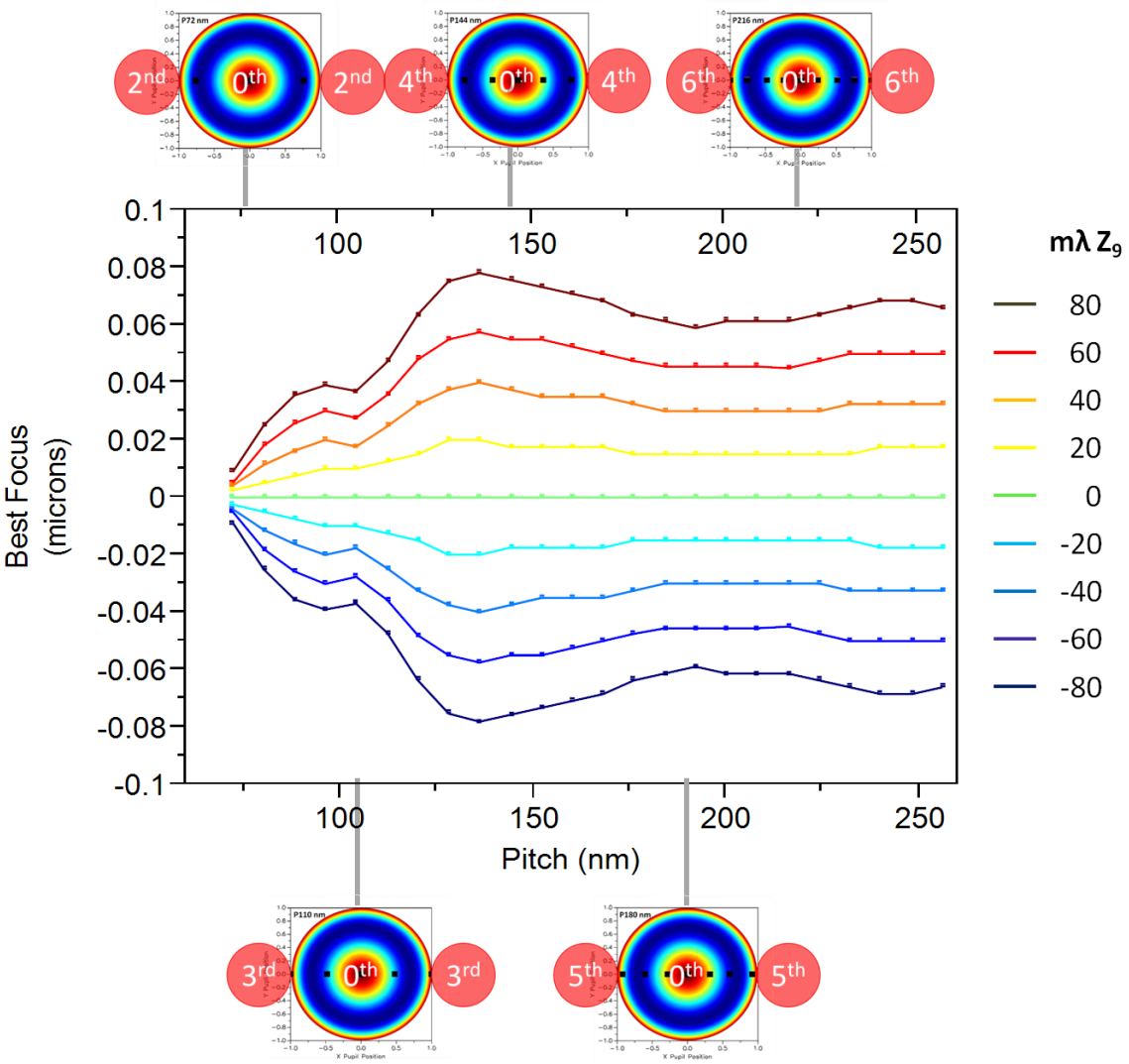

Figure 51: Expected best focus shift through pitch for incrementing Z_9, from -80 mλ (bottom line) to 80 mλ (top line)

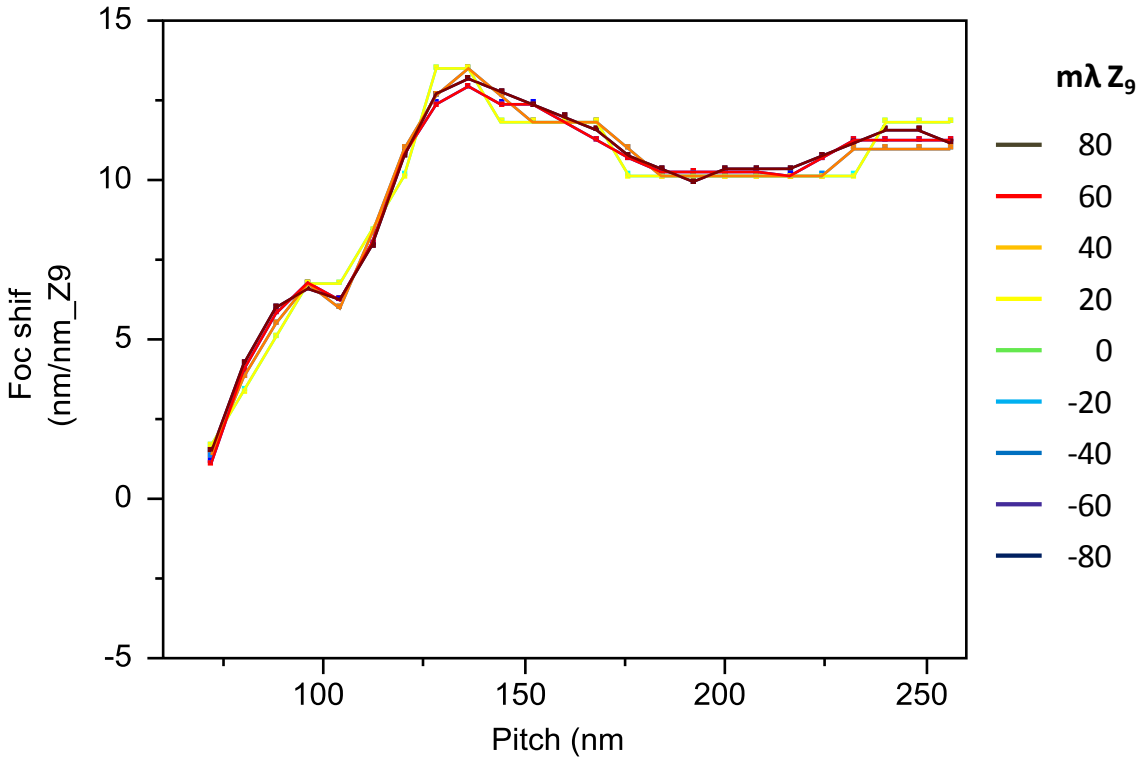

Figure 52: Expected best focus shift through pitch for various spherical aberrations normalized by Z_9

4.1.4 *Brick Wall*

The target investigated for the extraction of trefoil (Z_{10} & Z_{11}) was brick wall pillars with various x or horizontal pitch (HP) and y or vertical pitch (VP) as seen in Figure 53, showing the 120° pitch that enables the sensitivity of brick wall pattern to trefoil (Z_{11}). The vertical pitch was chosen so that the diffraction order interacts with the highest lobe of the trefoil aberration in the y direction as seen in Figure 54 (a). The horizontal pitch can then be simply calculated by the expression HP=arctan(120°-90°)/VP. The diffraction pattern of the brick wall structure for increasing horizontal or x pitch is seen in Figure 54. Figure 54 (a) shows an overlay of the diffraction pattern of a brick wall structure that has a horizontal pitch of 90 nm and a vertical pitch of 240 nm

with the Zernike polynomial trefoil y (Z_{11}). Also shown in Figure 54 (a) are the vertical diffraction orders entering the pupil for the 240 nm pitch. Figure 54 (b) shows an overlay of the diffraction pattern of a brick wall structure that has a horizontal pitch of 110 nm and a vertical pitch of 240 nm with the Zernike polynomial trefoil y (Z_{11}). Figure 54 (c) shows an overlay of the diffraction pattern of a brick wall structure that has a horizontal pitch of 130 nm and a vertical pitch of 240 nm with the Zernike polynomial trefoil y (Z_{11}). Also seen in Figure 54 (c) is the emergence of a diffraction pattern of interest, one that interacts directly with the highest lobe of trefoil at 120° symmetry. Figure 54 (d) shows an overlay of the diffraction pattern of a brick wall structure that has a horizontal pitch of 130 nm and a vertical pitch of 240 nm with the Zernike polynomial trefoil y (Z_{11}). Figure 54 (d) shows the diffraction pattern of interest moving away from the high phase contrast area of trefoil, in imaging this resulted in a decrease in sensitivity to the trefoil aberration. The structure that was found to be most sensitive was a brick wall structure with a horizontal pitch of 128 nm, vertical pitch of 240 nm, vertical CD of 32 nm and horizontal CD of 160 nm. Since trefoil x is the same as trefoil y but with a 90° rotation, the same analysis can be applied, using a target structure rotated by 90°

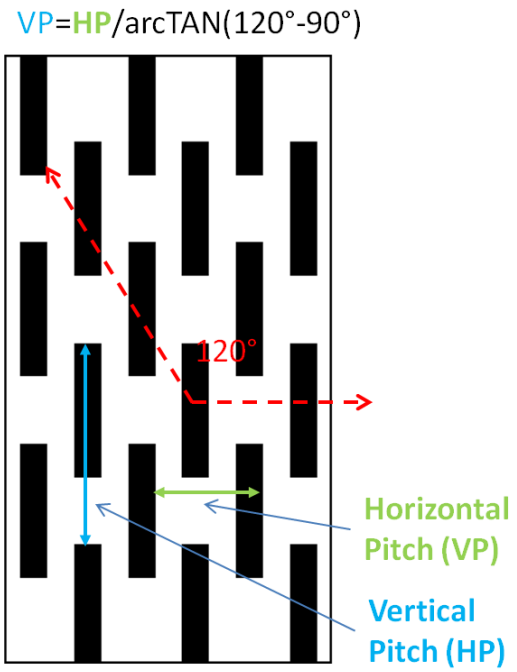

Figure 53: Drawing of a brick wall pattern with a pitch in the 120° orientation

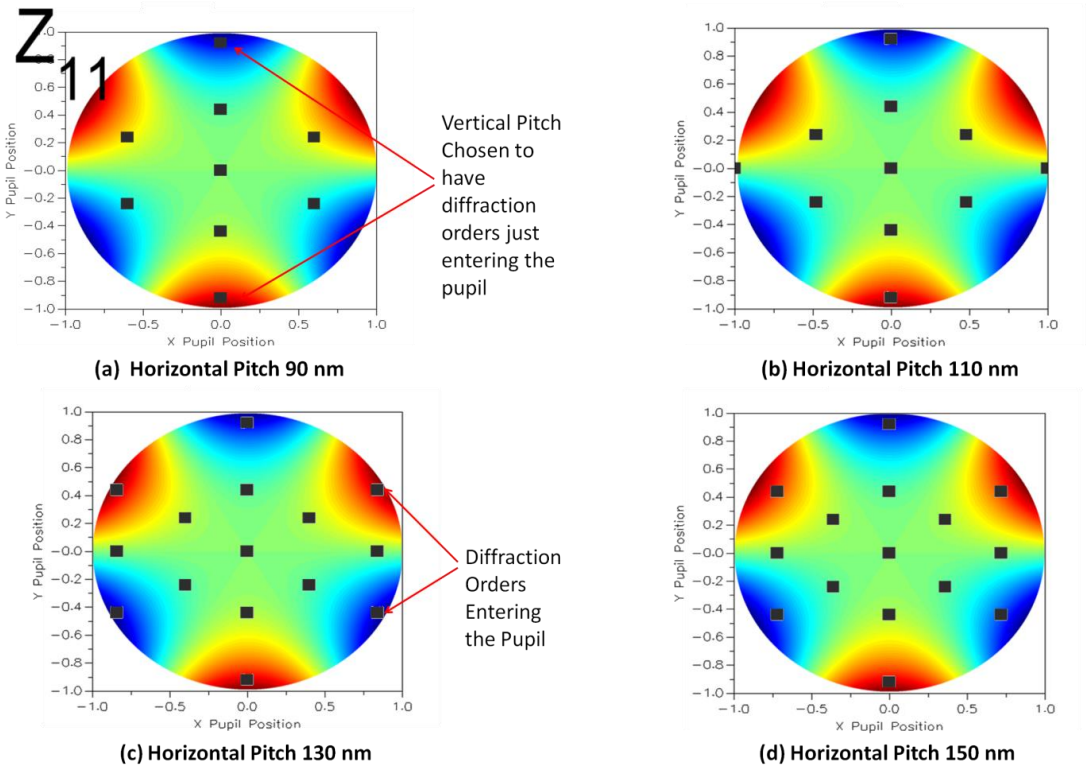

Figure 54: Diffraction spectrum of a brick wall structure with a vertical pitch of 240 nm and horizontal pitch of (a) 90 nm, (b) 110 nm, (c) 130 nm, and (d) 150 nm

A full factorial DOE was performed to determine any interactions with the test target as described in Table 3. The results of the DOE and ANOVA test for significance are shown in Table 8. The terms that were found to be significant were trefoil x (Z_{10}), and coma x (Z_7). The difference between the top and bottom CD of the printed bar, as seen in Figure 55, was used to create a model for trefoil y. Figure 55 (a) shows the ideal image with no aberrations and Figure 55 (b) shows the effect of trefoil y, with the CD of the top of the bar printing smaller than the bottom CD with a positive 200 mλ of trefoil y.

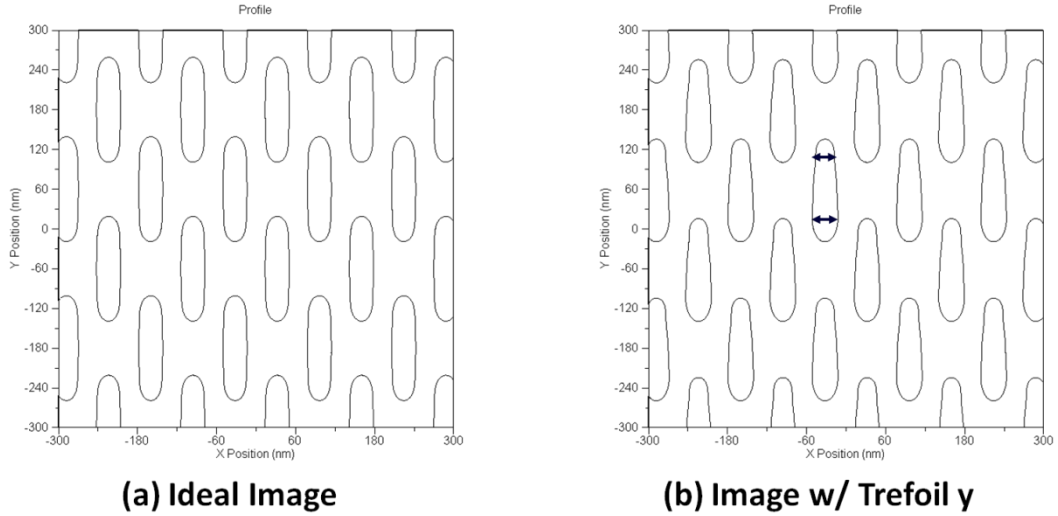

Figure 55: Image of a brick wall structure with a vertical pitch and CD of 240 nm and 160 nm respectively, and horizontal pitch and CD of 128 nm and 32 nm respectively, imaged with (a) no aberrations and (b) with 200 mλ of trefoil y

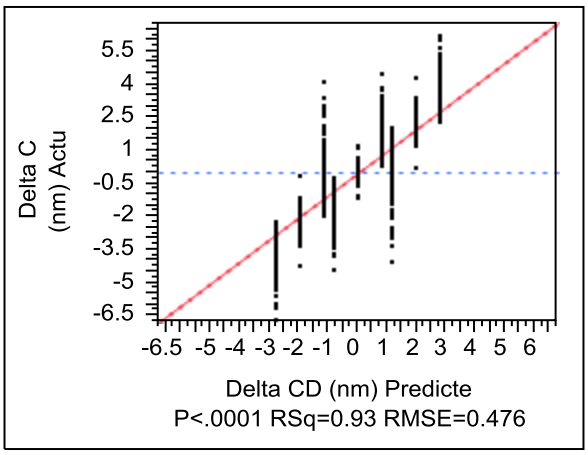

Figure 56: Plot of predicted versus actual CD delta of the bar ends of a brick wall structure with ±80 mλ of aberrations Z_4-Z_{11} and ±80 nm focus

Table 8: Results of brick wall DOE showing an ANOVA test of significant for Z_4-Z_{11}

Summary of Fit

RSquare	0.930198
RSquare Adj	0.930166
Root Mean Square Error	0.476746
Mean of Response	-3.5e-6
Observations (or Sum Wgts)	55837

Analysis of Variance

Source	DF	Sum of Squares	Mean Square	F Ratio
Model	25	169043.41	6761.74	29749.81
Error	55811	12685.10	0.23	**Prob > F**
C. Total	55836	181728.51		<.0001*

Effect Tests

Source	Sum of Squares	F Ratio	Prob > F
Zernike: Coma x (Z_7)	24455.97	107599.6	<.0001*
Zernike: Trefoil x (Z_{10})	144995.87	637942.5	<.0001*
Focus (um)*Zernike: Power (Z_4)	2.02137e-7	0.0000	0.9992
Focus (um)*Zernike: Primary Spherical (Z_9)	1.37009e-8	0.0000	0.9998
Zernike: Coma y (Z_8)	1.21978e-8	0.0000	0.9998
Zernike: Trefoil y (Z_{11})	1.17933e-8	0.0000	0.9998
Zernike: Astigmatism x (Z_5)*Zernike: Astigmatism x (Z_5)	8.22196e-9	0.0000	0.9998
Zernike: Power (Z_4)*Zernike: Power (Z_4)	6.66873e-9	0.0000	0.9999
Zernike: Primary Spherical (Z_9)*Zernike: Primary Spherical (Z_9)	2.38928e-9	0.0000	0.9999
Zernike: Trefoil x (Z_{10})*Zernike: Trefoil x (Z_{10})	1.87553e-9	0.0000	0.9999
Focus (um)	1.6698e-9	0.0000	0.9999
Zernike: Power (Z_4)	1.61404e-9	0.0000	0.9999
Focus (um)*Zernike: Trefoil x (Z_{10})	5.9017e-10	0.0000	1.0000
Focus (um)*Zernike: Astigmatism x (Z_5)	5.2511e-10	0.0000	1.0000
Zernike: Astigmatism x (Z_5)	4.0571e-10	0.0000	1.0000
Zernike: Primary Spherical (Z_9)	2.8419e-10	0.0000	1.0000
Zernike: Coma x (Z7)*Zernike: Coma x (Z_7)	2.8332e-10	0.0000	1.0000
Focus (um)*Zernike: Astigmatism y (Z_6)	2.2171e-10	0.0000	1.0000
Focus (um)*Zernike: Trefoil y (Z_{11})	2.0908e-10	0.0000	1.0000
Focus (um)*Zernike: Coma x (Z_7)	1.9872e-10	0.0000	1.0000
Zernike: Astigmatism y (Z_6)*Zernike: Astigmatism y (Z_6)	8.3942e-11	0.0000	1.0000
Zernike: Astigmatism y (Z_6)	5.2657e-11	0.0000	1.0000
Zernike: Coma y (Z_8)*Zernike: Coma y (Z_8)	2.3907e-11	0.0000	1.0000
Focus (um)*Zernike: Coma y (Z_8)	8.0467e-12	0.0000	1.0000
Zernike: Trefoil y (Z_{11})*Zernike: Trefoil y (Z_{11})	7.088e-12	0.0000	1.0000

It was found that coma y has an interaction with the brick wall pattern used for the extraction of trefoil y, and likewise coma x had an interaction with the brick wall pattern used to extract trefoil x, which shows the expected delta CD response to a certain amount of trefoil and coma. It is important to note that the sensitivity of trefoil is larger than that of coma, as seen by the sum of squares, where the sum of squares for trefoil was about 145,000 and for coma was 25,000. This can also be seen in the surface plot in Figure 58, showing the expected bar end delta CD for coma and trefoil, trefoil having a larger response. Figure 57 shows the overlay of a brick wall pattern with a vertical pitch of 240 nm and horizontal pitch of 130 nm with both phase plots of trefoil y (Figure 57 (a)) and coma y (Figure 57 (b)). The diffraction orders that are circled in both overlays show similar phase deviations that would result in a similar observed imaging difference.

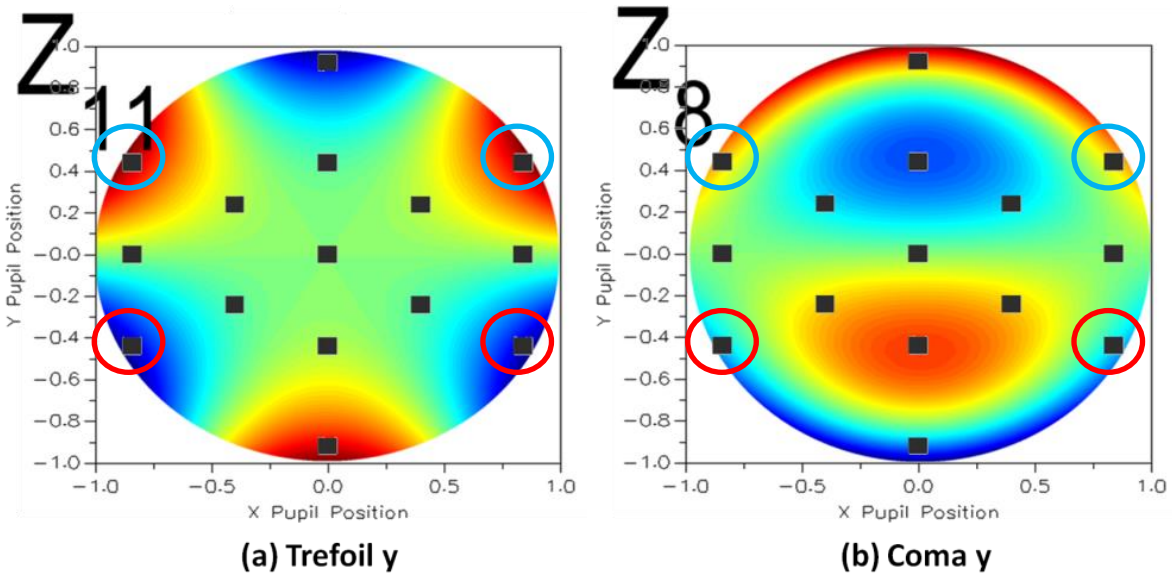

Figure 57: Diffraction spectrum of a brick wall structure with a vertical pitch of 240 nm and horizontal pitch of 130 nm overlaid with (a) trefoil y (Z_{11}) and (b) coma y (Z_8) indicating the diffraction orders that are interacting with similar areas of the two aberrations

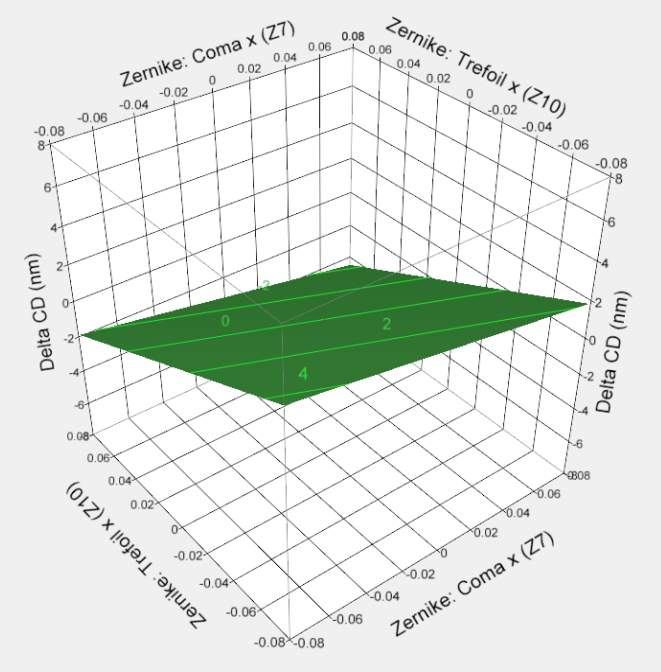

Figure 58: Surface response plot of the left right CD difference of a brick wall pattern through trefoil (Z_{10}) and coma (Z_7)

4.2 **Modeling & Extraction**

The first step in the flow described in Figure 59 as 'Stage 1' is to fit astigmatism, coma, spherical, and trefoil concurrently. A matrix of linear equations as a function of astigmatism and focus were created that use the CD difference of 1:1 lines, with a typical pitch of 90 nm, in vertical and horizontal orientations for astigmatism x and 45° and 135° for astigmatism y. The sensitivity of the models was found to be 0.075nm ΔCD/mλ astigmatism, meaning that for a 30 mλ eRMS lens, which is typical for EUVL, a measured CD difference of 2.25 nm is expected, which is well within the current modern metrology equipment detection limits [137,138]. Using these models, initial values for astigmatism x and y were determined.

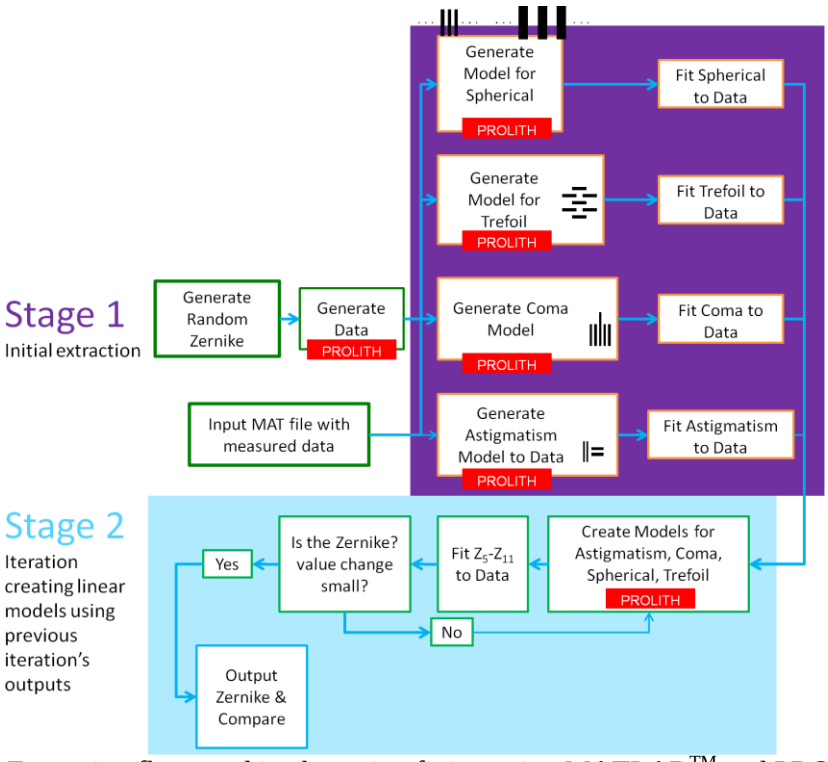

Figure 59: Extraction flow used in aberration fitting using MATLAB™ and PROLITH™

Concurrently, models were fit and used to find the initial value of coma x and y. The models for coma use a five bar structure with a pitch of 64 nm and 1:1 duty ratio in orthogonal orientations. The impact of coma aberration is evaluated by measuring the CD difference between the 1st and 5th bar. The sensitivity of the model was similarly found to be 0.075 nm ΔCD/mλ coma, an expected CD measurement of 2.25 nm for 30 mλ eRMS aberrated lens. The 1^{st} and 5^{th} bar delta CD was also found to be a function of trefoil, with a sensitivity of 0.015 nm ΔCD/mλ trefoil, resulting in a 0.45 nm CD difference from a 30 mλ eRMS aberrated lens.

Primary spherical fitting required more data than coma and astigmatism and is fit by measuring the best focus shift through pitch. This requires a focus exposure matrix (FEM) for each pitch. Using the initial values for astigmatism and coma in the FEM, this method was used to determine an initial value for spherical aberration using a best fit for all pitch values as described by Figure 51.

A linear model for trefoil was created using the bar end CD difference from DRAM isolation pillars with a vertical pitch of 128 nm, horizontal pitch of 240 nm and CD of 160 by 32 nm. The model was fit at best dose for different trefoil values and used to obtain an initial value for trefoil x and y. Trefoil y uses the same brick wall structure as trefoil x but rotated 90º. The sensitivity of the model was found to be 0.070 nm ΔCD/mλ trefoil, resulting in an expected CD difference of 2.1 nm from a 30 mλ eRMS aberrated lens. Table 9 shows a summary of the test structures described as well as the test measurement output.

In stage 2, the solved wavefront from stage 1 was used as a starting point and a new wavefront was solved for as seen Figure 59. Once initial values of primary aberrations were determined, new models were created by simulating the pertinent Zernike coefficient effect on the CD metric or focus shift for aberrations up to Z_{11}. The current iteration uses as input the last iterations extracted Zernike coefficients. This was done until the Zernike coefficients were stable and changed less than five percent for each coefficient. Then the output wavefront was displayed together with the determined coefficient values. An example wavefront is shown in the next section.

Table 9: Binary structures found to be sensitive for the ADT

Aberration	***Binary test Structure***	***Test Output***
Z_5 *astigmatism x*	*Horizontal and vertical lines* CD: 45nm Duty ratio- 1:1	*Horizontal and vertical line CD difference through focus*
Z_6 *astigmatism y*	*45º and 135º lines* CD: 45nm Duty ratio-1:1	*45º and 135º line CD difference through focus*
Z_7 *coma x*	*Vertical five bar structure* CD: 32nm Duty ratio-1:1	*1st and 5th bar CD difference through dose*
Z_8 *coma y*	*Horizontal five bar structure* CD: 32nm Duty ratio-1:1	*1st and 5th bar CD difference through dose*
Z_9 *primary spherical*	*Horizontal lines through pitch* (60nm-260nm) CD:32nm	*Best focus through pitch*
Z_{10} *trefoil x*	*Horizontal brick wall structure* V-pitch: 128nm H-Pitch:240nm V-CD: 32nm H-CD: 160nm	*Left and right bar end CD difference through dose*
Z_{11} *trefoil y*	*Vertical brick wall structure* V-pitch: 240nm H-Pitch:128nm V-CD: 160nm H-CD: 32nm	*Top and bottom bar end CD difference through dose*

4.3 **Preliminary Simulated Results**

Several randomly generated wavefronts, generated from randomly selecting Z_5-Z_{11} from a normal distribution between -30 mλ to 30 mλ, are investigated to test the feasibility of using this approach with realistic aberration levels in EUVL. A representative wavefront is shown in Figure 60. Figure 60a, having a wavefront error RMS of 30 milliwaves (0.4nm), which is typical for EUVL scanners. After processing through the flow shown in Figure 59, using four iterations, the predicted wavefront is shown in Figure 60b.

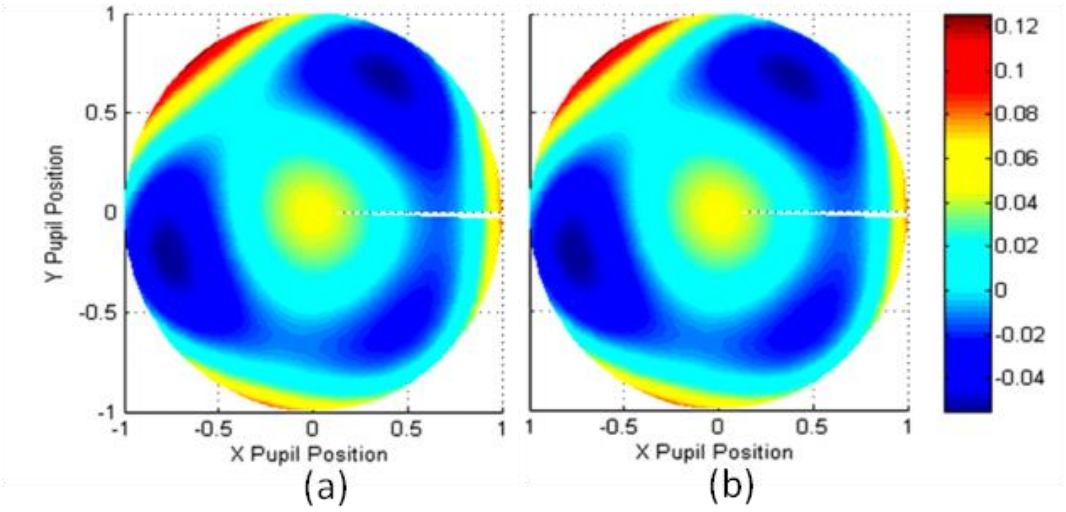

Figure 60 (a) Pupil wavefront map that was generated using random values for Z_5-Z_{11}, having a wavefront RMS of 30 milliwaves, (b) Predicted pupil wavefront after four iterations, using only Zernike coefficients up to Z_{11}

The results show a good match between generated and predicted wavefronts with an error RMS error of 0.3 mλ as seen in Figure 61. Figure 62 shows the progression of the four iterations for each aberration up to Z_{11}. It can be seen in Figure 62 that the initial value for each aberration is close to the randomly generated Zernike coefficient and is improved further after each iteration.

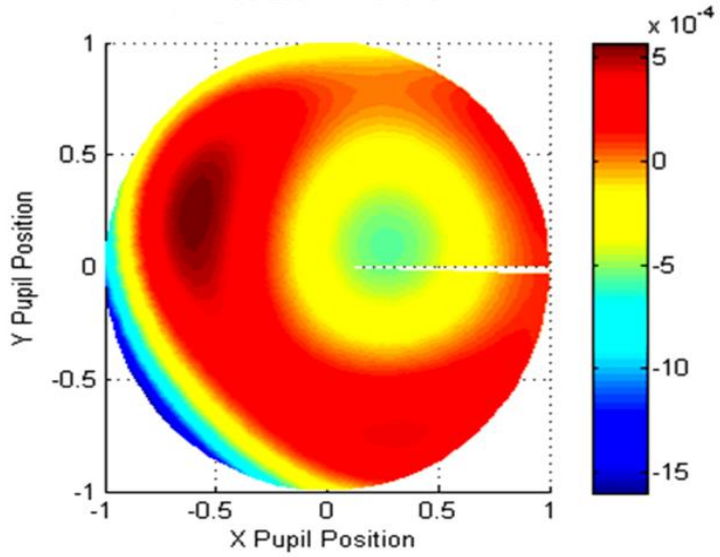

Figure 61: Residual pupil wavefront error after fitting with an RMS of 0.3 milliwaves

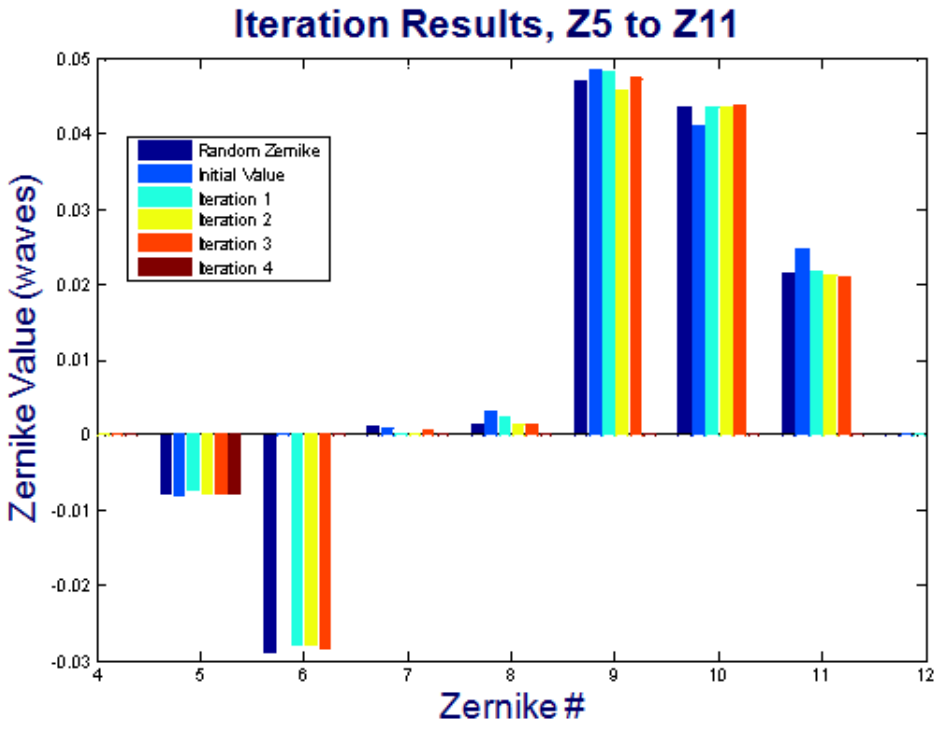

Figure 62: Plot of Zernike coefficient results after initial guess and 4 iterations

4.3.1 *CD Error Analysis*

An analysis of the influence of unaccounted random error in the CD SEM measurements and the influence on aberration fitting was completed. A random CD error was added to simulated CDs of the structures previously discussed structures. After the random error was added to the CD data, the CDs were used to extract the aberrated wavefront. This wavefront was then compared to the original wavefront used to generate the structure CDs, representing a non ideal and more realistic system. Figure 63 shows the result of this experiment for different standard deviations of error and number of repeat structures for each measurement. It can be seen that with increasing the CD noise, there is more error in the extracted wavefront. This can, however, be compensated for by increasing the number of repeat measurements, but suffers from diminishing returns after four repeated measurements.

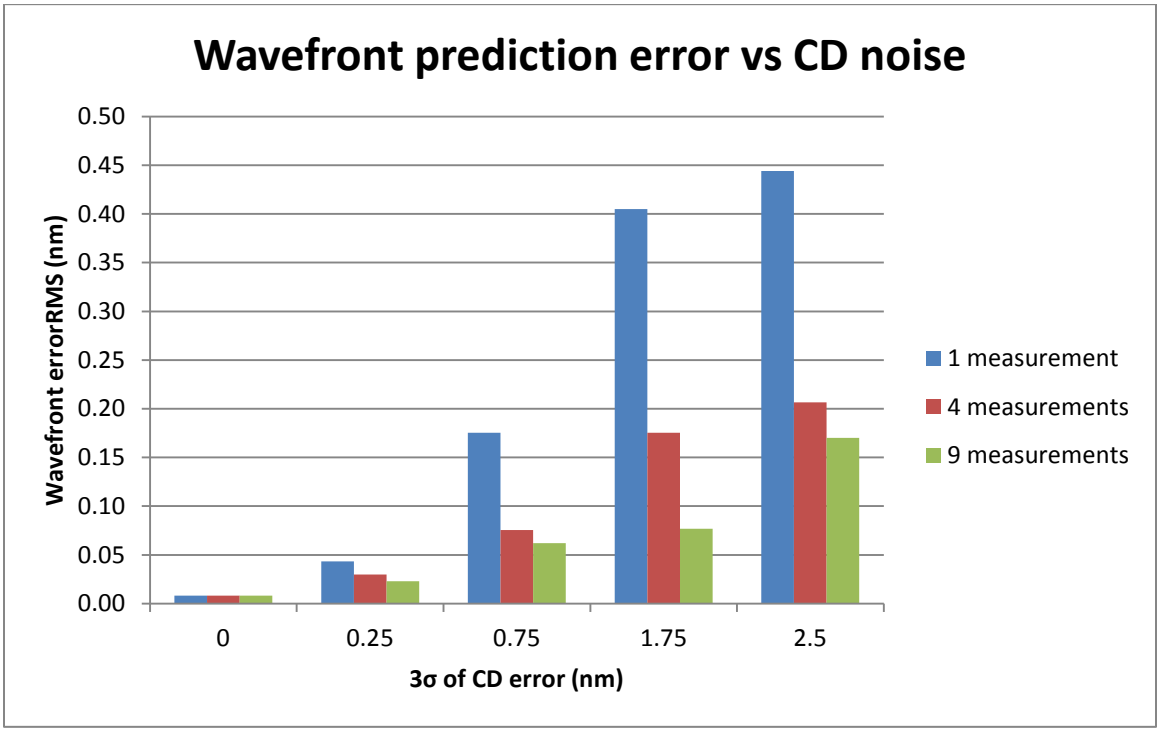

Figure 63: Error from extraction due to unaccounted for error in synthetic CD data for different amount of repeat measurements

4.4 **Target selection and experimental data collection**

The method described in the previous sections was verified on a preproduction full-field EUVL tool, ASML's alpha demo tool (ADT) located in CNSE [135]. The field size is 26 x 33 mm^2 in the wafer plane. Figure 37 shows a CAD drawing of the ASML ADT.

An FEM was conducted to determine the best exposure dose and focus before the collection of any dataset. Once best focus and dose were determined, data was collected in accordance to the modeling flow seen in Figure 59, requiring several different targets, and focus and dose settings.

Targets that were selected for experimental investigations were both sensitive to the aberration and available on reticles for the system under test. Table 10 shows the structures that were used, which are similar, but not exact to the screening simulation structures in Table 9. Because the method described in the previous section is flexible and input parameters can be modified as needed, similar structures can be substituted for a given target, making implementation with the generation of a dedicated reticle more feasible.

Table 10: Binary structures used for experimental validation on the ADT

Aberration	*Binary test Structure*	*Test Output*
Z_5 *astigmatism x*	*Horizontal and vertical lines* CD 40nm 1:1	*Horizontal and vertical line CD difference through focus*
Z_6 *astigmatism y*	*45º and 135º lines* CD: 40nm1:1	*45º and 135º line CD difference through focus*
Z_7 *coma x*	*Vertical five bar structure* CD: 35nm1:1	*1st and 5th bar CD difference*
Z_8 *coma y*	*Horizontal five bar structure* CD: 35nm1:1	*1st and 5th bar CD difference*
Z_9 *primary spherical*	*Horizontal lines through pitch* P64-192nm CD:32nm	*Best focus through pitch*
Z_{10} *trefoil x*	*Horizontal T-bar structure* V-pitch: 120nm H-Pitch:300nm V-CD: 30nm H-CD: 210nm	*Left and right bar end CD difference*
Z_{11} *trefoil y*	*Vertical T-Bar structure* V-pitch: 120nm H-Pitch:300nm V-CD: 30nm H-CD: 210nm	*Top and bottom bar end CD difference*

For each dataset, three resist-coated wafers were exposed on the EUV ADT; structures were repeated 8 times per field over 21 fields per wafer. The time between wafer exposures was kept at a minimum. The resist used for the experiments is 75 nm SEVR139 on silicon wafers. A focus meander was first carried out, centered at best focus (-0.05 μm) and having 21 steps of 20 nm. The focus meander was completed at best dose (20 mJ/cm^2), which was verified before exposure. The CD of pitch 80 nm (P80) lines in four orientations was measured to extract astigmatism. The change in the difference in CD per focus was fit to simulations to give an effective astigmatism value. By fitting to the slope of delta CD versus focus, neglecting the y intercept, the effects of shadowing can be neglected. Figure 64 shows an example of pitch 80 nm SEM images used in the astigmatism x fitting as well as CD values obtained through focus for horizontal and vertical lines with a duty cycle of 1:1 and pitch of 80 nm. There were 192

measurements for astigmatism x and the same amount for astigmatism y on the first wafer.

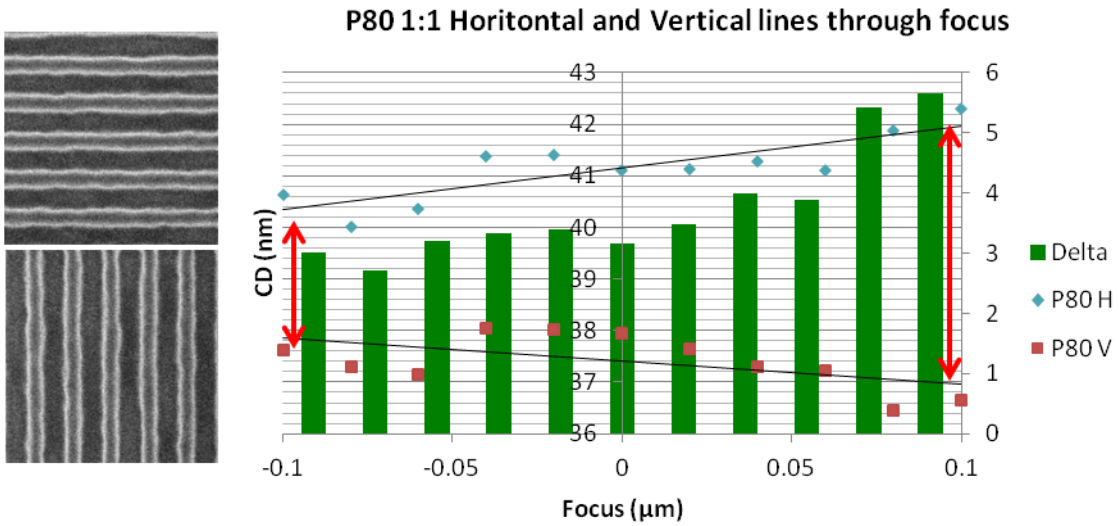

Figure 64: Pitch 80 nm horizontal and vertical lines with a duty ratio of 1:1, used to extract astigmatism x, line CD plotted through focus

The second exposed wafer consisted of an exposure series having 21 dies and was used for extraction of coma and trefoil. Being even aberrations, they are not sensitive to focus variations as discussed previously. For the extraction of coma the 1st and the 5th bar of a five bar structure were measured, as shown in Figure 65. A plot of the CD and delta CD of the 1st and 5th bar is shown in Figure 66, the vertical structure CDs used to extract coma x is shown in Figure 66 (a) and the horizontal five bar CDs used to extract coma y are shown in Figure 66 (b). The difference in CD was fit to simulations and an effective coma value was determined. Similarly, trefoil was fit to the CD difference of the ends of a T-bar structure shown in Figure 67. The CD and delta CD of the T-bar ends is shown in Figure 68. Figure 68 (a) shows the vertical T-bar structure CD and delta CD

used to extract trefoil x and Figure 68 (b) shows the CD and delta CD used to extract trefoil y.

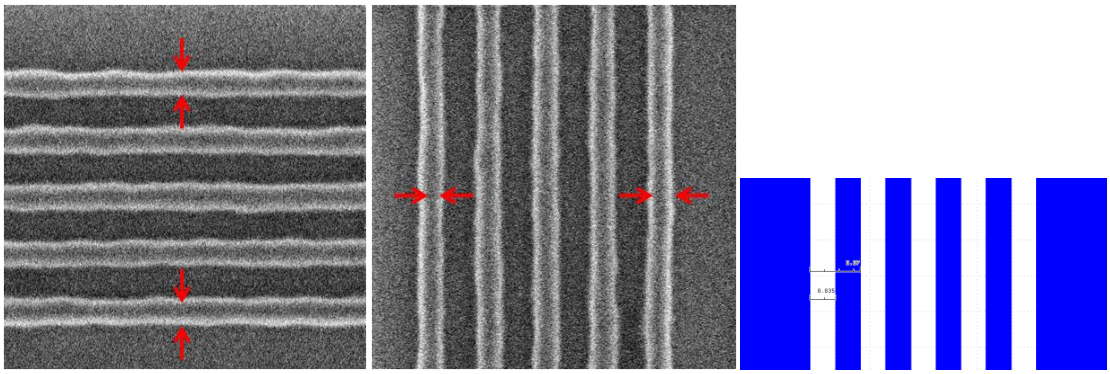

Figure 65: (left) SEM image of five bar structures used in the extraction of coma y and (center) coma y as well as (right) bright field five bar design

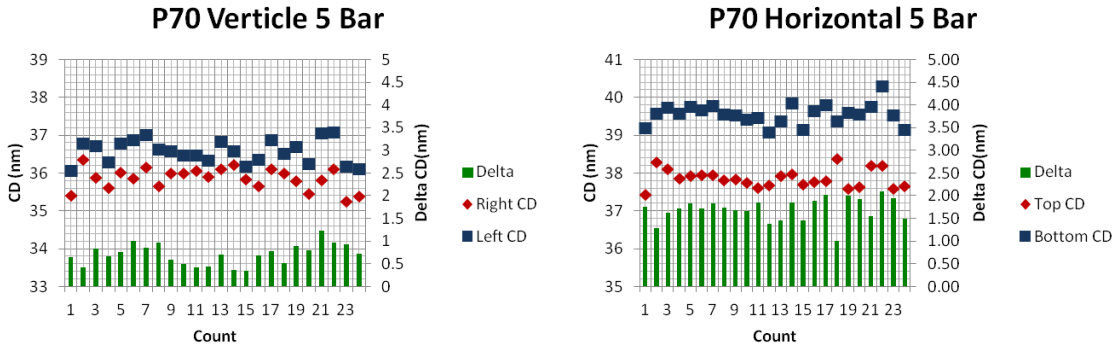

(a) (b)

Figure 66: Plot of CD and delta CD of the 1st and 5th bar of a (a) vertical and (b) horizontal five bar structure

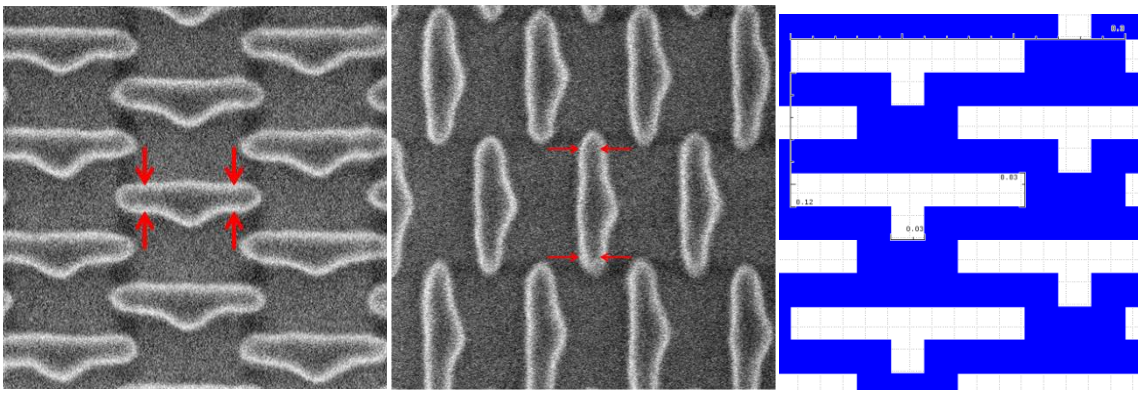

Figure 67 (left) SEM image of T-Bar structures used in the extraction of trefoil x (center) trefoil y as well as (right) bright field design of T-Bar structure

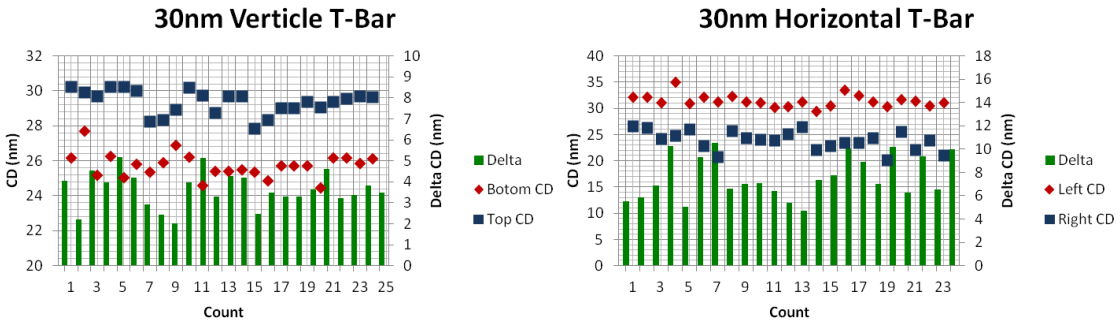

(a) (b)

Figure 68: Plot of CD and delta CD of the bar ends of a (a) vertical and (b) horizontal T-bar structure

The third exposed wafer was a focus exposure matrix (FEM) to determine best focus for several different pitches. The best focus was taken as the focus value where the through focus behavior is symmetric around that point. Figure 8 shows example SEM images of the five pitches that are measured, pitches 192 nm, 160 nm, 128 nm, 96 nm, and 64 nm with a 32 nm CD.

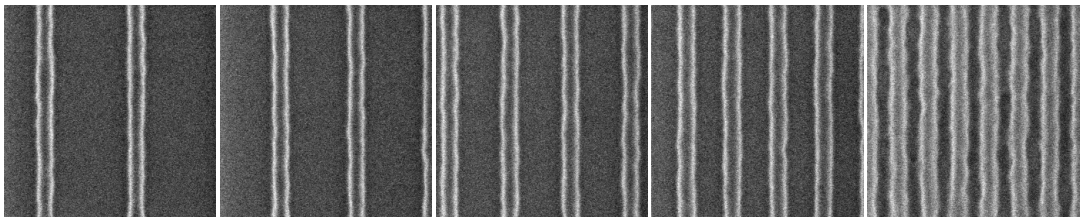

Figure 69: SEM images of (from left to right) pitches 192 nm, 160 nm, 128 nm, 96 nm, and 64 nm with a CD of 32 nm

The three wafers needed for a complete dataset were exposed on the same day, or within a few days to minimize tool variations, such as environmental or process fluctuations. Once data collection from the three wafers was complete, the measured values and experimental settings were fed into the fitting program.

A summary of the three wafers used in the experimental validation is shown in Table 11. Table 11 shows the scanner reticle ID, lot type (focus meander, exposure meander, FEM, production), estimated run time, dose, dose step, focus, focus step as well as the SEM recipe that were created for measuring the given targets on a Hitachi CD4000 CD SEM.

Table 11: Summary of the three wafers used in the experimental validation of the aberration extraction

Wafer 1	***Run Time***	***ReticleID***	***Lot Type***	***Dose***	***Dose Step***	***Focus***	***Focus Step***
Scanner Job	45 min	AMDROTATE7-9	Focus Meander	20 mJ/cm^2	-	-0.12 µm	0.01 µm
SEM Jobs	15 min	ibm_fenger/ibm_fenger_Rotatable1_45CCWP80					
	15 min	ibm_fenger/ibm_fenger_Rotatable1_45CWP80					
	15 min	ibm_fenger/ibm_fenger_Rotatable1_H_P80					
	15 min	ibm_fenger/ibm_fenger_Rotatable1_V_P80					
Wafer 2	***Run Time***	***ReticleID***	***Lot Type***	***Dose***	***Dose Step***	***Focus***	***Focus Step***
Scanner Job	1.2 hr	AMDROTATE7-9	FEM	20 mJ/cm^2	2.5 mJ/cm^2	0 µm	0.07 µm
SEM Jobs	1.5 hr	ibm_fenger/ibm_fenger_Rotatable1_V_TP					

Wafer 3	*Run Time*	*ReticleID*	*Lot Type*	*Dose*	*Dose Step*	*Focus*	*Focus Step*
Scanner Job	45 min	AMDROTATE7-9	Production	20 mJ/cm^2	-	-0.05 μm	-
SEM Jobs	15 min	ibm_fenger/ibm_fenger_Rotatable1_5B_V_P60					
	15 min	ibm_fenger/ibm_fenger_Rotatable1_5B_H_P60					
	15 min	ibm_fenger/ibm_fenger_Rotatable1_30V_LTB					
	15 min	ibm_fenger/ibm_fenger_Rotatable1_30H_180TB					

4.5 **Aberration Fitting and Experimental Results**

The CD-SEM data was formatted into one input file, which was loaded in the custom program called Binary Resist Image Based Aberration (BRIBA) fitting, which uses MATLAB^{TM} to interface with the PROLITH^{TM} simulator. Using lithography simulation, a model was created for the expected CD differences or focus shifts due to aberration. Then the experimental data was fit to a certain aberration level. This process of creating models and fitting data was repeated, forward feeding the aberration results to the next iteration.

The first step in the fitting algorithm is to generate a model for astigmatism. This is done sending the parameters for each structure, which are specified in the MATLAB^{TM} program, for PROLITH^{TM} simulation. These parameters include the simulation template file, exposure settings, lithography tool parameters, and other settings. The PROLITH^{TM} template file has the structure you are using with the appropriate tool parameters (NA, λ, σ, etc) as well as the appropriate models and metrology sites specified. The exposure and other settings are the focus range and focus step used to create the model, the resist threshold, the aberrated pupil function, specified by a series of Zernike coefficients (for the first model build the Zernike coefficients are typically all zero). Once the parameters are sent to the simulator, the structure is simulated with the given conditions and a CD

value is sent back to the fitting routine. This is done for all focus and astigmatism values, a matrix (focus X astigmatism) of CDs are generated. Using this CD data, the fitting routine fits a function to the delta CD data (horizontal-vertical or 45°-135° lines) in the form found in Equation (4.1).

$$Delta\ CD = a + b * Z_5 * + c * Focus + d * Z_5 * Focus \tag{4.1}$$

where *a*, *b*, *c* and *d* are model coefficients and *Focus* is the focus values used in the simulations and Z_5 is the astigmatism value used in the simulation. The same formula is used in astigmatism y (Z_6).

Once a model is made, the experimental data is fit. The fitting form is shown in Equation

$$ExpDelta\ CD = S + b * ExZ_5 + c * (ExpFocus + FS) + d * ExZ_5 * (ExpFocus + FS) \tag{4.2}$$

where *S* is a fit shadowing bias, *FS* is a focus shift between the model and the simulation (limited to 50 nm), *ExpFocus* is the experimental focus settings and *ExZ5* is an extracted astigmatism value. Note that the terms *S*, *a* and *FS* are offsets in delta CD and in focus and are neglected in the fitting of astigmatism, making the algorithm essentially fit astigmatism to the slope of delta CD over focus. The same formula is used for astigmatism x and y.

Concurrently, coma if fit using the CD difference between the 1st and 5th bar of a five structure. Similar to astigmatism, simulation parameters are sent from the fitting routine to the simulator. These parameters include the simulator template file, which has the tool, five bar structure, models, and metrology sites, and the exposure conditions,

including focus and resist thresholds. The simulation is run for a range of coma values specified and CDs are returned from the specified metrology sites. The delta CD between the 1st and 5th bar is then fit using the model form in Equation (4.3).

$$Delta\ CD = a + b * Z_7 * + c * Threshold + d * Z_7 * Threshold \quad (4.3)$$

where a, b, c, and d are fitting parameters, Z7 are the coma values used in the modeling, and Threshold is the small range of resist threshold values that were used in the modeling. Because a calibrated resist model was not used, a small range of threshold values were chosen to take an average delta CD value to create the model.

Once a model is created for coma, the experimental data is fit to the model. The fitting form is shown in Equation (4.4).

$$ExpDelta\ CD = a + b * Ex7_5 + c * Threshold + d * ExZ_7 * Threshold \quad (4.4)$$

where ExZ_7 is the extracted coma Zernike coefficient. The same model form is used for coma x and y as well as trefoil x and y.

Once values for astigmatism and coma are extracted, spherical aberration is fit. This is done by again creating a model by sending input parameters such as the simulator template file that has the tool, metrology and model parameters, as well as the exposure conditions. The exposure conditions include a wide focus range (±200 nm) and threshold. The structure parameters are also sent from the fitting routine including line pitch and line CD. A FEM is then conducted and best focus is determined by the focus setting that has the widest depth of focus for a 10% exposure latitude. The best focus is then sent back to the fitting routine for each pitch value. The through pitch array of best

focus values is then normalized by the smallest pitch, changing the values to a best focus shift for both the experimental and simulated results. The two arrays are then divided, giving an effective best fit for Z_9 as illustrated in Figure 52.

The final aberration that is fit is trefoil. Trefoil uses the same setup and model generation and fitting as coma, but with a different structure and metrology sites. Using Equation (4.3), a model is generated using the simulator and is then fit to experimental data in the form of Equation (4.4), substituting Z_7 for Z_{10} or Z_{11}. Once a first pass of fitting Z5 through Z11 is compete, the extracted values of each Zernike coefficient are then used as inputs for the simulator for generating a model, as seen in Equation (4.5).

$$Z_n^k = model_n^k\left(Z_{\{5-11\}}^{k-1}, Focus, Threshold, Z_n\right) \cdot \text{ExpData} \tag{4.5}$$

where Z is a Zernike coefficient, *ExpData* is the experimental data and model is the generated model.

Figure 70 shows the graphical user interface (GUI) of BRIBA and an example output of the fit pupil, Zernike coefficients and x and y cross-sections of the pupil. Also in the GUI are options that can be customized for a specific run. There are check boxes for selecting which aberrations to solve for, the default is all aberrations. There is also an input field for the maximum number of Zernike coefficients in a generated model (having a lower value will speed up the model generation, but may lose accuracy), maximum iterations, and the estimated wavefront scale (the default being 2 nm). The wavefront scale limits the algorithm from solutions that are outside of realistic, limiting aberration values with a peak to valley of up to 4X the wavefront scale term. There are also fields for specifying the range of a Zernike coefficient to use in generating a model.

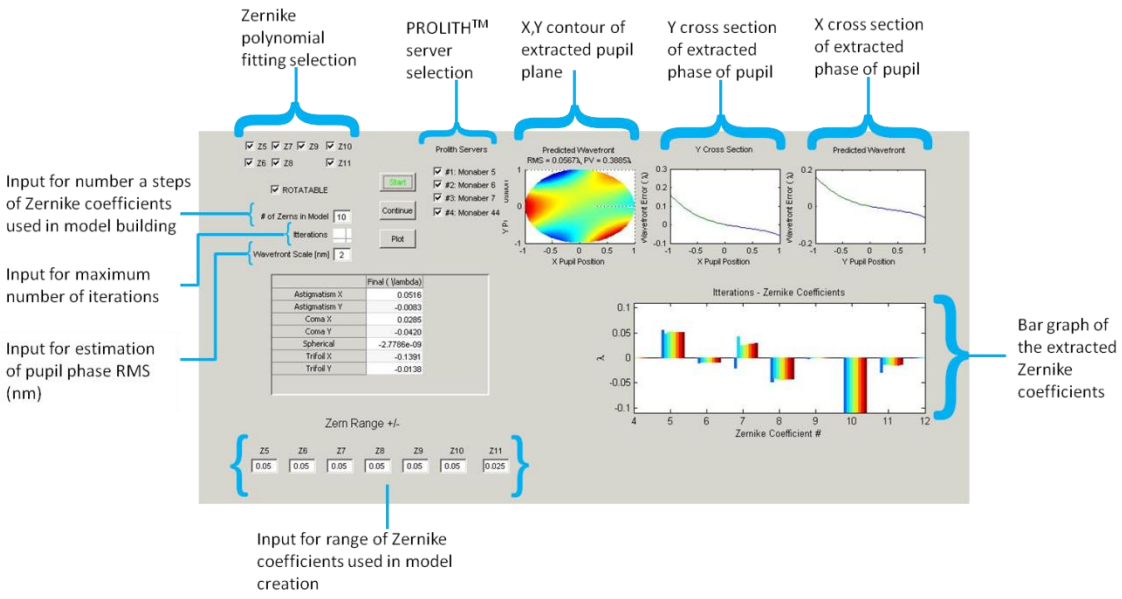

Figure 70: GUI for BRIBA with highlights of the features, showing an example output

Four datasets were collected in total, to determine the repeatability of this method as described in Table 11. Datasets A and B were at standard conditions measured approximately one month apart to show stability of the tool and algorithm. The resulting output of the fitting is shown in Figure 71 for dataset A and Figure 72 for dataset B. The dominate aberration that was seen for both datasets A and B was trefoil x (Z_{10}), with an extracted value of -91.3 and -104.9 mλ respectively.

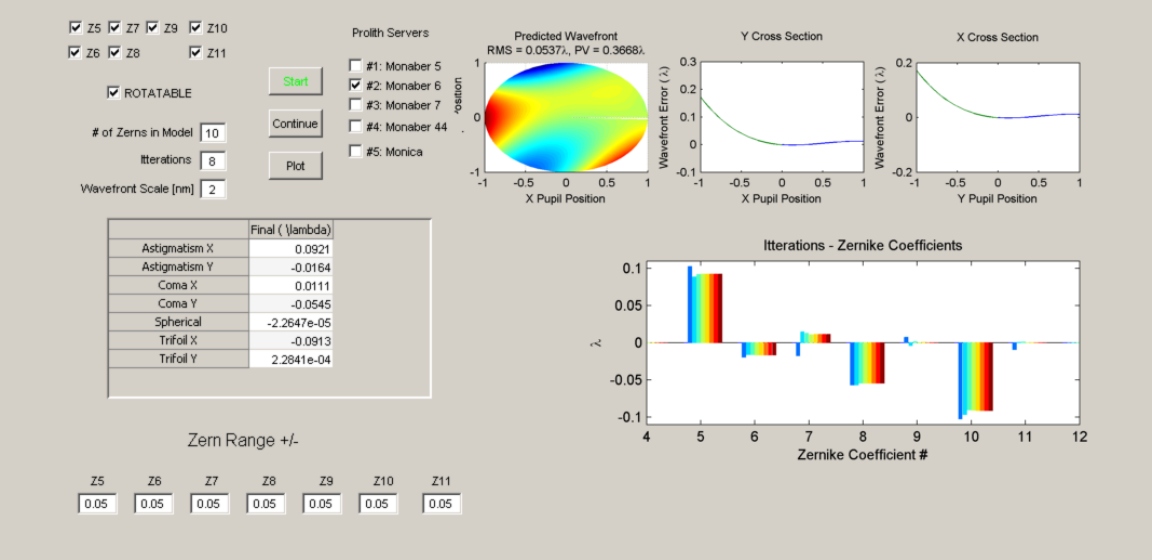

Figure 71: BRIBA output of dataset A after wavefront fitting

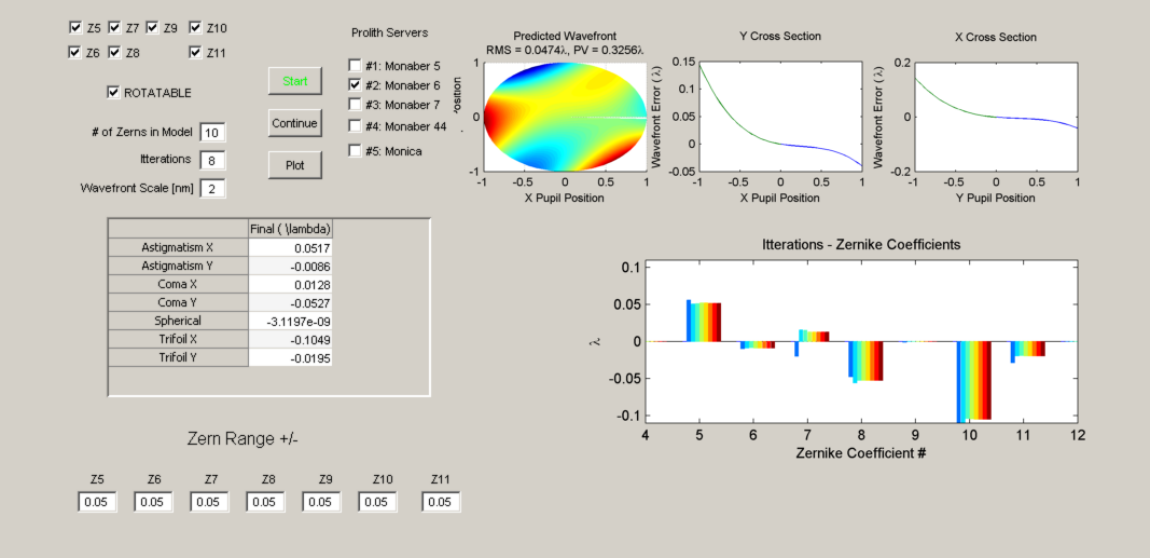

Figure 72: BRIBA output of dataset B after wavefront fitting

After about four iterations both dataset A and B converge to a stable solution for Zernike polynomial coefficients, shown in Figure 71 and 72. The difference in the extracted pupil from Dataset A and Dataset B is shown in Figure 73, having an RMS of 18.8 mλ.

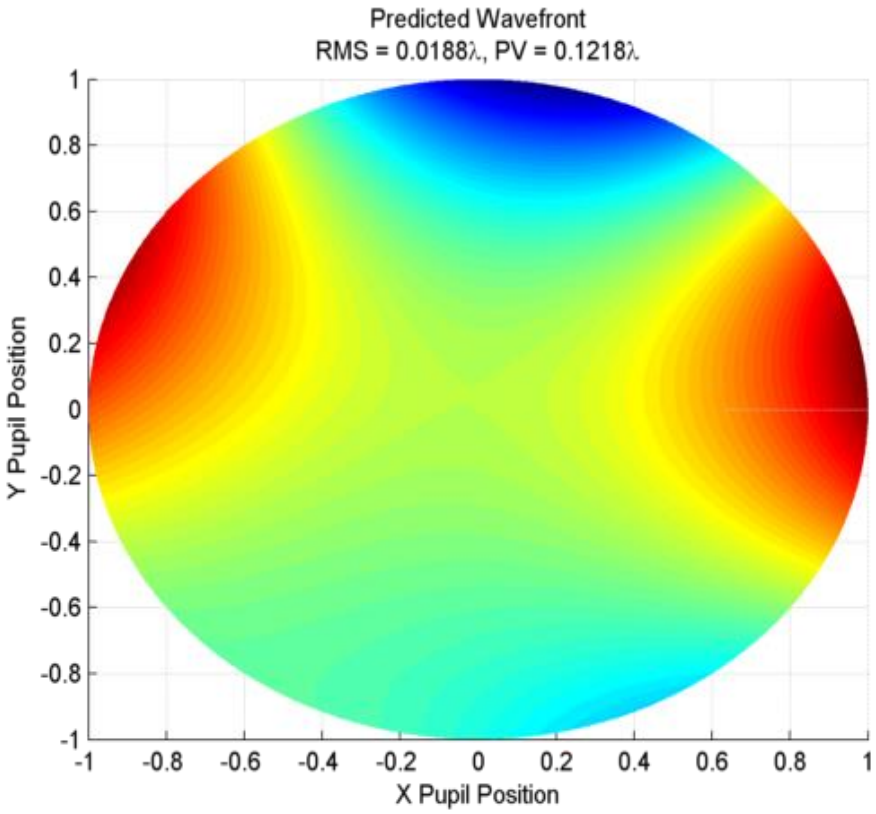

Figure 73: Pupil difference between dataset A and dataset B, having a RMS of 18.8 mλ

Dataset C was taken after a major lens repair of the system in standard conditions to see if the tool had drifted after maintenance and the result of the fitting are shown in Figure 74. Shown in both Figure 74 and 76, after about five iterations, the Zernike coefficients converge on a value. The difference between dataset B and dataset C is shown in Figure 75, having a RMS of 20.2 mλ, showing a difference that was greater than the baseline variability between dataset A and B, which was 18.8 mλ.

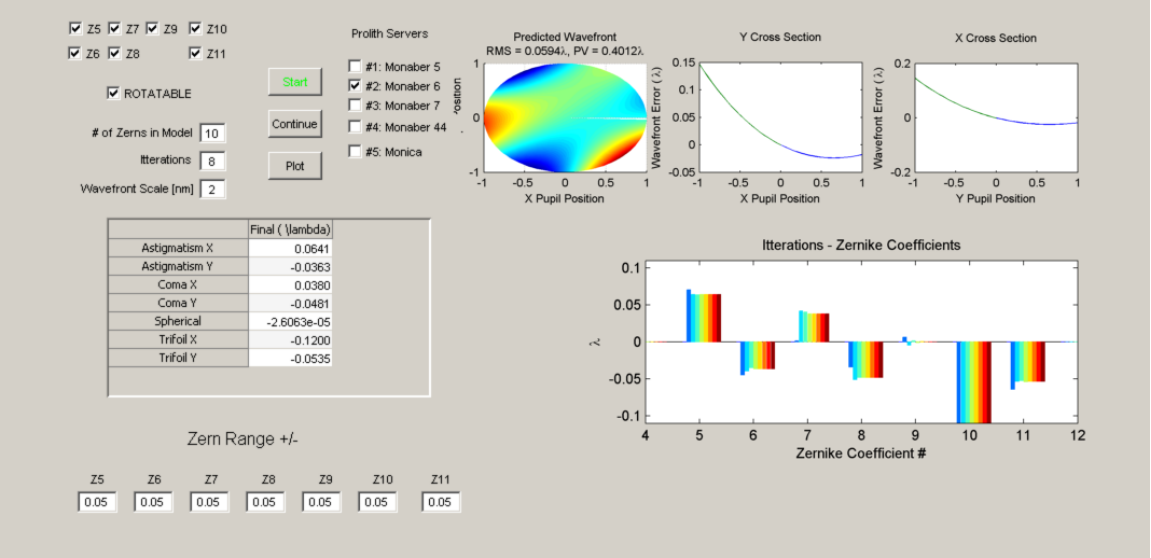

Figure 74: BRIBA output of dataset C after wavefront fitting

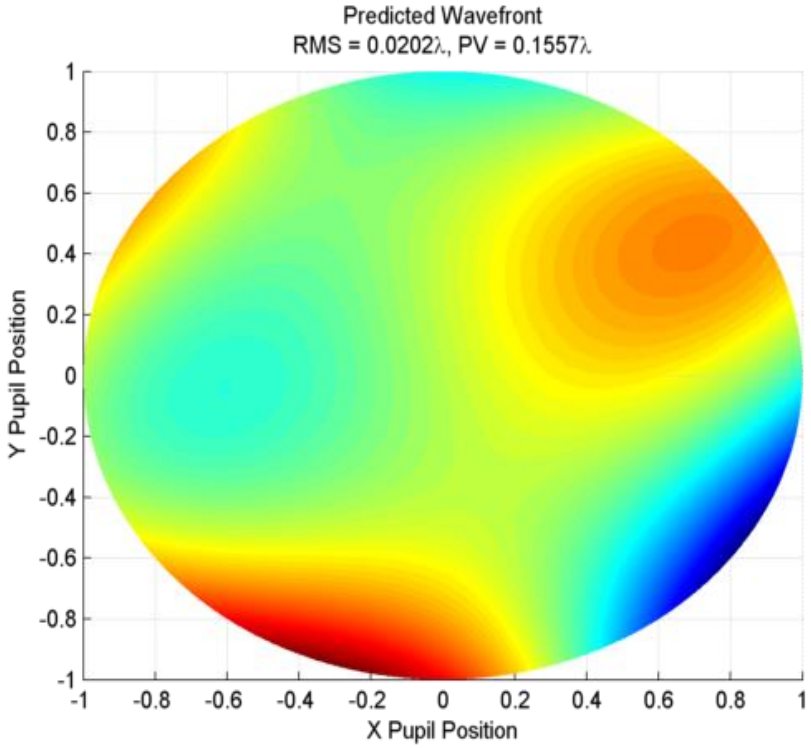

Figure 75: Pupil difference between dataset B and dataset C, having an RMS of 20.2 mλ

Dataset D, measured immediately after dataset C, was taken with machine constants altered to increase astigmatism x by ~50 mλ, to show the sensitivity of the method. The adjustments for the six mirrors in the ADT were each driven to a new value where it was calculated that astigmatism would be 50 mλ higher than the baseline. The results of this exercise are shown in Figure 76.

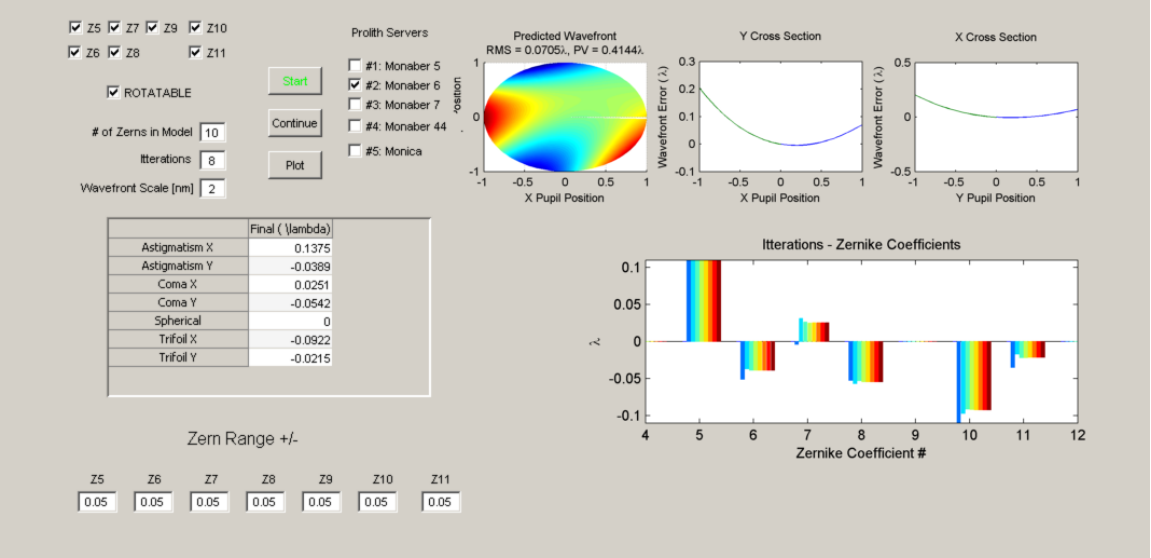

Figure 76: BRIBA output of dataset D after wavefront fitting

The difference between dataset C and dataset D is shown in Figure 77, having a RMS of 33.9 mλ, showing a difference that is greater than the baseline variability between dataset A and B. The signature of the pupil resembles that of astigmatism x, which is shown in Figure 39.

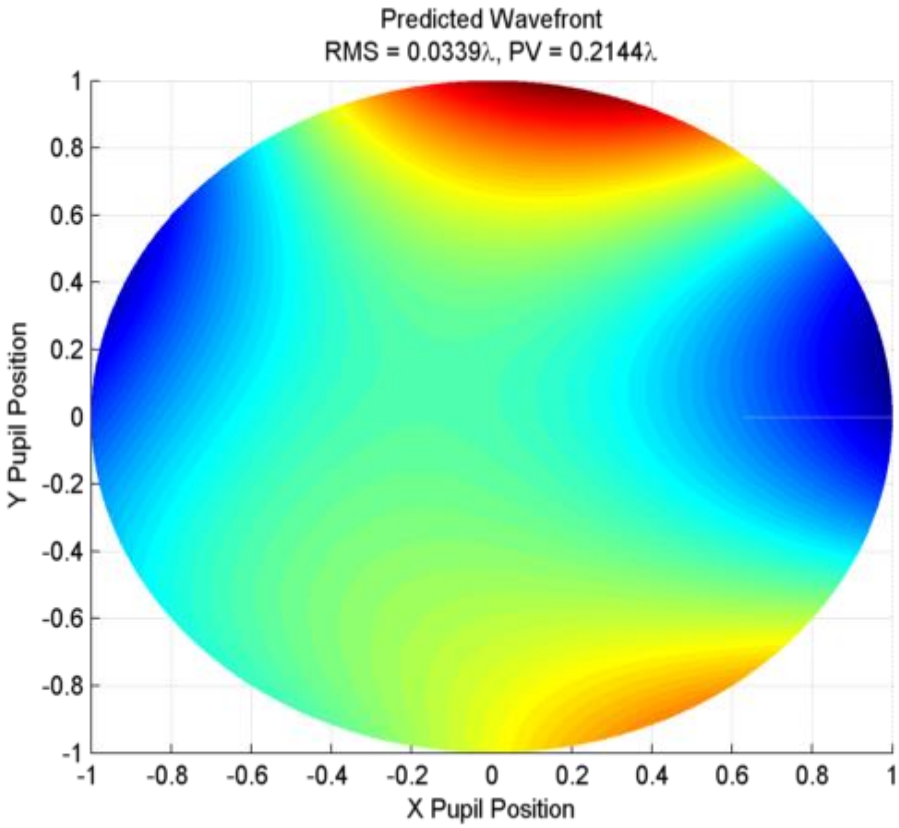

Figure 77: Pupil difference between dataset C and dataset D, having an RMS of 33.9 mλ

The extracted Zernike polynomial coefficients for Z_5-Z_{11} are shown in Figure 78 for each of the four datasets. The largest aberration consistently found on the tool was trefoil x (Z_{10}). The datasets seem to be in reasonable agreement of the aberration signature of the tool. Also dataset D, with the increase of astigmatism x by ~50 mλ, shows a definite increase in the extracted value of Z_5, with a difference from dataset C of 73 mλ.

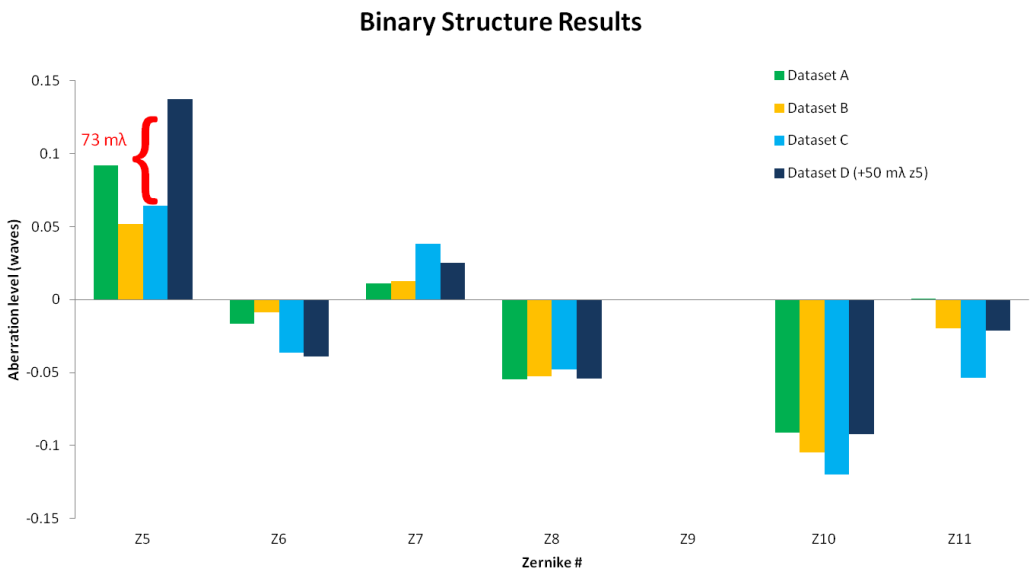

Figure 78: Graph of the extracted Zernike polynomial coefficients for four collected datasets from the ADT

The datasets that were collected show the variability of the method of extracting aberrations from the ADT. The variability can be attributed to the equipment, the process, or the metrology. From Figure 77 and 78 it can be seen that by altering the mirror parameters an increase in astigmatism x was confirmed and seen in the difference between the dataset before the mirror parameters were changed and after, thereby confirming the sensitivity of the method.

5. PHASE TARGETS USED IN ABERRATION MONITORING

Using phase targets in resist methods to extract lithography lens aberrations have been shown to be more sensitive to aberrations than binary targets alone [58,71]. This section will discuss the approach to utilizing phase targets for EUVL. In EUVL, creating a chromeless phase-shifting mask is currently not a commercial process. Therefore obtaining a strong phase shifting mask for EUVL can be difficult. Previous work for creating a phase shifting mask [43] was repeated to fabricate a test reticle. The mask was fabricated by using a standard multilayer stack but in the phase shifted regions the multilayer was partially etched to a depth of $n\lambda/2$. The test reticle was created for the SEMATECH Microexposure tool (MET) at Lawrence Berkeley National Labs, shown by a CAD rendering in Figure 79. The MET is a reflective, two-element, 5X-reducation optical system with a reflective reticle [103,120]. To achieve an on-axis system the reticle is tilted by four degrees and the wafer by 0.8 degrees.

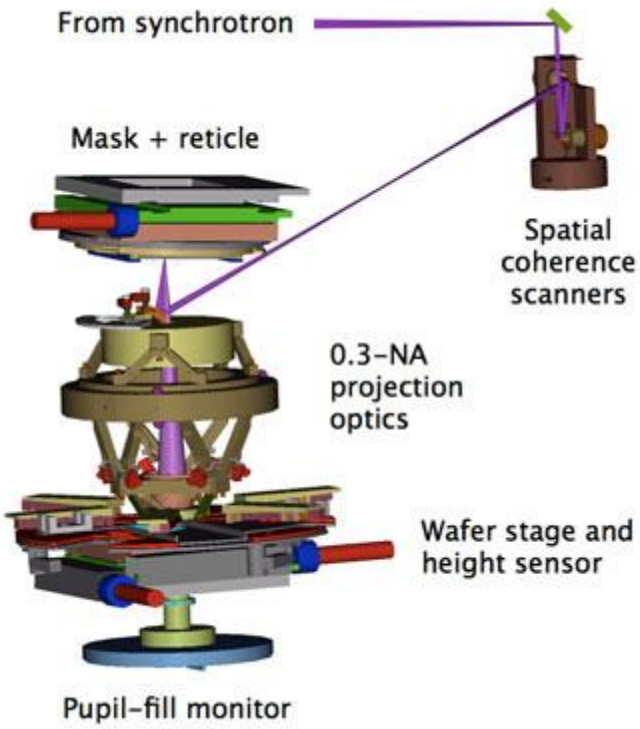

Figure 79: CAD drawing of the major components of the Berkeley MET exposure station as well as the EUV beam path [139]

5.1 **Simulated Results**

Several simulations of phase targets were completed with various exposure, illumination, and pupil conditions. Several CD measurement points are used to describe an output. The defined measurement points are shown in Figure 80, having a total of 40 measurements per phase wheel image. A plot of the difference in CD from nominal for a phase wheel with L1=50 nm, L2=L3=80 nm, L4=75 nm, imaged with NA=0.3, σ=0.3 and 80 mλ astigmatism x (Z_5) is shown in Figure 81. As expected the greatest CD change is from the measurement locations in the X (locations 1-6, 29-32) and Y (locations 7-12, 25-28) orientations through focus. This was done for each Zernike aberration, and each has a unique CD signature.

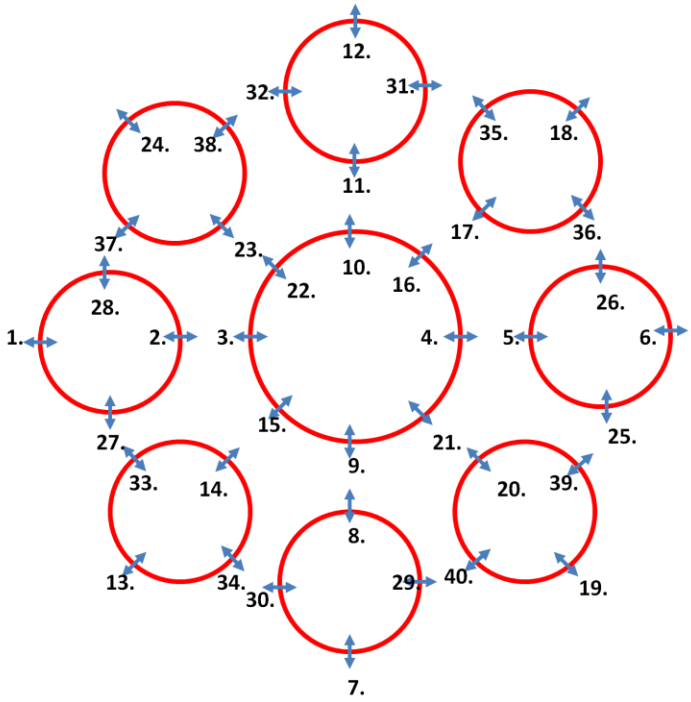

Figure 80: Drawing of a phase wheel with the CD measurement points labeled

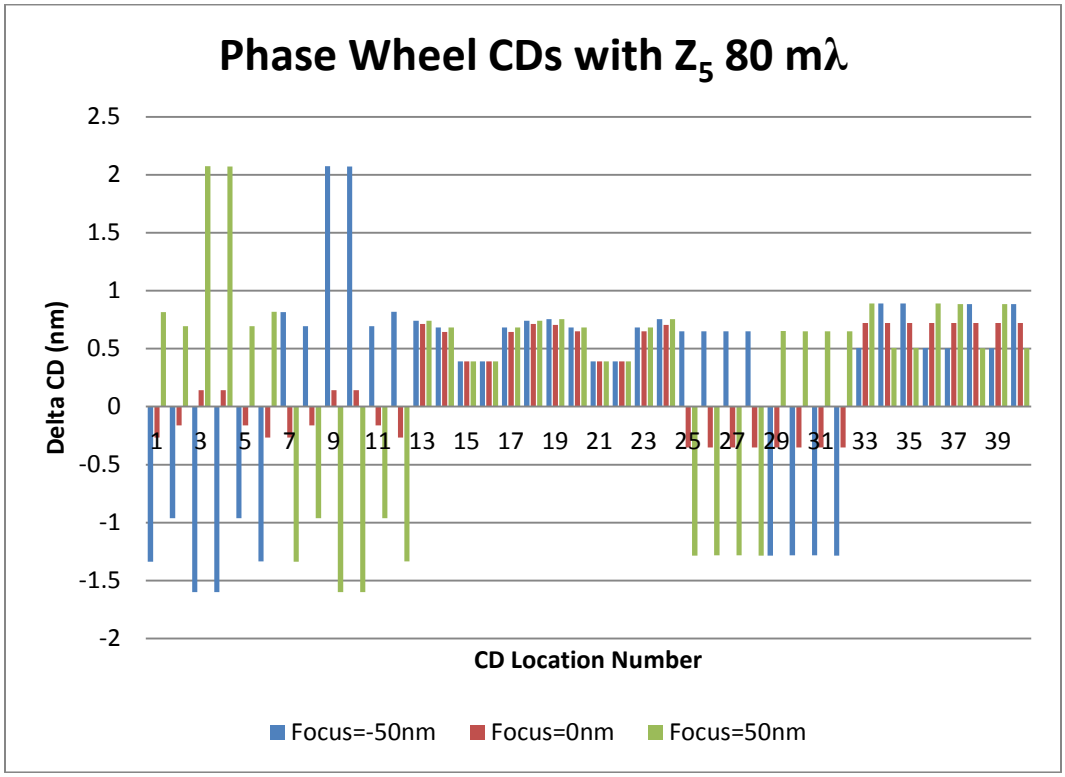

Figure 81: Plot of difference in CD from nominal in phase wheel target with L1=50nm, L2=L3=80 nm, L4=75 nm with 80 mλ astigmatism x

A plot of the difference in CD from nominal for a phase wheel with L1=50 nm, L2=L3=80 nm, L4=75 nm, imaged with NA=0.3, σ=0.3 and 80 mλ coma y (Z_8) is shown in Figure 82. As expected the greatest CD change is from the measurement locations in the Y (locations 7-12, 25-28) orientations, with no dependence on focus. Some measurement locations in 45 degree orientations also showed a response, this is due to interactions with the Y oriented structures.

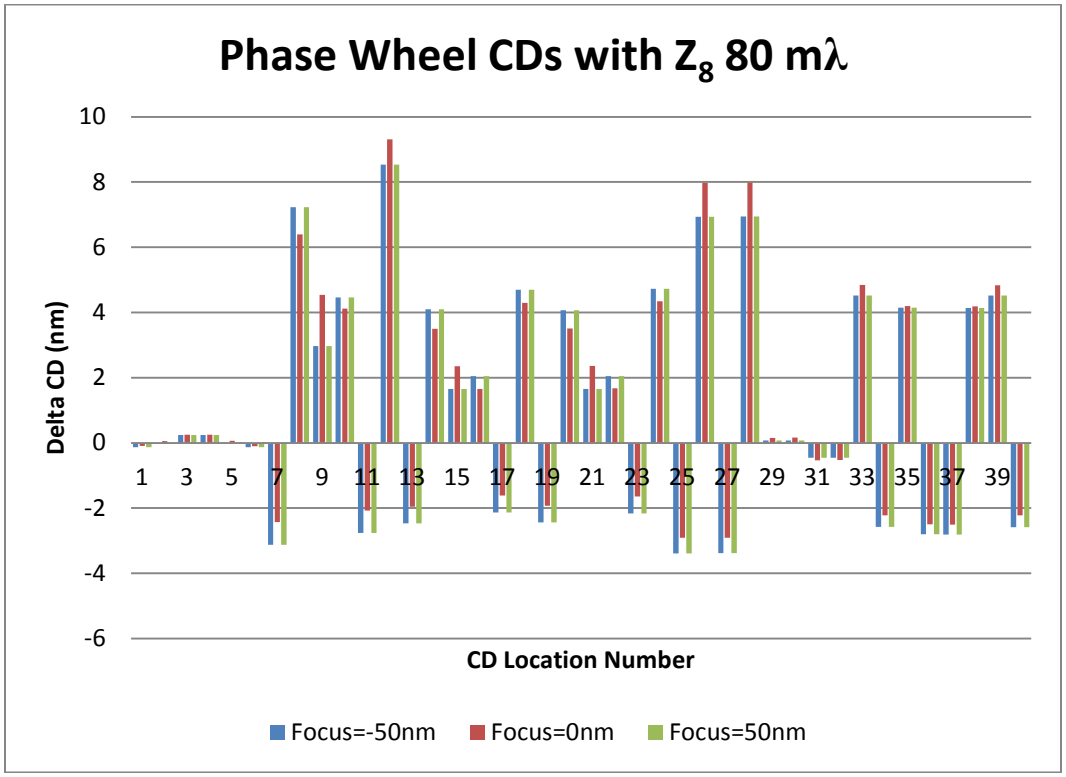

Figure 82: Plot of difference in CD from nominal in phase wheel target with L1=50nm, L2=L3=80 nm, L4=75 nm with 80 mλ coma y

Shown in Figures 83 and 84 are the plots of CD for each measurement location on the phase wheel for secondary and tertiary coma y respectively. The CD responses are both similar to primary coma y, but are different in many measurement locations,

measurement locations 39 and 40 for example. Having these differences in CD response allows for unique pupil solutions for a given phase wheel CD set.

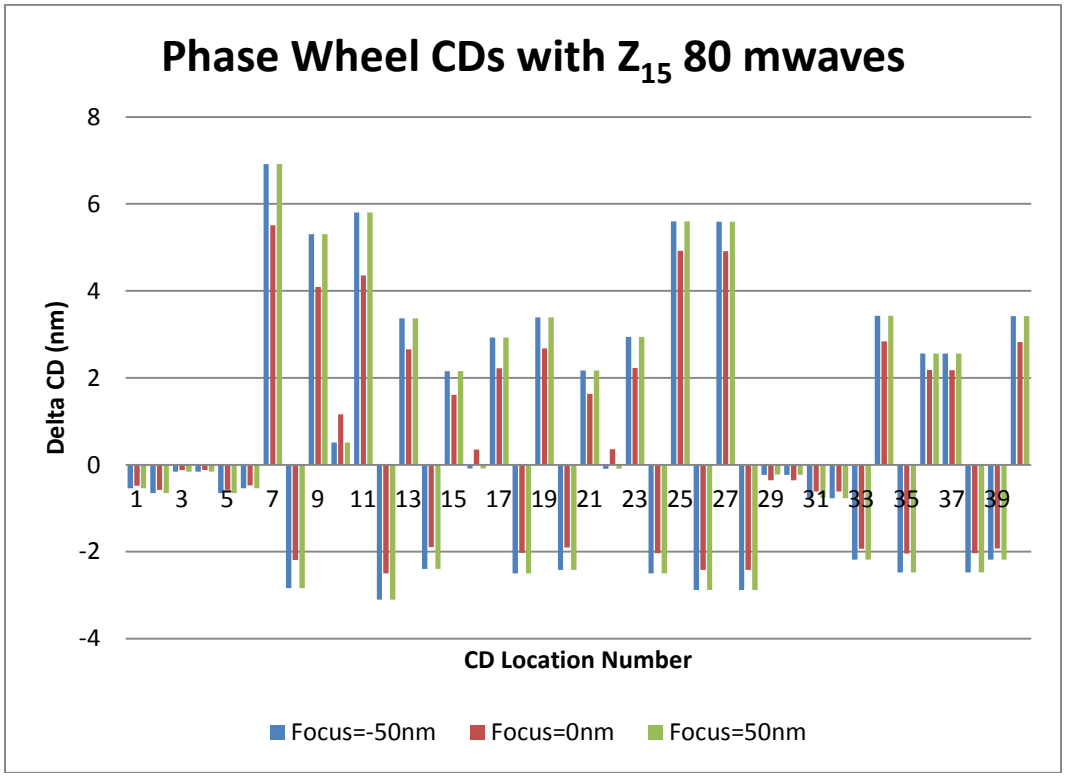

Figure 83: Plot of difference in CD from nominal in phase wheel target with L1=50nm, L2=L3=80 nm, L4=75 nm with 80 mλ secondary coma y

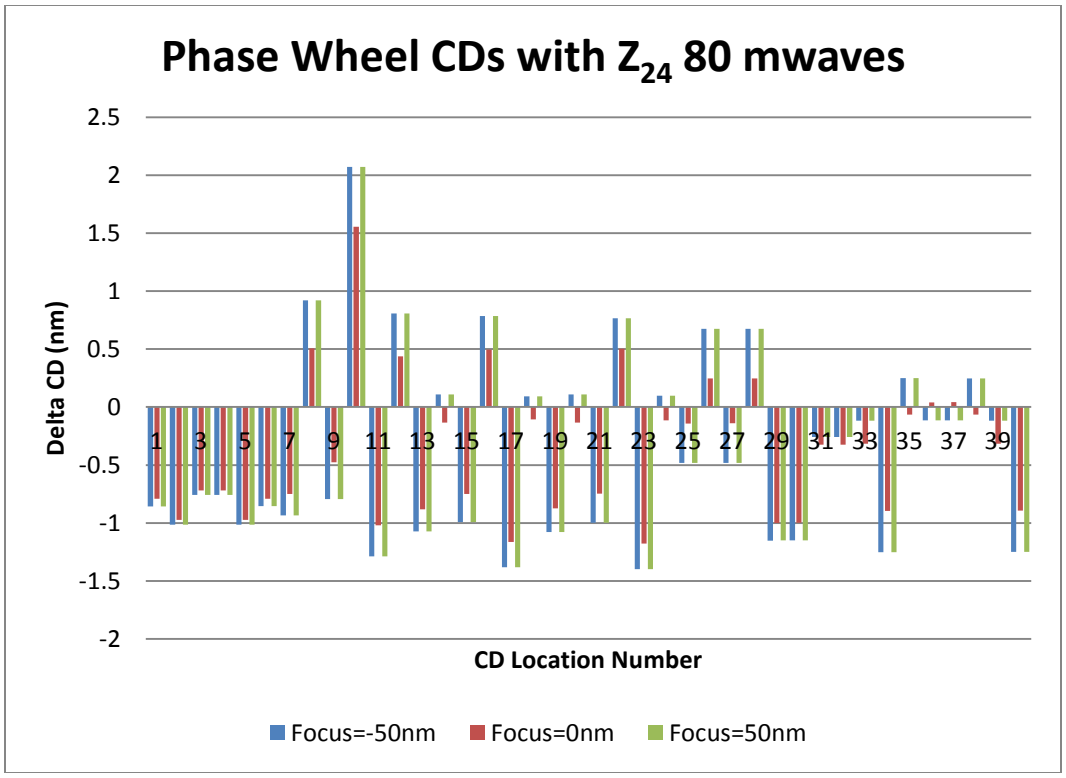

Figure 84: Plot of difference in CD from nominal in phase wheel target with L1=50nm, L2=L3=80 nm, L4=75 nm with 80 mλ tertiary coma y

5.2 Phase Target Model Flow

A method similar to the algorithm for binary targets was used to utilize phase targets in aberration extraction for EUVL. The model flow used CD measurements and a global minimization algorithm. The phase flow used a phase wheel target with 40 CD locations, shown in Figure 80. The response function, examples shown in Figure 81, 82, 83, and 84 of a given aberration, was used to find the lease square fit for given simulated CDs with a randomly generated aberrated wavefront. After initial least square fits, the solved Zernike coefficients are then used to create a new response function for each Zernike term and a least squares fit is preformed. This is repeated until a stable solution

is reached. The algorithm then uses global optimization on all Zernike polynomials to further simulate the wavefront. The extraction flow is shown in Figure 85.

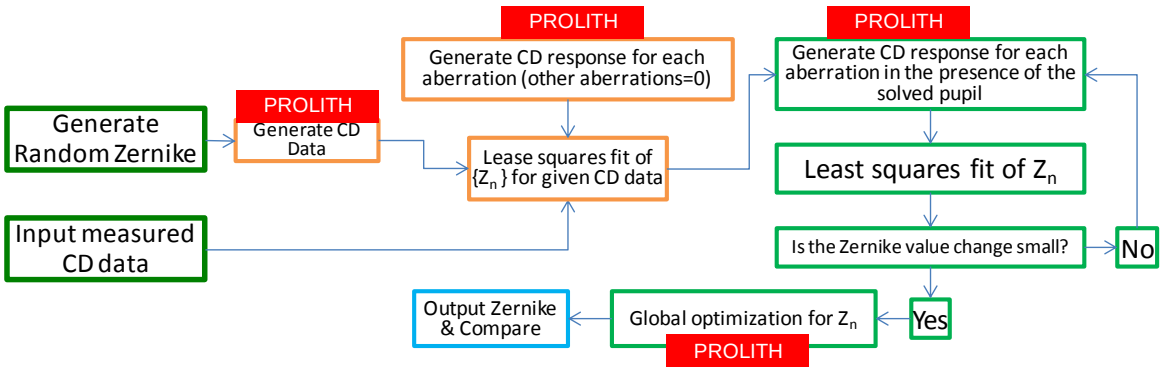

Figure 85: Utilized model flow for phase structures

A randomly generated wavefront utilizing Z_5-Z_{36}, was used to generate CD values of the phase wheel seen in Figure 80. The CDs were generated in a coherent EUVL system with a wavelength of 13.5 nm, NA of 0.3. The phase wheel had an L3=75 nm, L2=L1=50nm. The randomly generated wavefront is shown in Figure 86. The response function of the CDs for each aberration, Z5-Z36, was generated for this EUVL system. The response function is the difference between the measured CD with no aberration and with a specific aberration. Even aberrations, such as astigmatism, used the difference in CD from a focus value of -60 nm and 60 nm. Using these CD responses a least squares fit was completed and an initial wavefront was extracted. This process was then repeated until a stable wavefront was reached, using the wavefront extracted in the last iteration to create the response function of the new iteration. The wavefront after this step is shown in Figure 87 and the difference in this wavefront and the randomly generated wavefront is shown in Figure 88, with an error rms of 10.1 mλ. After this process is complete, a

global optimization is completed. The global optimization directly interfaces with PROLITH^{TM} and manipulates each aberration value to obtain a smaller rms error from measured to simulated CD. The predicted wavefront and wavefront error are shown in Figures 89 and 90, with an rms error of 8.9 mλ.

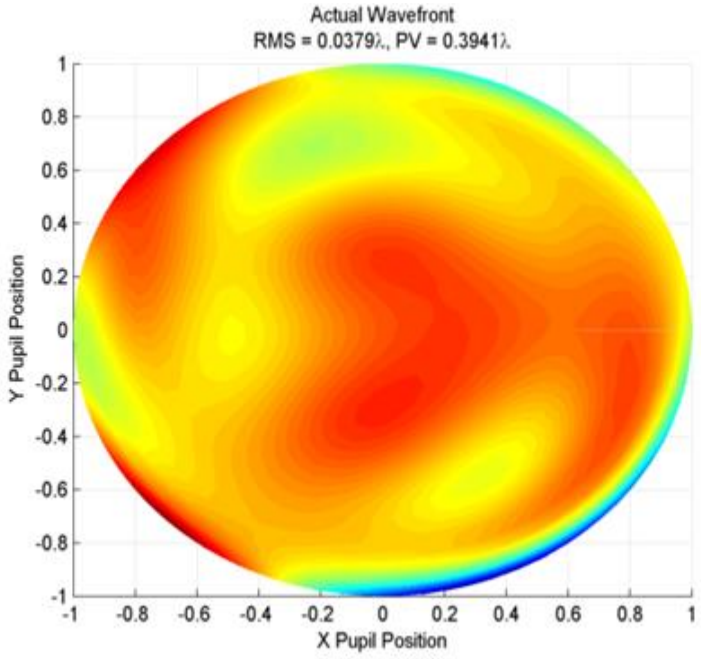

Figure 86: Randomly generated wavefront, with an rms of 37.9 mλ

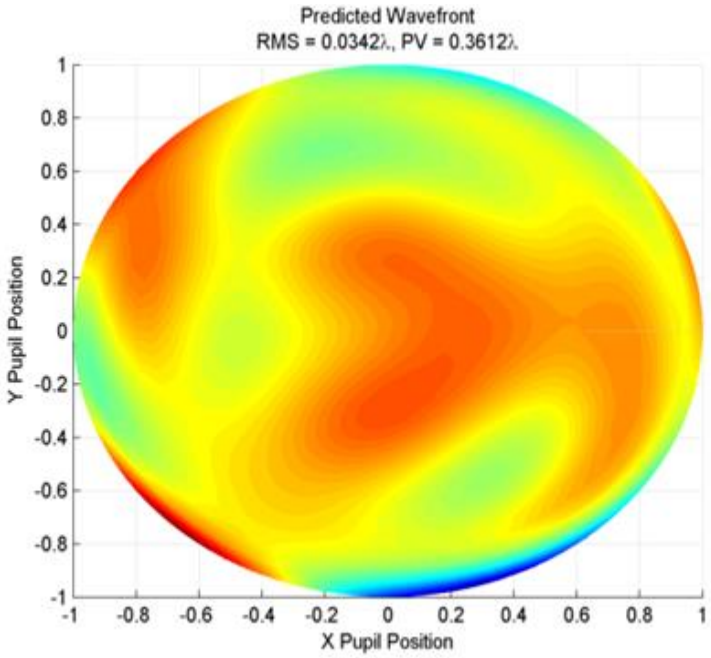

Figure 87: Extracted wavefront after least squares fit, showing an rms of 34.2 mλ

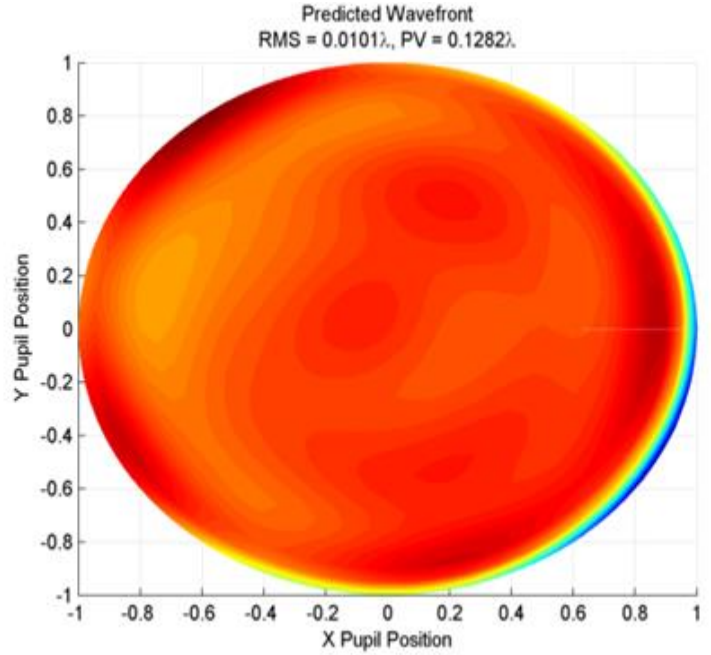

Figure 88: Wavefront difference between the extracted wavefront after least mean squares fit and the randomly generated wavefront with an rms error of 10.1 mλ

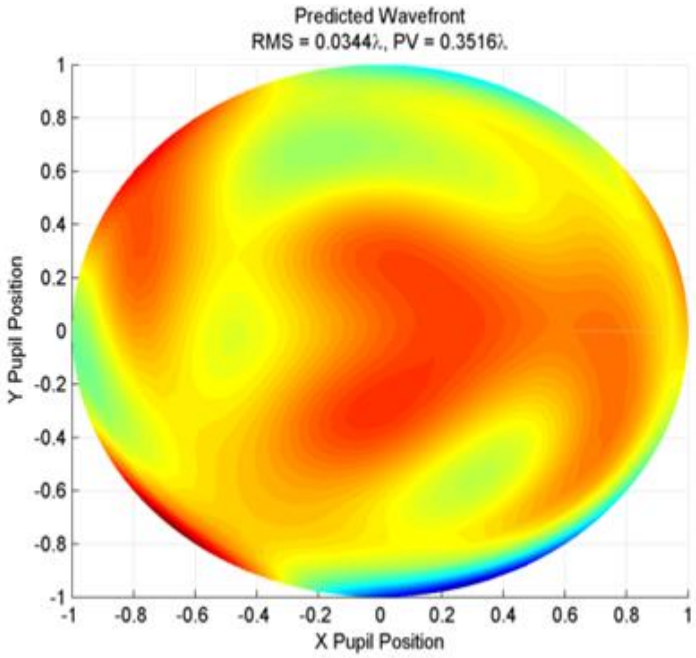

Figure 89: Extracted wavefront after 400 iterations of global fitting, with a wavefront rms of 34.4 mλ

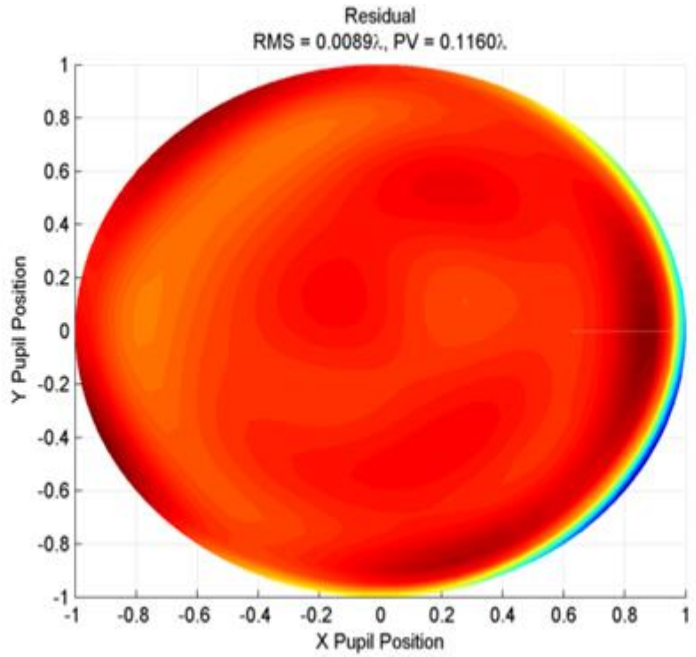

Figure 90: Wavefront difference between the extracted wavefront after 400 global iterations and the randomly generated wavefront with an rms error of 8.9 mλ

5.3 **Reticle Layout for Phase Targets**

Multiple phase targets were designed on the reticle, with multiple variations in dimension. The targets types that were included are three bar structures, phase disk structures, and phase wheel structures. The layout of the test clip for the phase reticle is shown in Figure 91, with eight rows of three bar structures on the top, in four orientations, followed by one row of phase disk structures, and on the bottom are ten rows of phase wheel structures. From left to right on the test clip, the on wafer CD varies from small (40-50 nm) to large(330-340 nm). Each row of a given target has different spacing and sizing between the features.

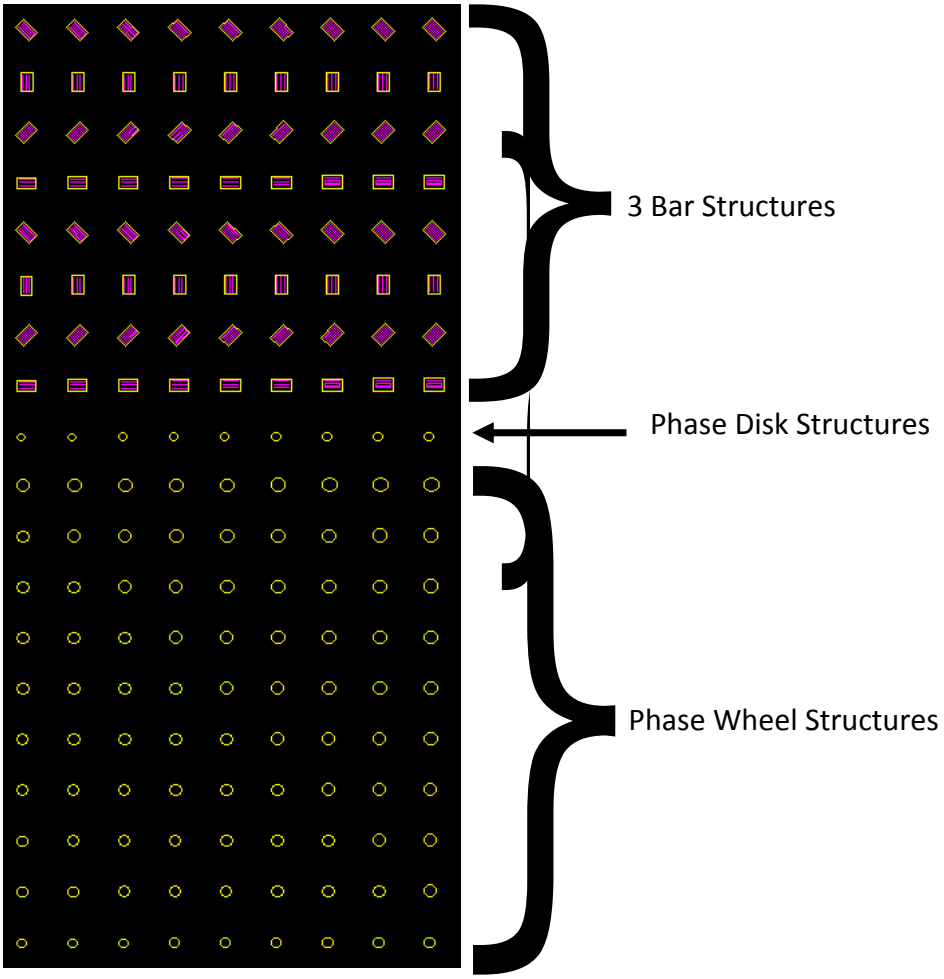

Figure 91: Phase target clip for EUVL

The labeling convention for each target type uses one feature size (in nm) that was incremented from left to right as the first number, this is followed by a series of letters that represent a multiplication factor for another feature dimension in the target. The multiplication factors that were used and their corresponding letter are listed in Table 12. For example, the label for a phase wheel with a peripheral disk of 50 nm and a center disk of 85 nm, a spacing of 60 nm between the center ring and outer disk, and a spacing of 75 nm between the outer disk and the guard disk would be:

50(50/50)(60/50)(100/50)(75/50) or 50(1X)(1.2X)(1.7X)(1.5X) or 50ACHF.

Table 12: Test structure labeling key

Layout Symbol	***Multiplication Factor***
A	1
B	1.1
C	1.2
D	1.3
E	1.4
F	1.5
G	1.6
H	1.7
I	1.8

The dimensions that are varying in each target type are designated by L1, L2, L3, and L4. In the three bar targets, L1 is the 1st and 3rd bar CD, L2, is the spacing between the 1st or 3rd bar and the center bar, L3 is the center bar CD, and L4 is the spacing between the 1st or 3rd bar and the dark boarder as seen in Figures 92 and 93.

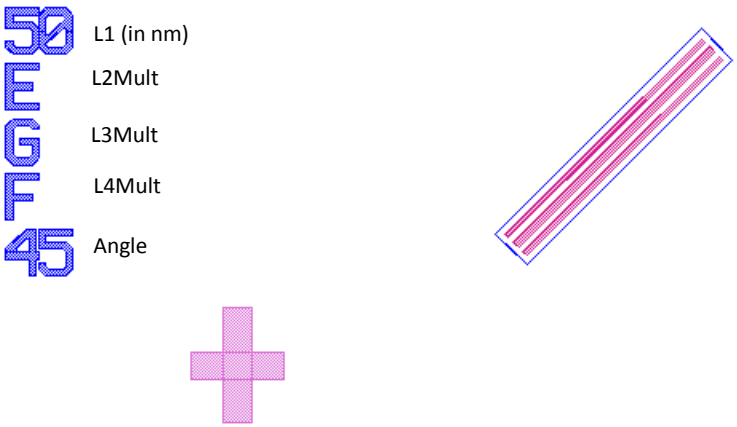

Figure 92: Three bar phase structure with label and SEM alignment mark

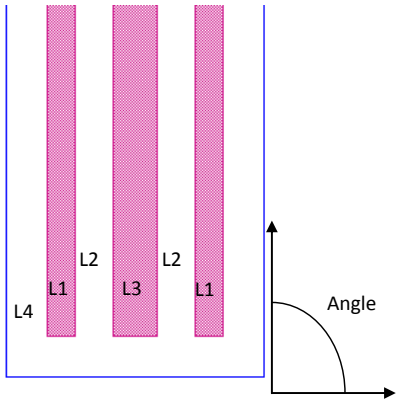

Figure 93: Three bar structure with the definitions of L1, L2, L3, L4, and angle

The three bar structure had variations of the 1st and 3rd bar from 50 nm to 340 nm in 5 nm steps with multipliers for L1, L2, L3 and L4 of (1X)(1.4X)(1.6X)(1.5X) and (1X)(1.6X)(1.4X)(1.5X) for four orientations (0°, 45°, 90°, -45°). A summary of the variations of the three bar structure are shown in Table 13 as well as the relative location of the given row from the bottom of the test clip (Y).

Table 13: Rows of three bar structures included on the test chip and their Y location relative to the bottom

L1Mult	*L2Mult*	*L3Mult*	*L4Mult*	*Angle*	*Y µm*
A (1X)	E (1.4X)	G (1.6X)	F (1.5X)	0	110
A (1X)	E (1.4X)	G (1.6X)	F (1.5X)	45	120
A (1X)	E (1.4X)	G (1.6X)	F (1.5X)	90	130
A (1X)	E (1.4X)	G (1.6X)	F (1.5X)	-45	140
A (1X)	G (1.6X)	E (1.4X)	F (1.5X)	0	150
A (1X)	G (1.6X)	E (1.4X)	F (1.5X)	45	160
A (1X)	G (1.6X)	E (1.4X)	F (1.5X)	90	170
A (1X)	G (1.6X)	E (1.4X)	F (1.5X)	-45	180

For the phase disk test pattern, the parameter L1 is not used, the spacing from the disk to the dark boarder is given by L2+L4, and the disk CD is given by L3. The phase disk test pattern parameter L3 is incremented from 40 nm to 330 nm in 5 nm increments. Figure 94 shows the phase disk structure along with its label. One row of phase disk structures were included with multiplication factors of (-)(1.4X)(1X)(1.5X) as seen in Table 14.

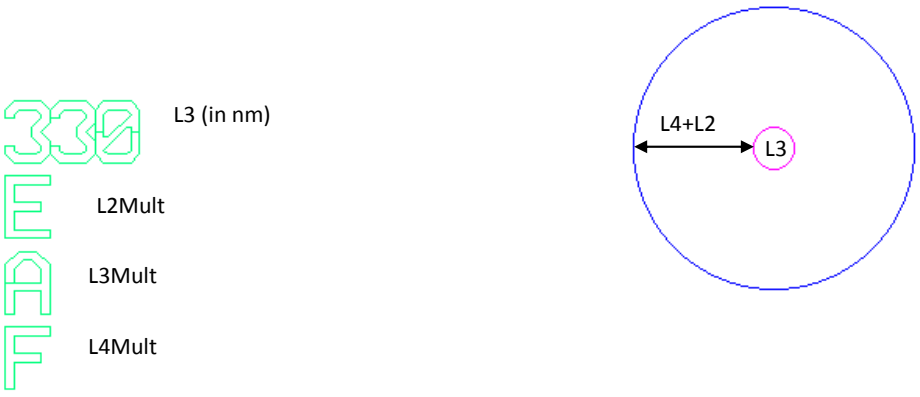

Figure 94: Phase disk structure with label and definitions of L2, L3, and L4

Table 14: Row of phase disk structures included on the test chip and the Y location relative to the bottom

L1Mult	*L2Mult*	*L3Mult*	*L4Mult*	*Y µm*
-	E (1.4X)	A (1X)	F (1.5X)	100

In the phase wheel targets, L1 was the outer disks CD, L2 was the spacing between the outer disks and inner disk, L3 was the inner disk CD, and L4 was the spacing between the outer disk and the dark boarder. Figure 95 shows a phase wheel structure and its label. The outer disk CD (L1) was varied from 50 nm to 340 nm in 5 nm increments with each row having a different multiplication factor combination for L2, L3, and L4 as seen in Table 15.

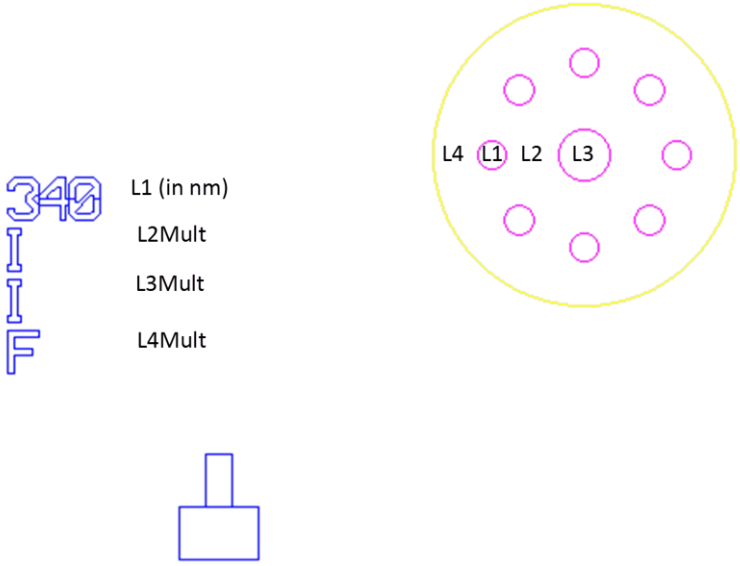

Figure 95: Phase wheel structure with alignment marks and label also showing the definitions of L1, L2, L3, and L4

Table 15: Rows of phase wheel structures on the test chip and their Y location relative to the bottom

L1Mult	*L2Mult*	*L3Mult*	*L4Mult*	*Y µm*
A (1X)	C (1.2X)	A (1X)	A (1X)	0
A (1X)	C (1.2X)	C (1.2X)	F (1.5X)	10
A (1X)	C (1.2X)	E (1.4X)	F (1.5X)	20
A (1X)	C (1.2X)	G(1.6X)	F (1.5X)	30
A (1X)	E (1.4X)	E (1.4X)	F (1.5X)	40
A (1X)	E (1.4X)	G(1.6X)	F (1.5X)	50
A (1X)	E (1.4X)	I (1.8X)	F (1.5X)	60
A (1X)	G(1.6X)	G(1.6X)	F (1.5X)	70
A (1X)	I (1.8X)	E (1.4X)	F (1.5X)	80
A (1X)	I (1.8X)	I (1.8X)	F (1.5X)	90

The dark boarder was created by including a sub-resolution checkerboard pattern. This checkerboard pattern puts the 1st diffraction order outside of the pupil and being a phase pattern with a 1:1 duty cycle, the 1st order destructively interferes with itself, creating a 'dark' image as seen in Figure 96, (a) showing a 32 nm pitch design and its image (b) with λ=13.5 nm, NA=0.3, and σ=0.3. This 'dark' pattern was placed everywhere on the test clip up to the target edge defined by the parameter L4.

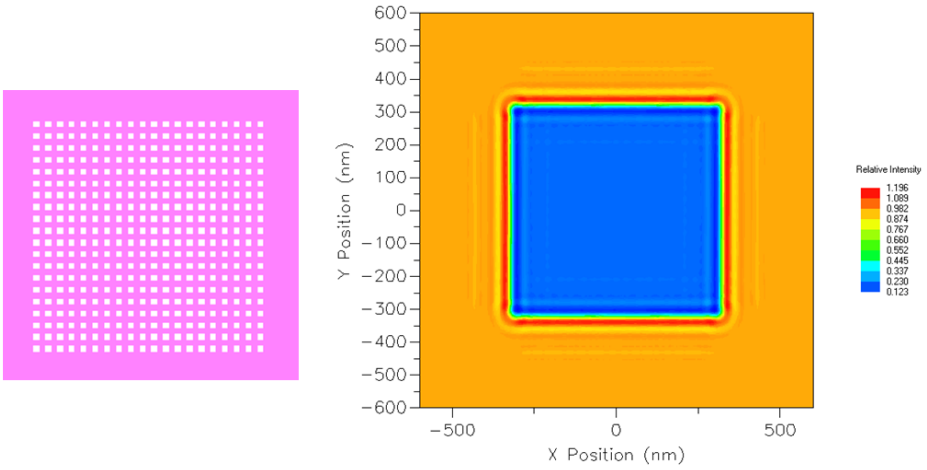

(a) (b)

Figure 96: Checkerboard pattern (a) design and (b) aerial image simulation with a pitch of 32 nm, λ=13.5 nm, NA=0.3, & σ=0.3

5.4 **Reticle Fabrication**

During the fabrication of the EUV phase shifting reticle, there was an etching bias (25 nm overetch) that caused features smaller than 50 nm (mask 5X) to be completely undercut and removed. This process bias prevented imaging of small phase targets as well as the 'dark' phase background made up of a sub-resolution checkerboard. The resulting background causes light to scatter in the system, reflecting most of the incoming radiation as seen in Figure 97. This can also be seen in Figure 98, which is a Transmission Electron Microscope (TEM) image of 50 nm lines showing their destruction post etch. The effect of a semi-transparent background is a reduction in contrast of the phase edges. Figure 99 shows a Transmission Electron Microscope (TEM) cross section image of the reticle. The image shows significant lateral etching. This can also be seen in the SEM top down image of the reticle, shown in Figure 100. The image shows lateral etching causing feature destruction.

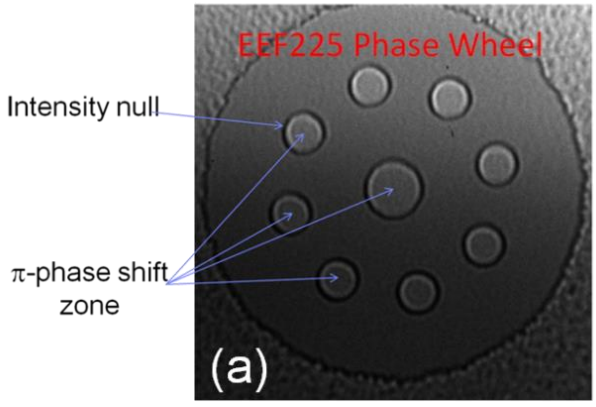

Figure 97: Actinic image of a phase wheel showing the semi-reflective background

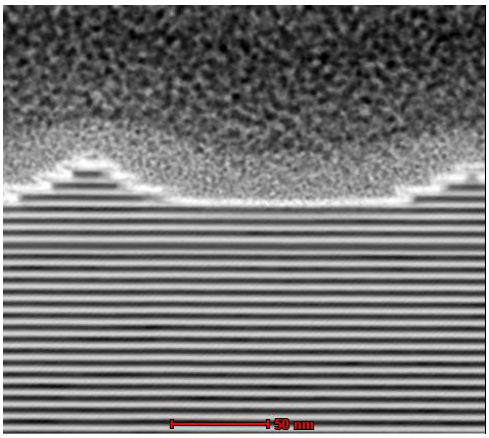

Figure 98: TEM image showing complete destruction of 50 nm lines post etch, courtesy of SEMATECH

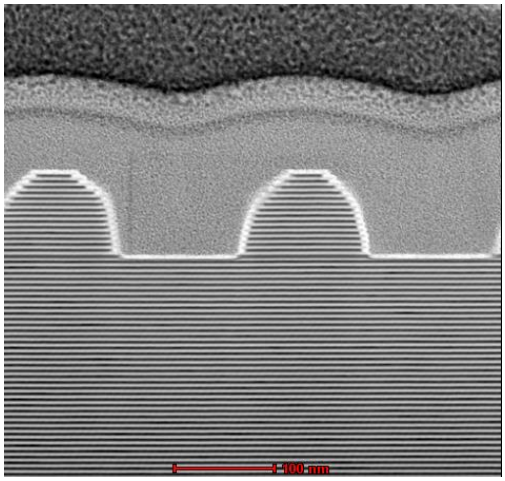

Figure 99: TEM cross section of the post etch PSM showing the rounding of a 100 nm feature, courtesy of SEMATECH

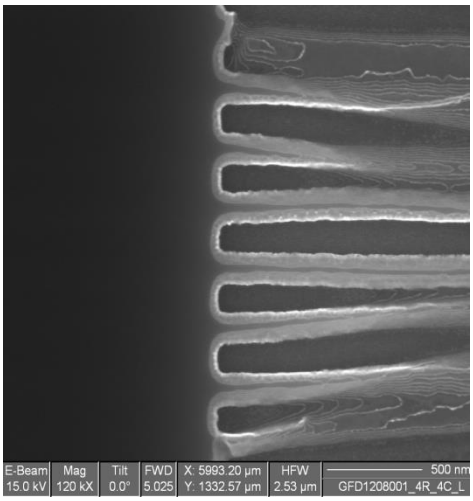

Figure 100: SEM top down image of 100 nm lines showing lateral etching and lift-off, courtesy of SEMATECH

5.5 **Experimental Validation**

Using the designed phase test patterns shown in Figure 91, data was collected using the SEMATECH Berkeley EUV Micro Exposure (MET) tool. The MET has an annular pupil with a central obscuration of 30% of the full pupil as well as mirror support structures as seen in Figure 101. The exposure field is 1 mm x 3 mm at the reticle plane (200 µm x 600 µm at wafer plane). The central obscuration reduces the effect of aberration on imaging, and therefore the sensitivity of image-based methods to extracting aberrations.

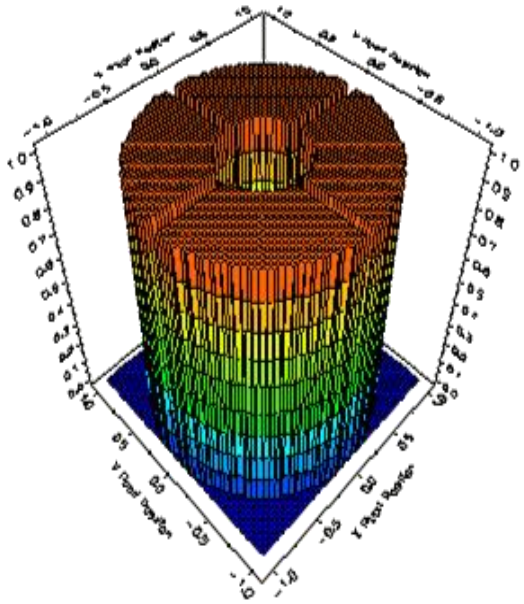

Figure 101: Transmission function of the pupil of the MET

Three test reticles have been manufactured by GLOBALFOUNDRIES, two with π phase shift and one with π/2 phase shift. There are two EUV MET tools in the United States, one at the University of California Berkeley and another at the University of Albany College of Nanoscale Science and Engineering (CNSE). The CNSE MET tool has an NA of 0.3 and limited illumination options, currently only allowing for dipole or quadrapole illumination with an inner sigma of 0.36 and outer sigma of 0.68. The Berkeley MET has a programmable illuminator, offering a range of different illuminations, including standard, monopole, dipole, quadrapole, and annular. The outer sigma of the programmable illuminator can go as high as 0.9 and the inner sigma has a practical limit of 0.1.

Several attempts were made to expose and obtain meaningful data from the Berkeley EUV MET with limited success. Since there is a central obscuration of 30% in

the pupil, an ideal on-axis small sigma illuminator would not give the desired image of phase edges. Ideally one phase edge would print as one line; however, since the un-diffracted light is being blocked, one phase edge printed as several trenches. Figure 102 shows an ideal aerial image of two phase edges from an isolated line, these would print as two resist lines for partial coherences of 0.1, 0.3 and 0.5. Figure 103 shows the same isolated phase shifted line printed with the MET 30% central obscuration shown in Figure 101. The resulting image would print as trenches for a partial coherence of 0.1 and 0.3, and will print as lines partial coherence values of 0.5 and 0.7. The obscuration blocks the undiffracted light (the background), so in a sense changing the tone from a bright field to a dark field. By using an illumination shape that has a larger radius than the obscuration, the field reverts back to bright field. In all cases the contrast is reduced compared to the non obscured case.

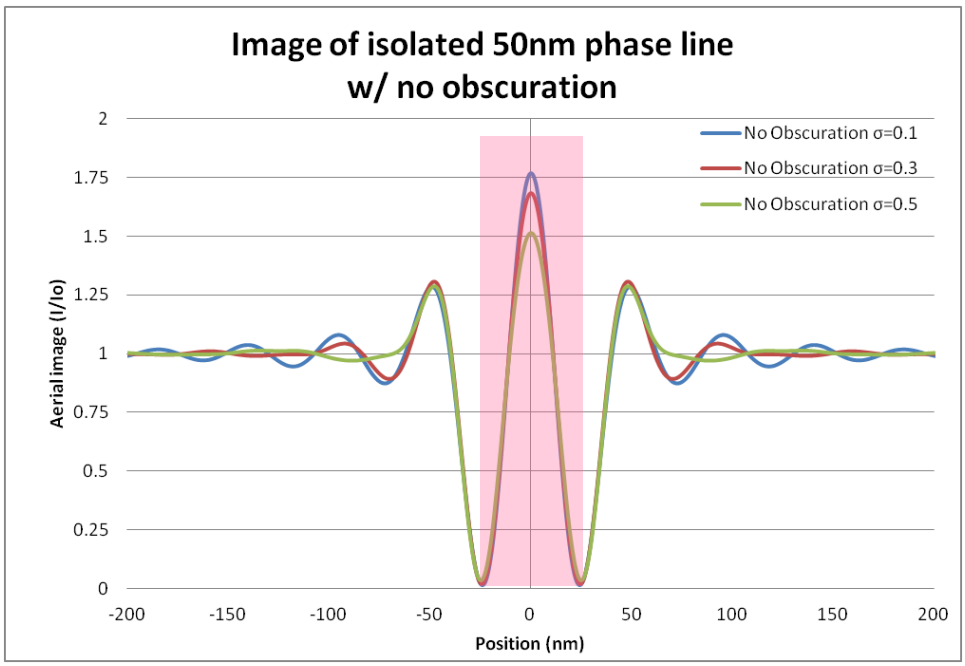

Figure 102: Image of 50nm isolated phase shifted line, two phase edges, with no pupil obscuration with varying partial coherence

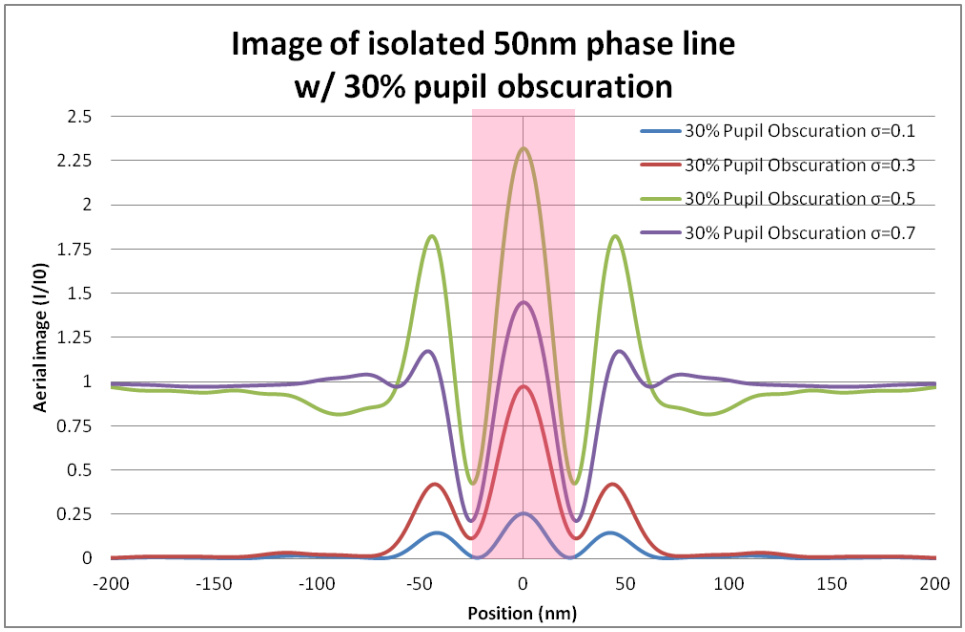

Figure 103: Aerial image of a 50nm isolated phase shifted line, two phase edges, with the MET 30% pupil obscuration

Another option that was considered was the use of monopole illumination. With a monopole a small partial coherence can be used with the limitations of an obscured pupil, gaining back the sensitivity that would be lost if a larger on-axis partial coherence was used. The results showed asymmetric printing through focus caused by the monopole. Figure 104 shows a 200 nm half pitch π phase shifted three bar structure through focus with a monopole with a sigma center (σ_c) of 0.4 and sigma radius (σ_r) of 0.1. Figure 105 shows the same but with the addition of a 30% central obscuration. In both it can be seen that there are asymmetric intensities from left to right with out-of-focus conditions. These asymmetric intensities can be accounted for if a reference of best focus is known. If a best focus reference is not known decoupling the effect of the monopole from aberrations becomes difficult as aberrations like coma will cause similar print artifacts. Figure 106 shows a SEM micrograph of a phase wheel having a L1=170 nm, L2=272 nm, L3=272 nm, and L4=255 nm, imaged with a σ_c=0.4 and σ_r=0.05 monopole. The results show an unknown focus state and asymmetric printing. Without knowledge of the focus condition it is difficult to determine aberrations using this method.

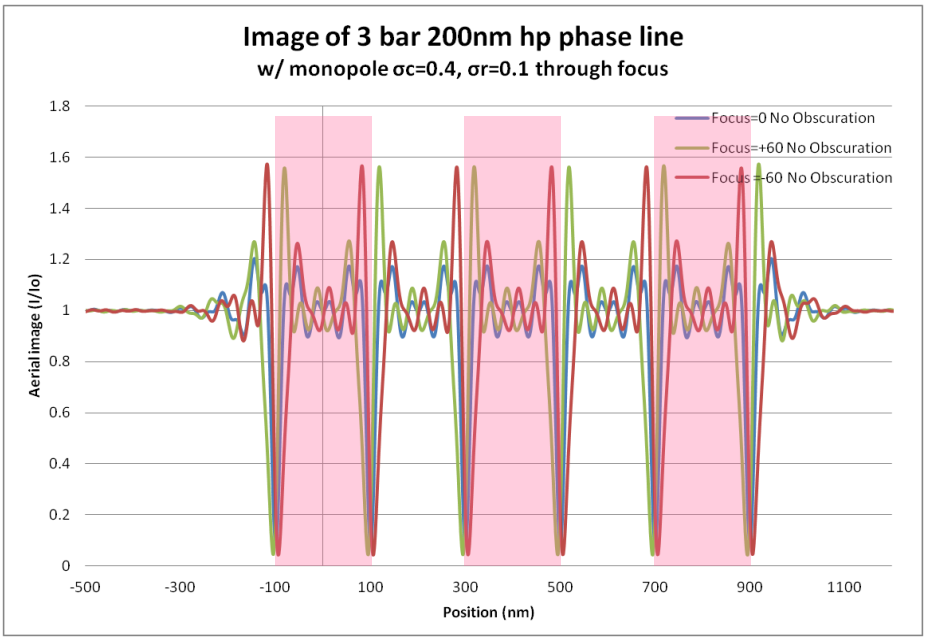

Figure 104: Aerial image of a phase shifted three bar structure with 200 nm half pitch, six π phase edges, imaged with a monopole with σ_c=0.4, and σ_r=0.1 through focus

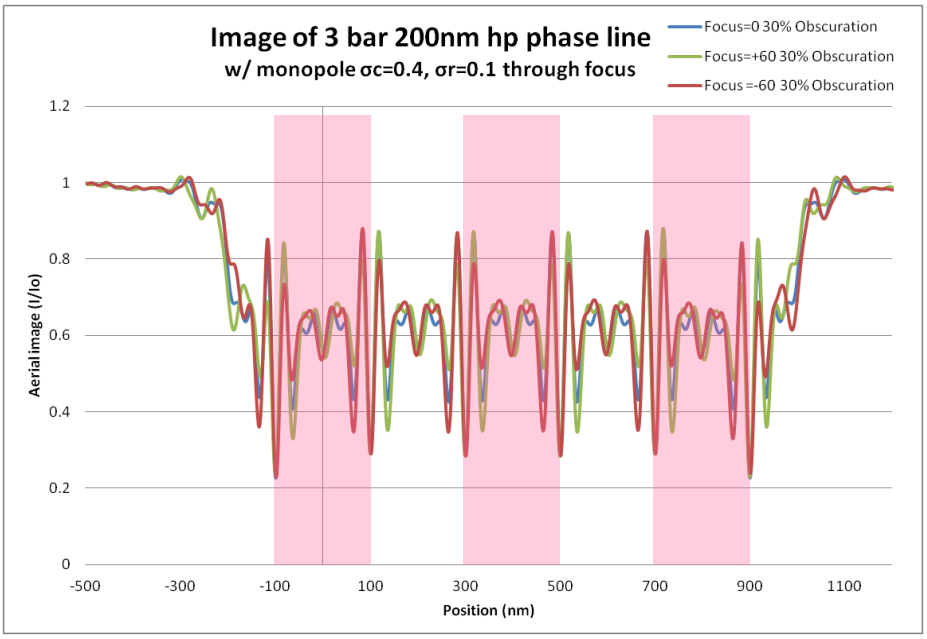

Figure 105: Aerial image of a three bar structure with 200 nm half pitch, six π phase edges, through focus with a 30% obscuration and monopole illumination σ_c=0.4, σ_r=0.1

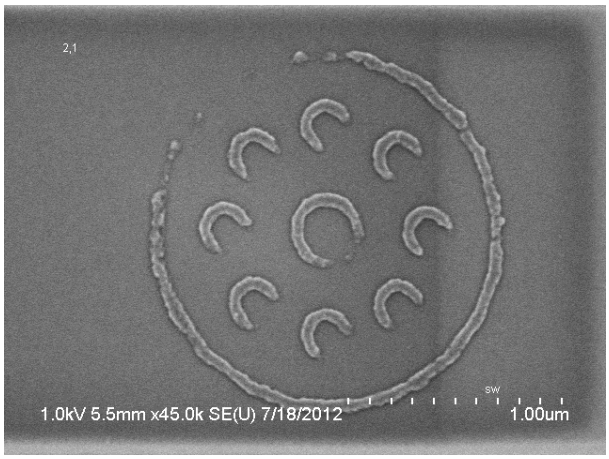

Figure 106: SEM micrograph of a phase wheel, L1=170 nm, L2=272 nm, L3=272 nm and L4=255 nm, imaged with a monopole with σ_c=0.4 and σ_r=0.05

Figure 107 show a SEM micrograph of an EUV resist image of a phase wheel with L1=235 nm, L2=376 nm, L3=376 nm, and L4=352 nm imaged with an on-axis standard illuminator having a partial coherence of 0.5. The image has much more resist scumming compared to Figure 106 due to the lower contrast. Imaging of features of interest with L1~50 nm was not possible due to this lower contract and possibly the effects of the black border around the phase wheels. It was therefore not possible to gather meaningful data with a large sigma standard illuminator.

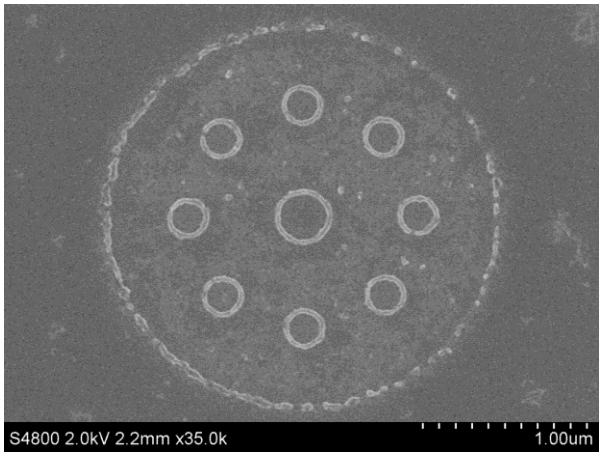

Figure 107: SEM micrograph of a phase wheel, L1=235 nm, L2=376 nm, L3=376 nm, and L4=352 nm

6. CONCLUSIONS

A complementary method to traditional approaches of determining and monitoring aberrations in EUVL systems has been shown. Image based aberration monitoring has a unique opportunity in EUVL. Due to tighter lens tolerances in absolute wavefront distortion and potential negative effects from heating, it may be necessary to monitor aberration levels during system use, something that is not possible using traditional methods. The absolute sensitivity of the presented method scales with wavelength and in terms of wavelength, wavefront distortion tolerances in EUVL compared to DUV (193 nm) lithography are much more relaxed, making an image based approach applicable for EUVL.

The presented method used one-dimensional and two-dimensional binary structures imaged in a partially coherent EUVL system in conjunction with computational modeling and simulation. It was successfully shown that the image based method can be used to monitor an aberration signature composed of primary as well as some higher order aberrations up to Z_{11}. The datasets were collected using three wafer exposures of specific test targets selected for the ASML alpha demo tool. It is believed that these three wafers can be further reduced to one wafer for periodic monitoring. It was also shown that the method is repeatable and sensitive to aberration change with a detection of an induced ~50 mλ change in astigmatism x, measuring 72 mλ.

A method of aberration extraction was shown that utilized a phase shifted structure that is capable of extracting aberrations up to Z_{36}. The method relies on CD

measurements of printed phase edges in conjunction with computational modeling and simulation. Several attempts of using phase structures with the Berkeley MET were investigated, yielding some promising images. It was however difficult to analyze the images that use a monopole illuminator due to the nature of the through focus behavior and no focus reference point. Another attempt was made utilizing an on axis 0.5 sigma partial coherence illumination, but due to poor process and effects of a light shield that was undercut during reticle fabrication, structures of interest (50 nm) did not print in photoresist.

7. REFERENCES

[1] G. E. Moore, "Cramming more components onto integrated circuits, Reprinted from Electronics, volume 38, number 8, April 19, 1965, pp.114 ff.," *IEEE Solid-State Circuits Society Newsletter* **11**(5), 33–35 (2006) [doi:10.1109/N-SSC.2006.4785860].

[2] "Intel 22nm 3-D Tri-Gate Transistor Technology," <http://newsroom.intel.com/docs/DOC-2032> (7 December 2011).

[3] "Intel Museum – The Intel 4004," <http://www.intel.com/about/companyinfo/museum/exhibits/4004/facts.htm> (7 December 2011).

[4] B. Smith, "Optics for Photolithography," in *Microlithography*, K. Suzuki and B. Smith, Eds., pp. 149–242, CRC Press (2007).

[5] Lord Rayleigh, "On the Theory of Optical Images, with special reference to the Microscope," *The London, Edinburgh, and Dublin Philosophical Magazine and Journal of Science* **42**(5), 167–195 (1896) [doi:10.1111/j.1365-2818.1903.tb04831.x].

[6] K. Ronse, P. De Bisschop, A. M. Goethals, J. Hermans, R. Jonckheere, S. Light, U. Okoroanyanwu, R. Watso, D. McAfferty, et al., "Status and critical challenges for 157-nm lithography," *Microelectron. Eng.* **73-74**(1), 5–10 (2004) [doi:10.1016/.mee.2004.02.007].

[7] B. W. Smith, A. Bourov, H. Kang, F. Cropanese, Y. Fan, N. Lafferty, and L. Zavyalova, "Water immersion optical lithography at 193 nm," *Journal of Microlithography, Microfabrication, and Microsystems* **3**(1), 44–51 (2004) [doi:doi:10.1117/1.1637594].

[8] P. A. Zimmerman, B. J. Rice, E. C. Piscani, and V. Liberman, "High index 193 nm immersion lithography: the beginning or the end of the road," 727420–727420 (2009) [doi:10.1117/12.814381].

[9] K. Kamon, T. Miyamoto, Y. Myoi, H. Nagata, N. Kotani, and M. Tanaka, "Photolithography System Using a Combination of Modified Illumination and Phase Shift Mask," *Japanese Journal of Applied Physics* **31**(Part 1, No. 12B), 4131–4136 (1992) [doi:10.1143/JJAP.31.4131].

[10] J. Garofalo, C. J. Biddick, R. L. Kostelak, and S. Vaidya, "Mask assisted off-axis illumination technique for random logic," in *Proceedings of the 16th international symposium on electron, ion, and photon beams* **11**, pp. 2651–2658, AVS (1993) [doi:10.1116/1.586579].

[11] M. D. Levenson, N. S. Viswanathan, and R. A. Simpson, "Improving resolution in photolithography with a phase-shifting mask," *Electron Devices, IEEE Transactions on* **29**(12), 1828 – 1836 (1982) [doi:10.1109/T-ED.1982.21037].

[12] A. E. Rosenbluth, S. Bukofsky, C. Fonseca, M. Hibbs, K. Lai, A. F. Molless, R. N. Singh, and A. K. K. Wong, "Optimum mask and source patterns to print a given shape," *J. Micro/Nanolith. MEMS MOEMS* **1**(1), 13–30 (2002) [doi:10.1117/1.1448500].

[13] B. W. Smith, L. V. Zavyalova, and A. Estroff, “Benefiting from polarization effects on high-NA imaging,” 68–79 (2004) [doi:10.1117/12.537266].
[14] “ITRS Reports,” *International Technology Roadmap for Semiconductors*, <http://public.itrs.net/reports.html> (18 January 2012).
[15] B. J. Lin, “Deep UV lithography,” *Journal of Vacuum Science and Technology* **12**(6), 1317–1320 (1975) [doi:10.1116/1.568527].
[16] J. J. Ewing, “Rare-gas halide lasers,” *Physics Today* **31**(5), 32–39 (1978) [doi:10.1063/1.2995036].
[17] J. J. Ewing and C. A. Brau, “Laser action on the 2Σ+1/2→2Σ+1/2 bands of KrF and XeCl,” *Applied Physics Letters* **27**(6), 350–352 (1975) [doi:doi:10.1063/1.88473].
[18] K. Jain, C. G. Willson, and B. J. Lin, “Ultrafast deep UV Lithography with excimer lasers,” *IEEE Electron Device Letters* **3**(3), 53 – 55 (1982) [doi:10.1109/EDL.1982.25476].
[19] D. Basting, K. D. Pippert, and U. Stamm, “History and future prospects of excimer lasers,” 25–34 (2002) [doi:10.1117/12.456812].
[20] J. Fujimoto, T. Abe, S. Tanaka, T. Ohta, T. Hori, T. Yanagida, H. Nakarai, and H. Mizoguchi, “Laser-produced plasma-based extreme-ultraviolet light source technology for high-volume manufacturing extreme-ultraviolet lithography,” *J. Micro/Nanolith. MEMS MOEMS* **11**(2), 021111–1 (2012) [doi:10.1117/1.JMM.11.2.021111].
[21] I. V. Fomenkov, B. La Fontaine, D. Brown, I. Ahmad, P. Baumgart, N. R. Böwering, D. C. Brandt, A. N. Bykanov, S. De Dea, et al., “Development of stable extreme-ultraviolet sources for use in lithography exposure systems,” *J. Micro/Nanolith. MEMS MOEMS* **11**(2), 021110–021111 (2012) [doi:10.1117/1.JMM.11.2.021110].
[22] V. G. Novikov, V. V. Ivanov, K. N. Koshelev, V. M. Krivtsun, and A. D. Solomyannaya, “Calculation of tin emission spectra in discharge plasma: The influence of reabsorption in spectral lines,” *High Energy Density Physics* **3**(1–2), 198–203 (2007) [doi:10.1016/j.hedp.2007.02.014].
[23] D. A. Tichenor, G. D. Kubiak, M. E. Malinowski, R. H. Stulen, S. J. Haney, K. W. Berger, R. P. Nissen, R. L. Schmitt, G. A. Wilkerson, et al., “Application of laser plasma sources in soft x-ray projection lithography,” 104–112 (1994) [doi:10.1117/12.167986].
[24] J. Mulkens, J. de Klerk, M. Leenders, F. de Jong, and J. W. Cromwijk, “Latest developments on immersion exposure systems,” 2008, 69241P–69241P–12 [doi:10.1117/12.774958].
[25] H. Meiling, W. de Boeij, F. Bornebroek, N. Harned, I. de Jong, P. Kűrz, M. Lowisch, H. Meijer, D. Ockwell, et al., “From performance validation to volume introduction of ASML’s NXE platform,” 83221G–83221G (2012) [doi:10.1117/12.916971].
[26] “EUVA official Web site / Technical Information - EUV Light Source and Exposure Tool,” <http://www.euva.or.jp/technical_info/tool.html> (18 January 2012).

[27] H. Ito, “Rise of chemical amplification resists from laboratory curiosity to paradigm enabling Moore’s law,” 692302–692302 (2008) [doi:10.1117/12.782636].
[28] T. Kozawa and S. Tagawa, “Theoretical Study on Difference between Image Quality Formed in Low- and High-Activation-Energy Chemically Amplified Resists,” *Applied Physics Express* **1**(10), 107001 (2008) [doi:10.1143/APEX.1.107001].
[29] T. Kozawa and S. Tagawa, “Radiation Chemistry in Chemically Amplified Resists,” *Japanese Journal of Applied Physics* **49**(3), 030001 (2010) [doi:10.1143/JJAP.49.030001].
[30] W. D. Hinsberg, F. A. Houle, M. I. Sanchez, J. A. Hoffnagle, G. M. Wallraff, D. R. Medeiros, G. M. Gallatin, and J. L. Cobb, “Extendibility of chemically amplified resists: another brick wall?,” 1–14 (2003) [doi:10.1117/12.487739].
[31] F. Scholze, J. Tümmler, E. Gullikson, and A. Aquila, “Comparison of extreme ultraviolet reflectance measurements,” *Journal of Microlithography, Microfabrication, and Microsystems* **2**(3), 233 (2003) [doi:10.1117/1.1583735].
[32] O. Kritsun, B. La Fontaine, Y. Hao, J. Li, O. Wood, S. Raghunathan, T. Brunner, C. Koay, and H. Mizuno, “Characterization of a 0.25NA full-field EUV exposure tool,” 727121–727121 (2009) [doi:10.1117/12.816545].
[33] D. M. Tennant, J. E. Bjorkholm, L. Eichner, R. R. Freeman, T. E. Jewell, A. A. MacDowell, J. Z. Pastalan, L. H. Szeto, W. K. Waskiewicz, et al., “Comparison of reflective mask technologies for soft x-ray projection lithography,” 91–104 (1992) [doi:10.1117/12.56938].
[34] B. La Fontaine, A. R. Pawloski, Y. Deng, C. Chovino, L. Dieu, O. R. Wood II, and H. J. Levinson, “Architectural choices for EUV lithography masks: patterned absorbers and patterned reflectors,” 300–310 (2004) [doi:10.1117/12.539074].
[35] S. B. Hill, I. Ermanoski, S. Grantham, C. Tarrio, T. B. Lucatorto, T. E. Madey, S. Bajt, M. Chandhok, P. Yan, et al., “EUV testing of multilayer mirrors: critical issues,” 61510F–61510F (2006) [doi:10.1117/12.656502].
[36] K. Murakami, T. Oshino, H. Kondo, H. Chiba, Y. Kawabe, T. Ono, N. Kandaka, A. Yamazaki, T. Yamaguchi, et al., “Development of EUV lithography tool technologies at Nikon,” 2012, 832215–832215–9 [doi:10.1117/12.917676].
[37] Y. D. Chan, “EUV mask readiness and challenges for the 22nm half pitch and beyond,” *Proceedings of SPIE* **7985**(1), 79850A–79850A–7 (2011) [doi:doi:10.1117/12.896913].
[38] R. Jonckheere, G. F. Lorusso, A. Goethals, K. Ronse, J. Hermans, and R. De Ruyter, “Assessment of EUV reticle blank availability enabling the use of EUV tools today and in the future,” *Proceedings of SPIE* **6533**(1), 653313–653313–12 (2007) [doi:doi:10.1117/12.737179].
[39] A. Tchikoulaeva, U. Okoroanyanwu, O. Wood, B. La Fontaine, C. Holfeld, S. Kini, M. Peikert, C. Boye, C.-S. Koay, et al., “EUVL reticle defectivity evaluation,” *Proceedings of SPIE* **7271**(1), 727117–727117–8 (2009) [doi:doi:10.1117/12.815525].
[40] J. Moon, C.-K. Kim, B.-S. Nam, B.-H. Nam, Y.-S. Hyun, S.-K. Kim, C.-M. Lim, Y.-D. Kim, M.-S. Kim, et al., “Evaluation of shadowing and flare effect for EUV

tool," *Proceedings of SPIE* **7271**(1), 727144–727144–10 (2009) [doi:doi:10.1117/12.814364].
[41] R. Jonckheere, D. Van den Heuvel, T. Bret, T. Hofmann, J. Magana, I. Aharonson, D. Meshulach, E. Hendrickx, and K. Ronse, "Evidence of printing blank-related defects on EUV masks missed by blank inspection," *Proceedings of SPIE* **7985**(1), 79850W–79850W–10 (2011) [doi:doi:10.1117/12.883854].
[42] G. F. Lorusso, F. Van Roey, E. Hendrickx, G. Fenger, M. Lam, C. Zuniga, M. Habib, H. Diab, and J. Word, "Flare in extreme ultraviolet lithography: metrology, out-of-band radiation, fractal point-spread function, and flare map calibration," *Journal of Micro/Nanolithography, MEMS and MOEMS* **8**(4), 041505–041505–6 (2009) [doi:doi:10.1117/1.3238515].
[43] B. La Fontaine, A. R. Pawloski, O. Wood, Y. Deng, H. J. Levinson, P. Naulleau, P. E. Denham, E. Gullikson, B. Hoef, et al., "Demonstration of phase-shift masks for extreme-ultraviolet lithography," *Proceedings of SPIE* **6151**(1), 61510A–61510A–8 (2006) [doi:doi:10.1117/12.652212].
[44] H.-K. Cho and J. Ahn, "EUV Mask and Mask Metrology," in *EUV lithography*, V. Bakshi, Ed., pp. 325–382, SPIE Press ; John Wiley, Bellingham, Wash.; Hoboken, NJ (2009).
[45] K. A. Goldberg, "EUV Optical Testing," in *EUV lithography*, V. Bakshi, Ed., pp. 205–226, SPIE Press ; John Wiley, Bellingham, Wash.; Hoboken, NJ (2009).
[46] C. Gwyn and S. Wurm, "EUV Lithography," in *Microlithography*, K. Suzuki and B. Smith, Eds., pp. 383–464, CRC Press (2007).
[47] R. Soufli, S. Bajt, R. M. Hudyma, and J. S. Taylor, "Optics and Multilayer Coatings for EUVL Systems," in *EUV lithography*, V. Bakshi, Ed., pp. 135–160, SPIE Press ; John Wiley, Bellingham, Wash.; Hoboken, NJ (2009).
[48] R. Soufli, R. M. Hudyma, E. Spiller, E. M. Gullikson, M. A. Schmidt, J. C. Robinson, S. L. Baker, C. C. Walton, and J. S. Taylor, "Sub-diffraction-limited multilayer coatings for the 0.3 numerical aperture micro-exposure tool for extreme ultraviolet lithography," *Appl. Opt.* **46**(18), 3736–3746 (2007) [doi:10.1364/AO.46.003736].
[49] H. Kinoshita and O. Wood, "EUV Lithography: An Hitoric Perspective," in *EUV lithography*, V. Bakshi, Ed., pp. 1 – 54, SPIE Press ; John Wiley, Bellingham, Wash.; Hoboken, NJ (2009).
[50] H. Mizuno, G. McIntyre, C. Koay, M. Burkhardt, B. La Fontaine, and O. Wood, "Flare evaluation of ASML alpha demo tool," 72710U–72710U (2009) [doi:10.1117/12.814312].
[51] G. L. Fenger, G. F. Lorusso, E. Hendrickx, and A. Niroomand, "Design correction in extreme ultraviolet lithography," *Journal of Micro/Nanolithography, MEMS and MOEMS* **9**(4), 043001–043001–8 (2010) [doi:doi:10.1117/1.3496030].
[52] S. Raghunathan, G. McIntyre, G. Fenger, and O. Wood, "Mask 3D effects and compensation for high NA EUV lithography," 867918–867918 (2013) [doi:10.1117/12.2011643].
[53] J. Bernoulli, *Jacobi Bernoulli ... Ars conjectandi, opus posthumum. Accedit Tractatus de seriebus infinitis, et epistola gallicé scripta de ludo pilae reticularis.*, impensis Thurnisiorum, fratrum, Basileae (1713).

[54] S.-D. Poisson, *Recherches sur la probabilité des jugements en matière criminelle et en matière civile: précédées des règles générales du calcul des probabilités*, Bachelier (1837).
[55] D. M. Williamson, "The Elusive Diffraction Limit," in *Extreme Ultraviolet Lithography* **23**, pp. 68–76, OSA (1994).
[56] O. R. Wood II, D. Back, R. Brainard, G. Denbeaux, D. Goldfarb, F. Goodwin, J. Hartley, K. Kimmel, C. Koay, et al., "Initial experience establishing an EUV baseline lithography process for manufacturability assessment," 65170U–65170U (2007) [doi:10.1117/12.714016].
[57] O. Wood, J. Arnold, T. Brunner, M. Burkhardt, J. H.-C. Chen, D. Civay, S. S.-C. Fan, E. Gallagher, S. Halle, et al., "Insertion strategy for EUV lithography," 832203–832203 (2012) [doi:10.1117/12.916292].
[58] P. Dirksen, C. A. H. Juffermans, A. Engelen, P. De Bisschop, and H. Muellerke, "Impact of high-order aberrations on the performance of the aberration monitor," *Proceedings of SPIE* **4000**(1), 9–17 (2000) [doi:doi:10.1117/12.389010].
[59] M. H. P. Moers, H. van der Laan, M. Zellenrath, W. de Boeij, N. A. Beaudry, K. D. Cummings, A. van Zwol, A. Brecht, and R. Willekers, "Application of the aberration ring test (ARTEMIS) to determine lens quality and predict its lithographic performance," *Proceedings of SPIE* **4346**(1), 1379–1387 (2001) [doi:doi:10.1117/12.435676].
[60] L. Zavyalova, "Measuring Aberrations in Lithographic projection Systems with Phase Wheel Targets," Rochester Institute of Technology (2010).
[61] N. R. Farrar, A. H. Smith, D. R. Busath, and D. Taitano, "In-situ measurement of lens aberrations," *Proceedings of SPIE* **4000**(1), 18–29 (2000) [doi:doi:10.1117/12.389021].
[62] H. Nomura and T. Sato, "Techniques for Measuring Aberrations in Lenses Used in Photolithography with Printed Patterns," *Appl. Opt.* **38**(13), 2800–2807 (1999) [doi:10.1364/AO.38.002800].
[63] E. L. Raab, C. Pierrat, C. H. Fields, R. L. Kostelak, W. G. Oldham, and S. Vaidya, "Analyzing deep-UV lens aberrations using aerial image and latent image metrologies," *Proceedings of SPIE* **2197**(1), 550–565 (1994) [doi:doi:10.1117/12.175450].
[64] B. W. Smith, "Variations to the influence of lens aberration invoked with PSM and OAI," *Proceedings of SPIE* **3679**(1), 330–346 (1999) [doi:doi:10.1117/12.354346].
[65] B. W. Smith and R. E. Schlief, "Understanding lens aberration and influences to lithographic imaging," *Proceedings of SPIE* **4000**(1), 294–306 (2000) [doi:doi:10.1117/12.389018].
[66] B. W. Smith, "Method for aberration detection and measurement," 7136143 (2006).
[67] B. W. Smith, "Apparatus for aberration detection and measurement," 7345735 (2008).
[68] B. W. Smith, "Method for aberration evaluation in a projection system," 7768648 (2010).
[69] K. van Ingen Schenau, H. Bakker, M. Zellenrath, R. Moerman, J. Linders, T. Rohe, and W. Emer, "System qualification and optimization for imaging

performance on the 0.80-NA 248-nm step-and-scan systems," *Proceedings of SPIE* **4691**(1), 637–651 (2002) [doi:doi:10.1117/12.474612].
[70] P. Venkataraman and B. W. Smith, "Aberrations of steppers using phase-shifting point diffraction interferometry," *Proceedings of SPIE* **4000**(1), 1245–1249 (2000) [doi:doi:10.1117/12.388962].
[71] L. Zavyalova, A. Bourov, and B. W. Smith, "Automated aberration extraction using phase wheel targets," *Proceedings of SPIE* **5754**(1), 1728–1737 (2005) [doi:doi:10.1117/12.606460].
[72] J. B. van Schoot, N. Seong, B. Geh, M. Burkhardt, P. Graeupner, G. Reisinger, R. Rubingh, M. Suddendorf, J. Finders, et al., "Printing 130-nm DRAM isolation pattern: Zernike correlation and tool improvement," 229–240 (2001) [doi:10.1117/12.435723].
[73] F. Wang, X. Wang, and M. Ma, "Measurement technique for in situ characterizing aberrations of projection optics in lithographic tools," *Appl. Opt.* **45**(24), 6086–6093 (2006) [doi:10.1364/AO.45.006086].
[74] C. G. Krautschik, M. Ito, I. Nishiyama, and T. Mori, "Quantifying EUV imaging tolerances for the 70-, 50-, 35-nm modes through rigorous aerial image simulations," *Proceedings of SPIE* **4343**(1), 524–534 (2001) [doi:doi:10.1117/12.436684].
[75] S. H. Lee, Y. Shroff, and M. Chandhok, "Flare and lens aberration requirements for EUV lithographic tools," *Proceedings of SPIE* **5751**(1), 707–714 (2005) [doi:doi:10.1117/12.604870].
[76] J. Whang, M. Chandrachood, E. Gallagher, T. Faure, M. Grimbergen, S. Crawford, K. Yu, T. Y. . B. Leung, R. Wistrom, et al., "Dry etching performance of advanced EUV mask blanks," *Proceedings of SPIE* **8166**(1), 81661W–81661W–6 (2011) [doi:doi:10.1117/12.898815].
[77] T. Shoki, M. Hosoya, T. Kinoshita, H. Kobayashi, Y. Usui, R. Ohkubo, S. Ishibashi, and O. Nagarekawa, "Process development of 6-in EUV mask with TaBN absorber," *Proceedings of SPIE* **4754**(1), 857–864 (2002) [doi:doi:10.1117/12.477007].
[78] P. Yan, G. Zhang, A. Ma, and T. Liang, "TaN EUVL mask fabrication and characterization," *Proceedings of SPIE* **4343**(1), 409–414 (2001) [doi:doi:10.1117/12.436668].
[79] R. Seltmann, A. M. Minvielle, C. A. Spence, S. Muehle, L. Capodieci, and K. B. Nguyen, "CD uniformity consideration for DUV step and scan tools," *Proceedings of SPIE* **3679**(1), 239–249 (1999) [doi:doi:10.1117/12.354337].
[80] J. Vasek, C.-C. Fu, and G. Chen, "Phase-shift reticle design impact on patterned linewidth variation and LWR," *Proceedings of SPIE* **6349**(1), 63491S–63491S–9 (2006) [doi:doi:10.1117/12.686594].
[81] D. Hibino, H. Shindo, Y. Abe, Y. Hojyo, G. Fenger, T. Do, I. Kusnadi, J. L. Sturtevant, J. Van de Kerkhove, et al., "High-accuracy optical proximity correction modeling using advanced critical dimension scanning electron microscope–based contours in next-generation lithography," *Journal of Micro/Nanolithography, MEMS and MOEMS* **10**(1), 013012–013012–8 (2011) [doi:doi:10.1117/1.3530082].

[82] H. Wolter, “Optik dünner Schichten,” *Encyclopedia of Physics* **24**, 461–554 (1956).
[83] F. Zernike, “Beugungstheorie des schneidenver-fahrens und seiner verbesserten form, der phasenkontrastmethode,” *Physica* **1**(7–12), 689–704 (1934) [doi:10.1016/S0031-8914(34)80259-5].
[84] D. Malacara, *Optical Shop Testing*, John Wiley & Sons, New York [etc.] (1992).
[85] A. K. Wong and A. R. Neureuther, “Mask topography effects in projection printing of phase-shifting masks,” *Electron Devices, IEEE Transactions on* **41**(6), 895 –902 (1994) [doi:10.1109/16.293299].
[86] B. J. Lin, “The attenuated phase-shifting mask,” *Solid State Technology* **35**(1), 43–47 (1992).
[87] B. W. Smith, “Attenuated phase shift mask and a method for making the mask,” 6309780 (2001).
[88] B. W. Smith, “Multi-layered attenuated phase shift mask and a method for making the mask,” 5939227 (1999).
[89] Y.-C. Ku, E. H. Anderson, M. L. Schattenburg, and H. I. Smith, “Use of a pi-phase shifting x-ray mask to increase the intensity slope at feature edges,” *Journal of Vacuum Science & Technology B: Microelectronics and Nanometer Structures* **6**(1), 150–153 (1988) [doi:10.1116/1.584034].
[90] B. W. Smith, “Apparatus and method for phase shift photomasking,” 6480263 (2002).
[91] J. W. Goodman, “Wave-Optics Analysis of Coherent Optical Systems,” in *Introduction to Fourier Optics*, pp. 96–125, McGraw-Hill, New York (1996).
[92] K. Strehl, “Aplanatische und fehlerhafte Abbildung im Fernrohr,” *Zeitschrift für Instrumentenkunde* **15**, 362–370 (1895).
[93] K. Strehl, “Über Luftschlieren und Zonenfehler,” *Zeitschrift für Instrumentenkunde* **22**, 213–217 (1902).
[94] A. B. Bhatia and E. Wolf, “On the circle polynomials of Zernike and related orthogonal sets,” *Mathematical Proceedings of the Cambridge Philosophical Society* **50**(01), 40–48 (1954) [doi:10.1017/S0305004100029066].
[95] M. Born and E. Wolf, “The diffraction theory of aberrations,” in *Principles of optics*, 7th ed., pp. 464–468, Cambridge Univ. Press, Cambridge (1999).
[96] J. S. Loomis, “Analysis Of Interferograms From Waxicons,” 64–69 (1979) [doi:10.1117/12.957046].
[97] V. N. Mahajan, “Zernike annular polynomials for imaging systems with annular pupils,” *J. Opt. Soc. Am.* **71**(1), 75–85 (1981) [doi:10.1364/JOSA.71.000075].
[98] V. N. Mahajan, “Zernike Annular Polynomials and Optical Aberrations of Systems with Annular Pupils,” *Appl. Opt.* **33**(34), 8125–8127 (1994) [doi:10.1364/AO.33.008125].
[99] B. W. Smith and J. S. Petersen, “Influences of off-axis illumination on optical lens aberration,” in *Papers from the 42nd international conference on electron, ion, and photon beam technology and nanofabrication* **16**, pp. 3405–3410, AVS (1998) [doi:10.1116/1.590467].
[100] W. P. Linnik, “A simple interferometer for the investigation of optical systems,” *Proc. Academy of Sci. of the USSR* **1**, 208 (1933).

[101] J. M. Burch, “Scatter Fringes of Equal Thickness,” , *Published online: 16 May 1953; | doi:10.1038/171889a0* **171**(4359), 889–890 (1953) [doi:10.1038/171889a0].
[102] H. Medecki, E. Tejnil, K. A. Goldberg, and J. Bokor, “Phase-shifting point diffraction interferometer,” *Opt. Lett.* **21**(19), 1526 (1996) [doi:10.1364/OL.21.001526].
[103] P. P. Naulleau, K. A. Goldberg, S. H. Lee, C.-H. C. Chang, C. J. Bresloff, P. J. Batson, J. Attwood, and J. Bokor, “Characterization of the accuracy of EUV phase-shifting point diffraction interferometry,” *Proceedings of SPIE* **3331**(1), 114–123 (1998) [doi:doi:10.1117/12.309563].
[104] P. P. Naulleau, K. A. Goldberg, and J. Bokor, “Extreme ultraviolet carrier-frequency shearing interferometry of a lithographic four-mirror optical system,” *J. Vac. Sci. Technol. B* **18**(6), 2939 (2000) [doi:10.1116/1.1321290].
[105] L. Foucault, “Description des procedees employes pour reconnaitre la configuration des surfaces optiques,” *C. R. Acad. Sci.* **47**, 958ff (1858).
[106] J. Hartmann, “Objektivuntersuchungen.,” *Zt. Instrumentenkd* **24**, 1 (1904).
[107] D. Malacara-Doblado and I. Ghozeil, “Hartmann, Hartmann–Shack, and Other Screen Tests,” in *Optical Shop Testing*, D. Malacara, Ed., pp. 361–397, John Wiley & Sons, Inc., Hoboken, NJ, USA.
[108] V. Ronchi, “Le frange di combinazioni nello studio delle superficie e dei sistemi ottici,” *Rivista d’Ottica e Meccanica di precisione* **2**, 9–35 (1923).
[109] J. P. Kirk, “Review of photoresist-based lens evaluation methods,” 2–8 (2000) [doi:10.1117/12.388926].
[110] M. Banyay, S. Brose, and L. Juschkin, “Line image sensors for spectroscopic applications in the extreme ultraviolet,” *Meas. Sci. Technol.* **20**(10), 105201 (2009) [doi:10.1088/0957-0233/20/10/105201].
[111] M. G. Moharam and T. K. Gaylord, “Rigorous coupled-wave analysis of planar-grating diffraction,” *J. Opt. Soc. Am.* **71**(7), 811–818 (1981) [doi:10.1364/JOSA.71.000811].
[112] J. C. Maxwell, “A Dynamical Theory of the Electromagnetic Field,” *Philosophical Transactions of the Royal Society of London* **155**, 459–512 (1865).
[113] H. H. Hopkins, “On the Diffraction Theory of Optical Images,” *Proceedings of the Royal Society of London. Series A, Mathematical and Physical Sciences* **217**(1130), 408–432 (1953).
[114] H. H. Hopkins, “The Concept of Partial Coherence in Optics,” *Proceedings of the Royal Society of London. Series A, Mathematical and Physical Sciences* **208**(1093), 263–277 (1951).
[115] H. H. Hopkins, “The Frequency Response of a Defocused Optical System,” *Proceedings of the Royal Society of London. Series A, Mathematical and Physical Sciences* **231**(1184), 91–103 (1955).
[116] T. A. Brunner, A. L. Martin, R. M. Martino, C. P. Ausschnitt, T. H. Newman, and M. S. Hibbs, “Quantitative stepper metrology using the focus monitor test mask,” *Proceedings of SPIE* **2197**(1), 541–549 (1994) [doi:doi:10.1117/12.175449].
[117] J. P. Kirk and C. J. Progler, “Application of blazed gratings for determination of equivalent primary azimuthal aberrations,” *Proceedings of SPIE* **3679**(1), 70–76 (1999) [doi:doi:10.1117/12.354375].

[118] H. Schreiber and J. H. Bruning, “Phase Shifting Interferometry,” in *Optical Shop Testing*, D. Malacara, Ed., pp. 547–666, John Wiley & Sons, Inc., Hoboken, NJ, USA.

[119] M. A. van de Kerkhof, W. de Boeij, H. Kok, M. Silova, J. Baselmans, and M. Hemerik, “Full optical column characterization of DUV lithographic projection tools,” *Proceedings of SPIE* **5377**(1), 1960–1970 (2004) [doi:doi:10.1117/12.536331].

[120] P. P. Naulleau, K. A. Goldberg, S. H. Lee, C. Chang, D. Attwood, and J. Bokor, “Extreme-ultraviolet phase-shifting point-diffraction interferometer: a wave-front metrology tool with subangstrom reference-wave accuracy,” *Appl. Opt.* **38**(35), 7252–7263 (1999) [doi:10.1364/AO.38.007252].

[121] K. A. Goldberg, P. Naulleau, J. Bokor, H. N. Chapman, and A. Barty, “Testing extreme ultraviolet optics with visible-light and extreme ultraviolet interferometry,” *Papers from the 46th International Conference on Electron, Ion, and Photon Beam Technology and Nanofabrication* **20**, 2834–2839 (2002) [doi:10.1116/1.1523401].

[122] W. N. Partlo, C. H. Fields, and W. G. Oldham, “Direct aerial image measurement as a method of testing high numerical aperture microlithographic lenses,” in *Proceedings of the 16th international symposium on electron, ion, and photon beams* **11**, pp. 2686–2691, AVS, San Diego, California (USA) (1993) [doi:10.1116/1.586585].

[123] D. G. Flagello, J. de Klerk, G. Davies, R. Rogoff, B. Geh, M. Arnz, U. Wegmann, and M. Kraemer, “Toward a comprehensive control of full-field image quality in optical photolithography,” *Proceedings of SPIE* **3051**(1), 672–685 (1997) [doi:doi:10.1117/12.275987].

[124] Spiricon, “Hartmann Wavefront Analyzer Tutorial,” Spiricon Inc (2004).

[125] A. H. Smith, B. B. McArthur, R. O. Hunter, and Jr, “Apparatus method of measurement and method of data analysis for correction of optical system,” 5978085 (1999).

[126] K. Kaise, T. Tsukakoshi, and T. Hayashi, “Method for the measurement of aberration of optical projection system,” 6296977 (2001).

[127] M. S. Yeung, “Measurement of wave-front aberrations in high-resolution optical lithographic systems from printed photoresist patterns,” *Semiconductor Manufacturing, IEEE Transactions on* **13**(1), 24 –33 (2000) [doi:10.1109/66.827337].

[128] L. Sun, S. Raghunathan, V. Jindal, E. Gullikson, P. Mangat, I. Mochi, K. A. Goldberg, M. P. Benk, O. Kritsun, et al., “Application of phase shift focus monitor in EUVL process control,” 86790T–86790T (2013) [doi:10.1117/12.2011342].

[129] A. R. Neureuther, K. Adam, G. C. Robins, and F. E. Gennari, “Characterizing aberrations in an imaging lens and applications to visual testing and integrated circuit mask analysis,” 7030997 (2006).

[130] C. M. Garza, S. P. Warrick, G. S. Seligman, L. V. Zavyalova, A. van Zwol, and J. Foster, “Tool ranking using aberration measurements in a high-volume manufacturing facility,” *Proceedings of SPIE* **5040**(1), 1432–1440 (2003) [doi:doi:10.1117/12.485428].

[131] J. Meute, G. K. Rich, W. Conley, B. W. Smith, L. V. Zavyalova, J. S. Cashmore, D. Ashworth, J. E. Webb, and L. Rich, "Correction of 157-nm lens based on phase ring aberration extraction method," *Proceedings of SPIE* **5377**(1), 195–203 (2004) [doi:doi:10.1117/12.544256].

[132] L. V. Zavyalova, A. R. Robinson, A. Bourov, N. V. Lafferty, and B. W. Smith, "On the quality of measured optical aberration coefficients using phase wheel monitor," *Proceedings of SPIE* **6520**(1), 65203T–65203T–9 (2007) [doi:doi:10.1117/12.721311].

[133] L. V. Zavyalova, B. W. Smith, A. Bourov, G. Zhang, V. Vellanki, P. Reynolds, and D. G. Flagello, "Practical approach to full-field wavefront aberration measurement using phase wheel targets," *Proceedings of SPIE* **6154**(1), 61540Y–61540Y–9 (2006) [doi:doi:10.1117/12.657928].

[134] L. V. Zavyalova, B. W. Smith, T. Suganaga, S. Matsuura, T. Itani, and J. S. Cashmore, "In-situ aberration monitoring using phase wheel targets," *Proceedings of SPIE* **5377**(1), 172–184 (2004) [doi:doi:10.1117/12.537379].

[135] J. V. Hermans, E. Hendrickx, D. Laidler, C. Jehoul, D. Van Den Heuvel, and A.-M. Goethals, "Performance of the ASML EUV Alpha Demo Tool," *Proceedings of SPIE* **7636**(1), 76361L–76361L–12 (2010) [doi:doi:10.1117/12.848210].

[136] "Optics & Photonics Focus- Extreme Ultraviolet Lithography: Towards the Next Generation of Integrated Circuits," <http://opfocus.org/index.php?topic=story&v=7&s=4> (14 April 2012).

[137] D. Hibino, H. Shindo, Y. Abe, Y. Hojyo, G. Fenger, T. Do, I. Kusnadi, J. L. Sturtevant, P. De Bisschop, et al., "High-accuracy OPC-modeling by using advanced CD-SEM based contours in the next-generation lithography," *Proceedings of SPIE* **7638**(1), 76381X–76381X–11 (2010) [doi:doi:10.1117/12.846025].

[138] H. Shindo, A. Sugiyama, H. Komuro, Y. Hojo, R. Matsuoka, J. L. Sturtevant, T. Do, I. Kusnadi, G. Fenger, et al., "High-precision contouring from SEM image in 32-nm lithography and beyond," *Proceedings of SPIE* **7275**(1), 72751F–72751F–9 (2009) [doi:doi:10.1117/12.814430].

[139] "MET - How It Works," <http://met.lbl.gov/met> (14 April 2012).